
Politecnico di Torino

Avio Aero
a GE Aerospace company

**Corso di Laurea Magistrale**
**in Ingegneria Meccanica (Mechanical Engineering)**

Tesi di Laurea Magistrale

# "*Multibody dynamic analysis of geared transmission systems*"

**Relatrice**

Prof.ssa Teresa Maria Berruti

**Tutor**

Ing. Davide Allaio (Avio Aero)

Ing. Marco Tommasi (Avio Aero)

**Candidato**

Daniele Di Piazza

A.A. 2025/2026

Contents

## Abstract

*In view of the constant trend toward reducing the mass of aircraft engine components, gears dynamics has assumed an increasingly important role in the development of new products. The reduction in component mass entails a decrease in their dimensions as well as an increase in their flexibility, making some phenomena associated with high rotational speeds no longer negligible.*

*In this context, the present thesis, carried out in collaboration with GE Avio Aero, represents a preliminary study for the multibody analysis of complex transmission systems by means of the MSC.Adams software. After an initial phase devoted to the modelling of rotors with multiple degrees of freedom, a model of a compound gearbox was developed to analyze the effects that micro-geometry modifications, combined with the non-negligible deformations of the components, exert on the system dynamics.*

*Time-domain simulations under quasi-static loading conditions were performed on the gearbox model. The progressive introduction of an increasing level of detail made it possible to highlight how the transmission error is influenced using tooth profile modifications aimed at improving the contact conditions.*

*The thesis therefore lays the foundations, through a multibody approach, for the study of high-frequency dynamic effects that develop within transmission systems for aeronautical applications, providing useful indications for the continuation of research in this field.*

# 1. INTRODUCTION

## 1.1. Aim of the work

With the ever-increasing need to reduce the mass of moving components within mechanical systems, especially when such systems are employed in aeronautical structures, the study of transmission system dynamics assumes paramount importance. Geared systems, although central components in many applications, have long been a source of vibrations and noise in mechanical assemblies.

In the aeronautical field in particular, the drive toward increasingly efficient engines have directed engineering efforts toward the development of high bypass ratio architectures, which in turn force the front fan to operate at low rotational speeds due to the continually increasing diameters. The ratio between the engine rotational speed and that of the fan becomes progressively higher, creating the need for increasingly complex speed-reduction units which, despite stringent weight and size constraints, can withstand high and continuous loads.

It is precisely the need to limit masses, which constrains component dimensions and gear rim thickness, that reduces the structural stiffness of the elements and makes it essential to develop models capable of handling the interactions between tooth contact forces and the modes of the wheel body. Given their very slender structure, these wheels bodies can be readily excited by the gear mesh frequency. If indeed the wheel bodies have their outer diameter which is much larger than their thickness, they can show some similarity with the behavior of rotating membranes described in [1].

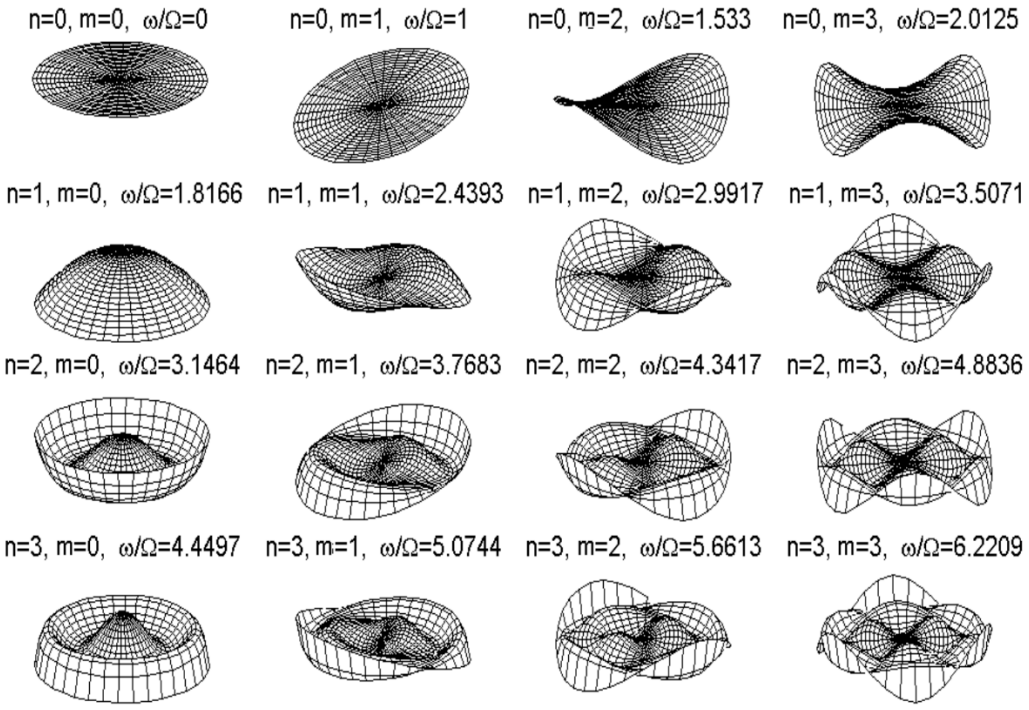


*Figure 1: Examples of thin disk modes from [1]*

Figure 1 shows several mode shapes of rotating membranes for different values of m, nodal diameters, and n, nodal circles. It is clear that the behavior of these rotating bodies can be very complex, especially when considered in the framework of gearbox dynamics where the main source of excitation is also non-linear.

Thus, it is of quite relevant importance to consider the deformability of the wheel bodies. An example is shown in [2] where, by considering these effects, it is evident how deformability affects variations in mesh stiffness, which is the primary driver of vibration phenomena introduced by geared systems.

Another example of a model where wheel bodies flexibility is considered is presented in [3], here a multibody approach has been used, thus nonlinear and with time- or space-varying coefficients (a Nonlinear Time-Variant approach), which enables the capture of phenomena associated with the non-negligible

deformations of the bodies during simulation, as well as time-varying parameters such as mesh stiffness

The multibody dynamics (MBD) approach appears to be one among the most promising ways for studying such complex phenomena. Making this option even more compelling is the availability of MBD software that enables efficient and effective modeling of gear systems, as well as bearings and splines.

The aim of this thesis, within the framework of rotor dynamics for transmission systems in aeronautical applications, is therefore to conduct a study to assess the capabilities of an MBD software package (MSC Adams) in the analysis and simulation of complex geared transmission systems.

## 1.2. Rotor dynamics

Studying the fundamentals of rotor dynamics is of paramount importance for understanding dynamic phenomena in more complex rotating systems, such as gears.

The two simplest models for investigating these phenomena are:

- *Jeffcott rotor*
- *4DOF rotor*

In the following sections, the equations of motion will be derived, and the characteristics of both models, as well as their differences, will be examined.

### 1.2.1. Jeffcott rotor

The so-called Jeffcott rotor model provides a significant simplification of rotor behavior, yet it remains a useful tool for studying its fundamentals. The model consists of a point mass connected to a massless shaft:

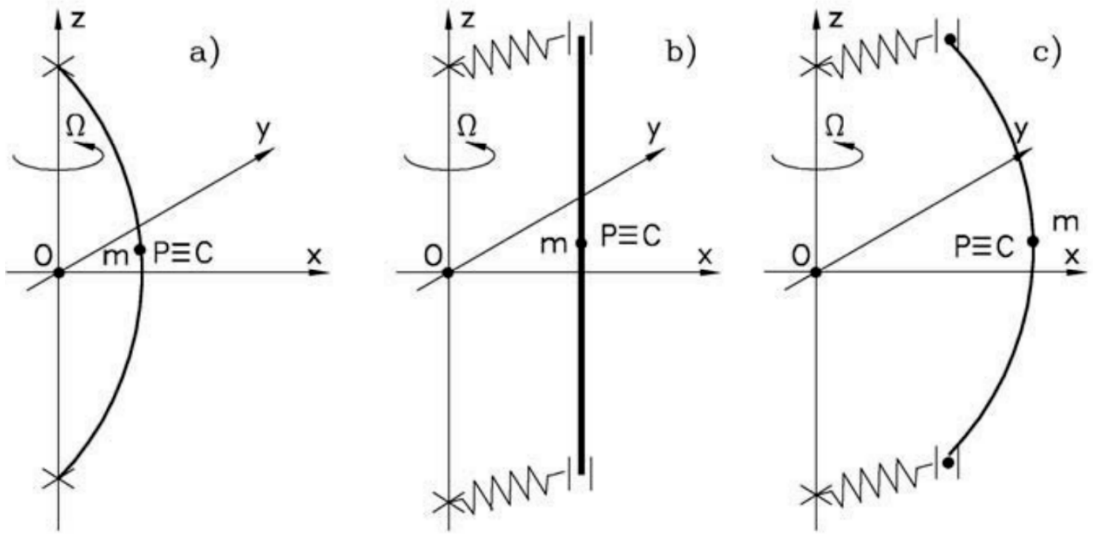


*Figure 2: Different configurations for Jeffcott rotor model [1]*

The three configurations shown in Figure 2 represent models that exhibit the same behavior in the case where they are completely undamped (both with respect to the connections and to the potentially deformable shaft in configurations (a) and (b)) and axisymmetric [1]. An assumption that greatly simplifies the model's behavior is that, in this case, both point P, the center of mass of the rotor, and point C, the elastic center of the rotor, are considered to lie on the x-y plane at all times by virtue of the small-displacement assumption [1].

However, in order to derive the equations of motion, it is necessary to introduce a small distance $\epsilon$, referred to as the eccentricity, between points P and C, since in practice they never coincide, and even a small eccentricity can strongly influence the system dynamics. The system thus becomes that shown in the figure below.

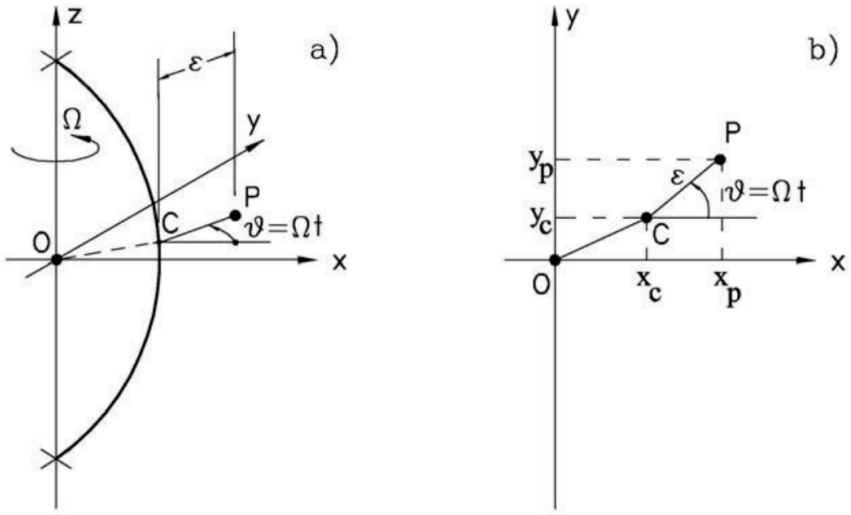


*Figure 3: Unbalanced Jeffcott rotor model [1]*

Figure 3 shows how the system gets modified when considering eccentricity. By using real coordinates of point C, the following EOMs of the system can be obtained:

$$\begin{cases} m\ddot{x}_C(t) + kx_c = m\epsilon\Omega^2 cos(\Omega t) + F_x(t) \\ m\ddot{y}_C(t) + ky_c = m\epsilon\Omega^2 sin(\Omega t) + F_y(t) \end{cases}$$

Where $F_x(t)$ and $F_y(t)$ are generic forcing terms; $\Omega$ is the rotational speed imposed by the driving system and $k$ is the overall stiffness, which may correspond to the shaft's bending stiffness (case (a)), the stiffness of compliant bearings (case (b)), or a combination of the two (case (c)). As is readily observed, the two equations are completely decoupled and, in both cases, the natural frequency is:

$$\omega_n = \Omega_{cr} = \sqrt{\frac{k}{m}}$$

That frequency, obtained by considering the system at standstill, represents the flexural critical speed, which is reached when the excitation frequency (static unbalance) equals the natural frequency.

The same system, expressed by introducing the complex coordinate $r_C(t) = x_C(t) + ix_C(t)$ is described by the following equation of motion:

$$m\ddot{r}_C(t) + kr_C = m\epsilon\Omega^2 e^{i\Omega t} + F_n(t)$$

By doing the Laplace transform of both ends of the equation and by defining the Laplace variable $s = \sigma + i\omega$ it is possible to find the following roots:

$$s_{1,2} = \sigma_{1,2} + i\omega_{1,2}$$

$$\sigma_{1,2} = 0; \qquad \omega_{1,2} = \pm\sqrt{\frac{k}{m}} = \pm\omega_n$$

The two values of the imaginary part of *s* describe a *forward* or *direct whirl* and a *backward* or *circular whirl* motion. The value of omega is independent from the rotational speed of the rotor; in a Campbell diagram this will translate in two horizontal lines.

When introducing damping into the system, it is important to distinguish between non-rotating damping, associated with the non-rotating structure such as the bearings, and rotating damping, associated with the moving components of the system. The latter, unlike the former, has a stabilizing effect in the subcritical range but can have a destabilizing effect in the supercritical regime [1].

Introducing damping and formulating the problem in a rotating reference frame leads to the following result:

$$m\ddot{r}_C(t) + (c_r + c_n)\dot{r}_C + (k - ic_r\Omega)r_C = m\epsilon\Omega^2 e^{i\Omega t} + F_n(t)$$

Where $c_r$ and $c_n$ are the damping associated with the rotating structure and the non-rotating structure, respectively. As is evident from the result above, the rotating damping contributes to the formation of a circulatory matrix when describing multiple degrees of freedom rotors.

The spin speed that represents the threshold of instability due to the presence of rotating damping in a Jeffcott rotor model is equal to:

$$\Omega_{\text{instability}} = \sqrt{\frac{k}{m}} \cdot \left(1 + \frac{c_n}{c_r}\right)$$

For $\Omega > \Omega_{instability}$ the system is unstable as shown in the following decay rate plot:

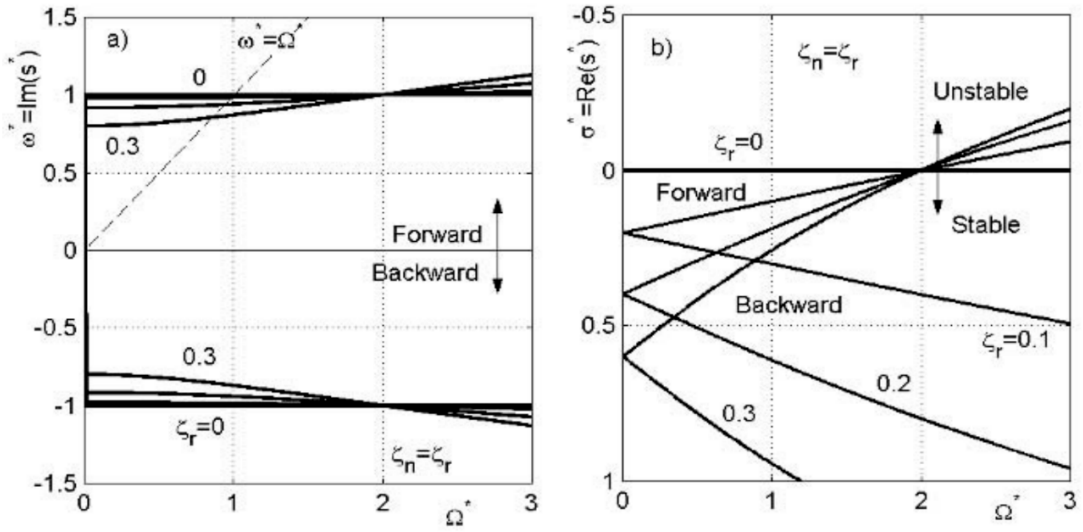


*Figure 4: Influence of damping on system stability [1]*

The results in Figure 4 above have been obtained for different values of damping ratio but always with $c_n = c_r$. As can be seen from the decay rate plot on the right the real part of the Laplace variable keeps decreasing for the *forward whirl mode* when increasing the velocity and eventually becomes negative at $\Omega = \Omega_{instability}$. The Campbell diagram on the left now shows how the frequency is depending upon the rotational speed and shows two horizontal lines only when $\zeta_n = \zeta_r = 0$.

The concept of instability associated with the effect of rotating damping in the supercritical regime was of significant relevance throughout the thesis project, particularly in certain analyses conducted on the *flexible rotor model* test case. Indeed, when finite element models are introduced, especially when the rotating components are not thin disks and cannot be represented as a series of beam elements joined together, it becomes particularly challenging to account for

effects related to the distinction between rotating and non-rotating damping, as well as to incorporate gyroscopic and Coriolis effects and centrifugal stiffening, which cannot be considered in this model due to its extreme simplicity.

### 1.2.2. 4DOF Rotor model

Compared with the Jeffcott rotor, the 4DOF rotor model no longer treats the mass as a point mass; instead, the mass is represented by a disk with a nonzero inertia ellipsoid. This enables accounting for the dependence of the natural frequencies on the rotor spin speed, an effect that, in the Campbell diagram, manifests as a clear variation of the conical mode frequencies with speed.

The models depicted in Figure 5 are examples of a 4DOF model:

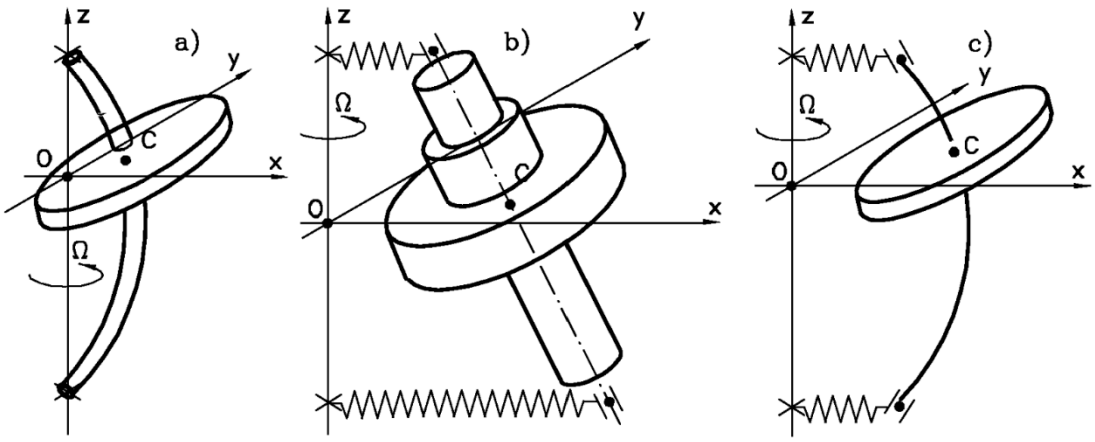


*Figure 5: 4DOF rotor model examples [1]*

With reference to the derivation presented by Professor Genta in his text "*Dynamic of Rotating Systems*" [1], to arrive at the equations of motion of the system, it is convenient to define four different reference frames. The first two are centered at O and represent the inertial frame (OXYZ) and the rotating frame (OΘHZ), which rotates at angular speed Ω. The remaining two are centered at C and are used to track point P while also accounting for the disk rotations about the x and y axes.

By introducing the following complex coordinates:

$$\begin{cases} r = X + iY \\ \phi = \phi_y - i\phi_{X'} \end{cases}$$

where X and Y are the coordinates of point C in the inertial reference frame, and $\phi_y$ and $\phi_{X'}$ are the angular coordinates of the plane on which the disk lies, if one neglects the contribution of small terms and the coupling between the axial direction and the two rotations around x and y, the set of equations of motion of the system can be written as follows:

$$\boldsymbol{M}\ddot{\boldsymbol{q}} + (\boldsymbol{C_n} + \boldsymbol{C_r} - i\Omega\boldsymbol{G})\dot{\boldsymbol{q}} + (\boldsymbol{K} - i\Omega\boldsymbol{C_r})\boldsymbol{q} = \Omega^2\boldsymbol{f}e^{i\Omega t}$$

Where:

$$\boldsymbol{M} = \begin{bmatrix} m & 0 \\ 0 & J_t \end{bmatrix}, \quad \boldsymbol{G} = \begin{bmatrix} 0 & 0 \\ 0 & J_p \end{bmatrix}, \quad \boldsymbol{K} = \begin{bmatrix} K_{11} & K_{12} \\ K_{12} & K_{22} \end{bmatrix}, \quad \boldsymbol{q} = \begin{Bmatrix} r \\ \phi \end{Bmatrix}, \quad \boldsymbol{f} = \begin{Bmatrix} m\epsilon e^{i\alpha} \\ \chi(J_t - J_p) \end{Bmatrix}$$

With $J_t$ and $J_p$ denoting the transverse and polar mass moments of inertia, respectively, $\alpha$ the unbalance phase, $\chi$ the angular error due to manufacturing inaccuracy and $\boldsymbol{G}$ the gyroscopic matrix. As is evident from the system of equations, these are completely decoupled if the component $K_{12} = 0$, a condition that holds when the disk is mounted at the rotor center. If the system is studied in the uncoupled form, one observes that the first equation is equivalent to the Jeffcott rotor case; therefore, focusing on the second equation, recalling that $s = \sigma + i\omega$ and considering the undamped system, one obtains:

$$\begin{cases} \omega = \dfrac{J_p\Omega \pm \sqrt{-{J_p}^2\Omega^2 + 4J_tK_{22}}}{2J_t} \\ \sigma = 0 \end{cases}$$

As can be inferred from the result above, the effect of the gyroscopic matrix varies the natural frequencies of the system as the rotational speed changes, and it has a softening effect on the backward whirl mode and a stiffening effect on the forward whirl mode.

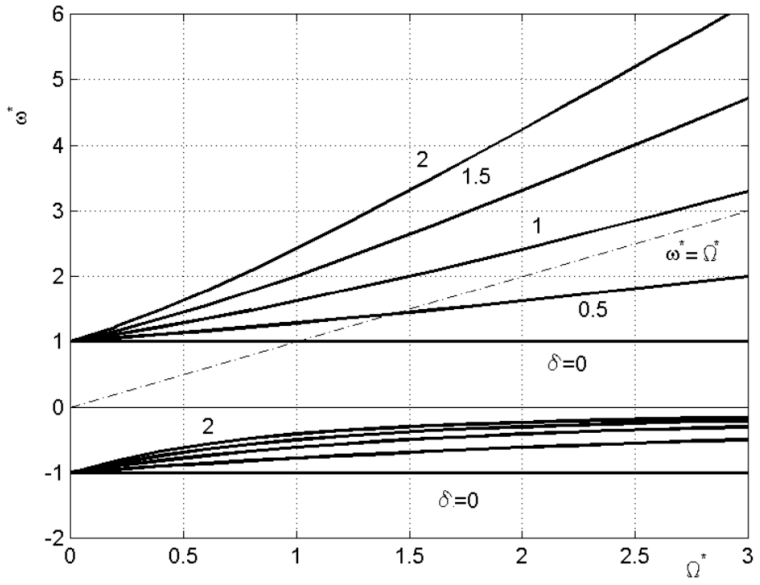


*Figure 6: Influence of gyroscopic effect on whirl modes frequency [1]*

If the natural frequencies obtained from the second equation are plotted in a Campbell diagram, a result like that in Figure 6 is obtained. In this case, the rotational speed and the natural frequency have been normalized, and $\delta = J_p/J_t$. It is noteworthy that the only way to excite the forward whirl mode with an unbalance-like excitation is to have $\delta < 1$, which is why two different models were developed during the study for analyzing the 4DOF rotor model in MSC Adams.

## 1.3. High Frequency gearbox dynamics

The main cause of vibration phenomena associated with geared systems is the variation of mesh stiffness correlated with the Transmission Error (TE). The latter is a quantity, measurable either as an angle or as a length, that represents the difference between the actual angular position occupied by the gears during meshing and the position they would theoretically occupy if the forces developed between the teeth did not lead to deformation of the system components. It is common practice to divide the transmission error into two categories: Static Transmission Error (STE), pertaining to working conditions such as low-speed

or quasi-static analyses, and Dynamic Transmission Error (DTE), defined for high rotational speeds [4].

The static transmission error can be expressed as an angular deviation [5]:

$$\Delta\theta_1(\theta_2) = \theta_2 - \frac{Z_1}{Z_2}\theta_1$$

Where $\theta_1$ and $\theta_2$ are the two angular positions of the meshing gears, whereas $Z_1$ and $Z_2$ are the respective teeth number, or it can be express as a length [5]:

$$STE(\theta_1) = r_2\theta_2(\theta_1) - r_1\theta_1$$

Where $r_1$ and $r_2$ are the pitch radii of the meshing gears.

It is important to emphasize that transmission error is a consequence of component compliance which, under external loading, inevitably leads to deformation and thus a deviation from the ideal contact conditions, resulting in oscillations relative to the desired output. Unlike STE, DTE is by definition influenced by frequency-related phenomena, such as system- or component-level resonances [5]. These resonances can induce non-negligible increases in the forces transmitted between the two gears, leading not only to unexpectedly severe loading conditions but also to a significant rise in component deformations and, consequently, in DTE.

In developing models to simulate the effect of meshing contact on system dynamics, it is necessary to highlight that not only the deformability of individual teeth, namely the combined contributions due to tooth bending and localized deformations caused by Hertzian contact, but also the deformations of the transmission shafts, the displacements of compliant bearings, and, in particular, the deformations of the wheel bodies contribute to increased transmission error and hence to oscillations in mesh stiffness. As shown by the results reported in [2], modeling the wheel bodies as deformable within the framework (Flexible Gear Body, FGB) yields a mesh stiffness variation that is substantially more gradual and reduced compared with the Rigid Gear Body (RGB) model.

Selected results are reported below:

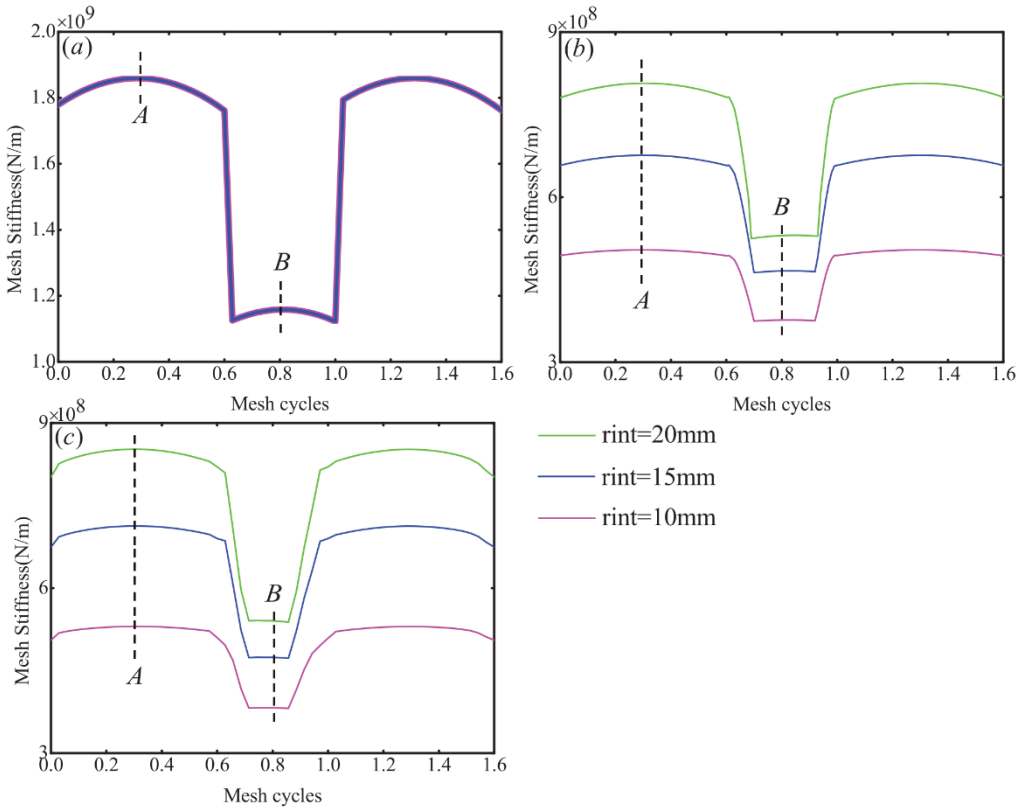


*Figure 7: Mesh stiffness variation when considering flexible wheel bodies [2]*

In Figure 7(a) the results of the RGB model are shown, in Figure 7(b) the results of the FGB model, and in Figure 7(c) the results of the FEM model. The results were extracted for three different values of the gear inner radius (20 mm, 15 mm, and 10 mm), and in the RGB case no differences are observed among the three curves precisely because wheel-body deformations are not considered in any instance. The results clearly show that the variation in mesh stiffness occurring during the transition from meshing supported by a single tooth pair to meshing supported by two tooth pairs is much less pronounced and much less abrupt in Figure 7 (b) and (c). Accounting for this effect can be of crucial importance when, in sectors such as aerospace where limiting components weight is a priority, wheel-body dimensions get reduced, and this not only lowers component stiffness

but also increases the amplitude of the excitation associated with mesh stiffness oscillation.

First and foremost, its oscillation is a natural consequence of the periodicity of the meshing process; it is precisely this feature that makes transmission error a periodic phenomenon [5]. To better elucidate this concept, it is useful to introduce the Gear Mesh Frequency (GMF), described as follows:

$$GMF = f_0 \cdot Z$$

Where $f_0$ is the rotational frequency and Z the number of teeth of the meshing gear. If the harmonic content of the transmission error is examined in the absence of geometric defects, one can observe the presence of integer multiples of the GMF [5].

A commonly recognized approach to reducing the aforementioned oscillations is the application of Tooth Profile Modifications (TPMs) such as tip relief, root relief and lead crowning. Such micro-geometric modifications facilitate contact by partially mitigating issues associated with corner contact (generally occurring at the end of a tooth's meshing cycle) and edge contact, which is primarily due to deviations of the gear axes from their ideal positions.

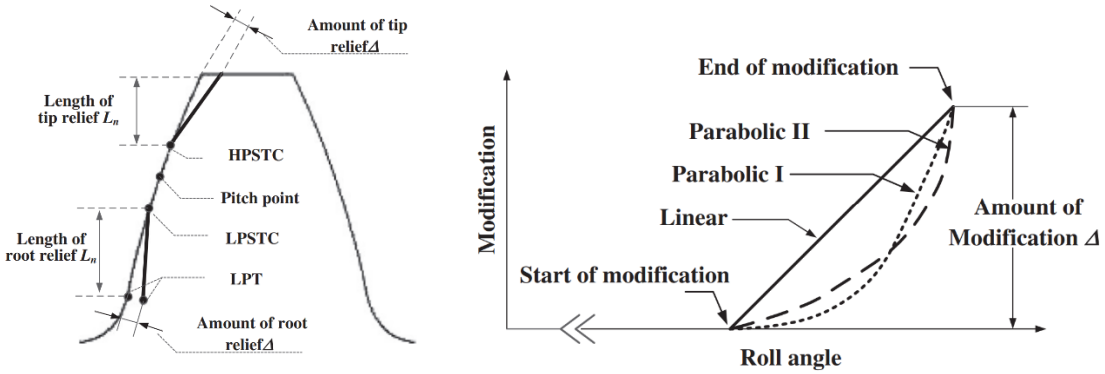


*Figure 8: Examples of Tooth Profile Modifications (Tip and root relief) [6]*

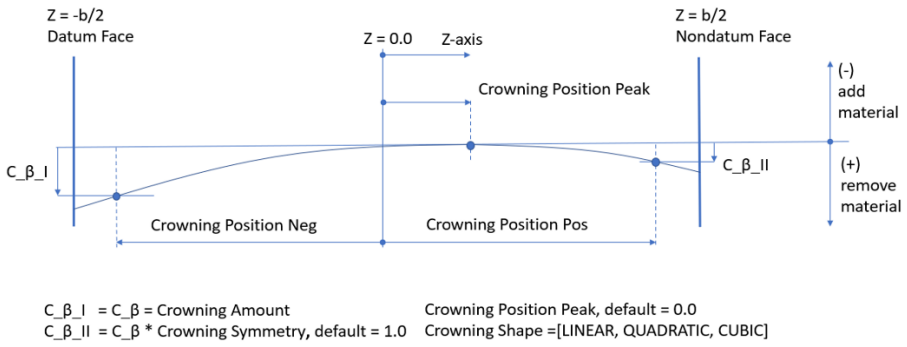


*Figure 9: Examples of Tooth Profile Modifications (Lead crowning) [7]*

In Figure 8 tip and root relief modifications are presented whereas in Figure 9 lead crowning modification is shown. Both will be used in the model developed during the fourth chapter.

There are numerous studies on the effectiveness of introducing micro-geometric modifications to achieve significant reductions in transmission error and the resulting system vibration and noise. Among these is [8], which investigated, through a model developed to study the effect of TPMs on the dynamic behavior of a planetary gearbox, the impact that increasing the amount of material removed from the tooth profile has on the frequency response.

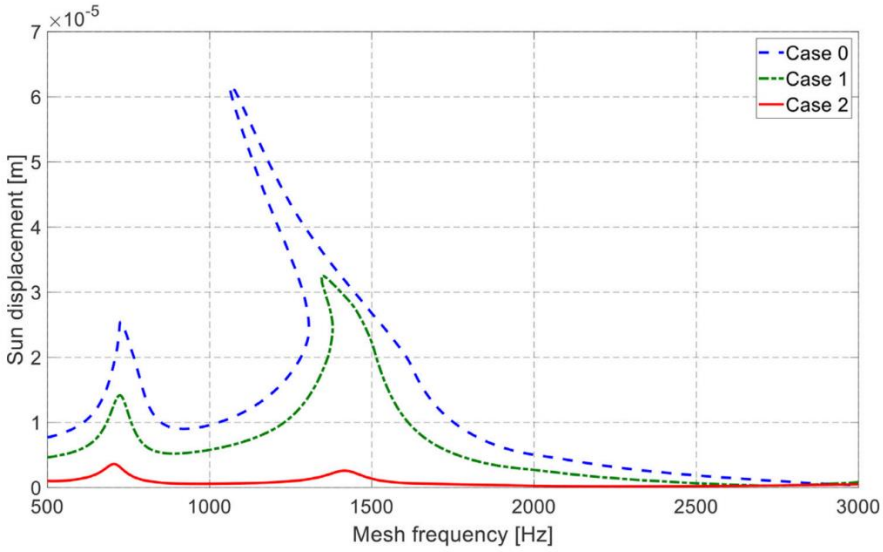


*Figure 10: Influence of TPMs on the frequency response of a planetary gearbox [8]*

For Figure 10, the author specifies that in case 0 no micro-geometric modifications were applied, whereas in cases 1 and 2 the magnitude of these modifications (applied on the tip and the root of the tooth profile) was progressively increased and, as evident from the chart, this led to a significant reduction in the frequency response. Furthermore, a smaller frequency response implies system behavior which is less influenced by non-linear effects. A lower frequency response can only benefit the system dynamics, as it also entails a reduction in the dynamic mesh force. It should be emphasized, however, that the positive effect provided by TPMs is strongly dependent on the torque transmitted through the system [8].

In light of these considerations, it is undeniable that studying the effect of TPMs on gearbox dynamics plays a crucial role and largely represents the primary objective of the power gearbox model developed over the course of this thesis.

## 1.4. MSC.Adams

MSC Adams (Automated Dynamic Analysis of Mechanical Systems), owned by MSC Software, is the most used commercial multibody dynamics simulation software. Through a full Graphical User Interface (GUI) the software gives the user a rather intuitive approach to the construction and simulation of the entire model.

MSC Adams is made of several modules that can be used through the main GUI which is Adams/View, herein the following will be discussed:

- Adams/Flex
- Adams/Machinery

### 1.4.1. Adams/Flex

Adams/Flex is an add-on of Adams that can be used both through Adams/View and Adams/Solver and it allows the user to import/create and manage deformable body in a model. The software achieves this through the definition of a *Modal Neutral File* (MNF) which can be generated directly on Adams/View, through an embedded NASTRAN solver in the software, or it can be imported from another FEA software [9].

For example, a way to create an MNF on Adams without the need of using an external FEA software is to use the ViewFlex option which allows, through the command "*Rigid-to-Flex*", to create a FE mesh of an existing rigid body in the model.

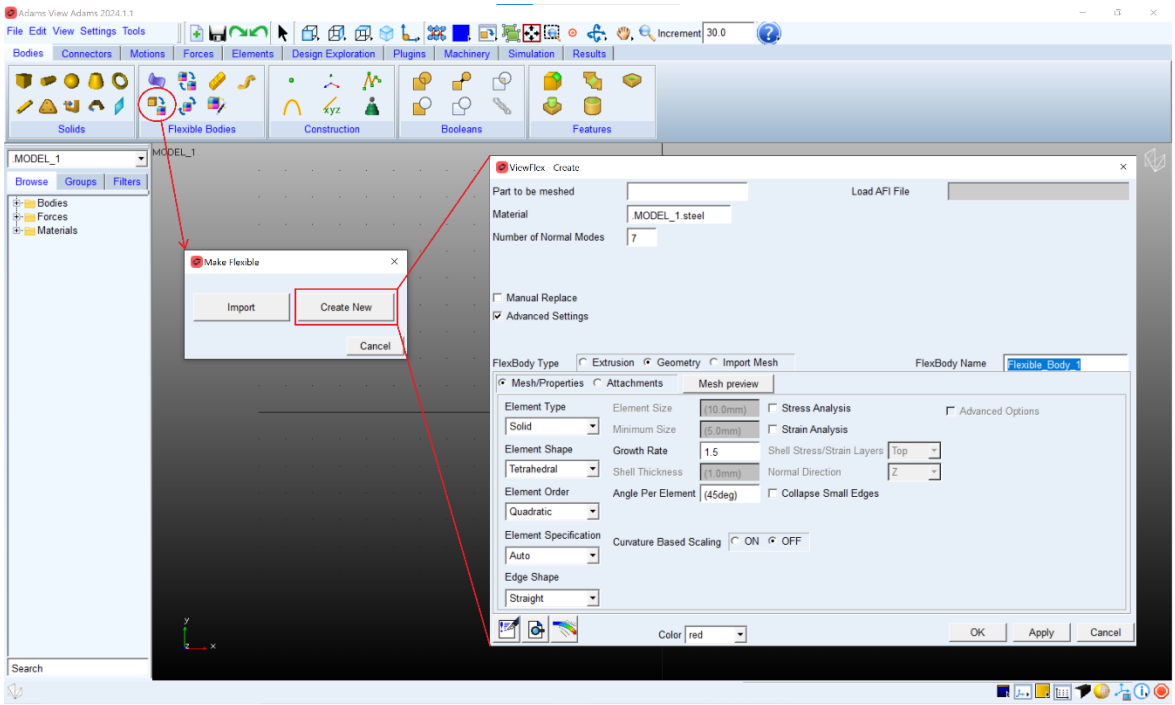


*Figure 11: Steps to create a FE part on Adams*

In the Figure 11 it is shown how to, by selecting the *Rigid-to-Flex* option in the *Flexible Bodies* commands, create a FE mesh of an existing rigid body in the model. As can be seen this solution offers great possibilities in terms of time saving, but if one wants to introduce a Generalized Damping matrix or mesh

complex geometry it is probably better to import the MNF from an external software. To create an MNF from an external software it is possible to exploit the NASTRAN/Adams interface through which the MNF can be generated on NASTRAN while also specifying the parameters of the desired reduction.

The MNF is a binary file and represents the flexible body description file, including the following information:

- Geometry
- Nodal mass and inertia
- Mode shapes
- Generalized mass and stiffness for mode shapes (and eventually Generalized Damping matrix)

The information coming from the MNF describes the model after a reduction method (CMS) has been performed. The boundary nodes defined before the reduction process will represent the attachment points for that body in the model, this means that they will be used to attach joints, apply forces and in general to interface with the flexible body.

**Rotor dynamics in Adams**

From 2024.1 version of the solver a new feature has been introduced to deal with rotating flexible bodies in the software. This feature allows to capture local gyroscopic effects for the body if its MNF has been generated with the SOL 107 command (Direct Complex Eigenvalues) of NASTRAN [12], [9]. Through this procedure the resulting MNF will be storing the gyroscopic, the circulatory and the differential stiffness matrix if the body.

In Adams only the fixed reference frame formulation of the EOMs is available [13]:

$$[\boldsymbol{M}]\{\ddot{\boldsymbol{g}}\} + ([\boldsymbol{B}_R] + [\boldsymbol{B}_S] + \Omega[\boldsymbol{G}])\{\dot{\boldsymbol{g}}\} + ([\boldsymbol{K}] + \Omega[\boldsymbol{K}_C]_R + \Omega^2[\boldsymbol{K}_G])\{\boldsymbol{g}\} = \{\boldsymbol{F}_S\}$$

Where:

- $\boldsymbol{M}$ is the mass matrix
- $\boldsymbol{g}$ is the vector of generalized coordinates
- $\boldsymbol{B_R}$ is the damping in the rotating frame
- $\boldsymbol{B_S}$ is the damping in the fixed frame
- $\boldsymbol{G}$ is the gyroscopic matrix
- $\boldsymbol{K}$ is the stiffness matrix
- $[\boldsymbol{K_C}]_R$ is the circulatory matrix
- $\boldsymbol{K_G}$ is the differential stiffness matrix
- $\Omega$ is the angular velocity

In Adams the effects of velocity related phenomena are considered as the application of a modal force (MFORCE statement, [14]) along the length of the shaft [15]:

$$\boldsymbol{Q_v} = -(\Omega[\boldsymbol{G}]\{\dot{\boldsymbol{g}}\} + (\Omega[\boldsymbol{K_C}]_R + \Omega^2[\boldsymbol{K_G}])\{\boldsymbol{g}\})$$

Therefore, the final form of the above equation of motion becomes:

$$[\boldsymbol{M}]\{\ddot{\boldsymbol{g}}\} + ([\boldsymbol{B_R}] + [\boldsymbol{B_S}])\{\dot{\boldsymbol{g}}\} + [\boldsymbol{K}]\{\boldsymbol{g}\} = \{\boldsymbol{F_S}\} + \{\boldsymbol{Q_v}\}$$

### 1.4.2. Adams/Machinery – Gear AT

Adams/Machinery is an add-on module of the MSC.Adams multibody dynamics environment specifically developed for the modeling and simulation of rotating machinery and power transmission systems. It provides a library of pre-configured, parameterized components such as gears, bearings, belts, chains, pulleys, and cams, enabling the user to build complex mechanical assemblies starting from high-level design parameters rather than from low-level geometric and joint definitions.

For the development of the model presented in chapter 4 the module Gear AT (Advanced Technology) of Adams/Machinery has been exploited. The Gear AT module of Adams/Machinery is specifically designed for the modeling and simulation of gear transmissions, with particular focus on their dynamic behavior

under realistic operating conditions. Within Gear AT, the gear mesh is represented by dedicated formulation that accounts for time-varying mesh stiffness, backlash, contact losses, and alignment conditions between mating gears [7]. The creation of a model within the Gear AT environment can be done by following the flow chart below:

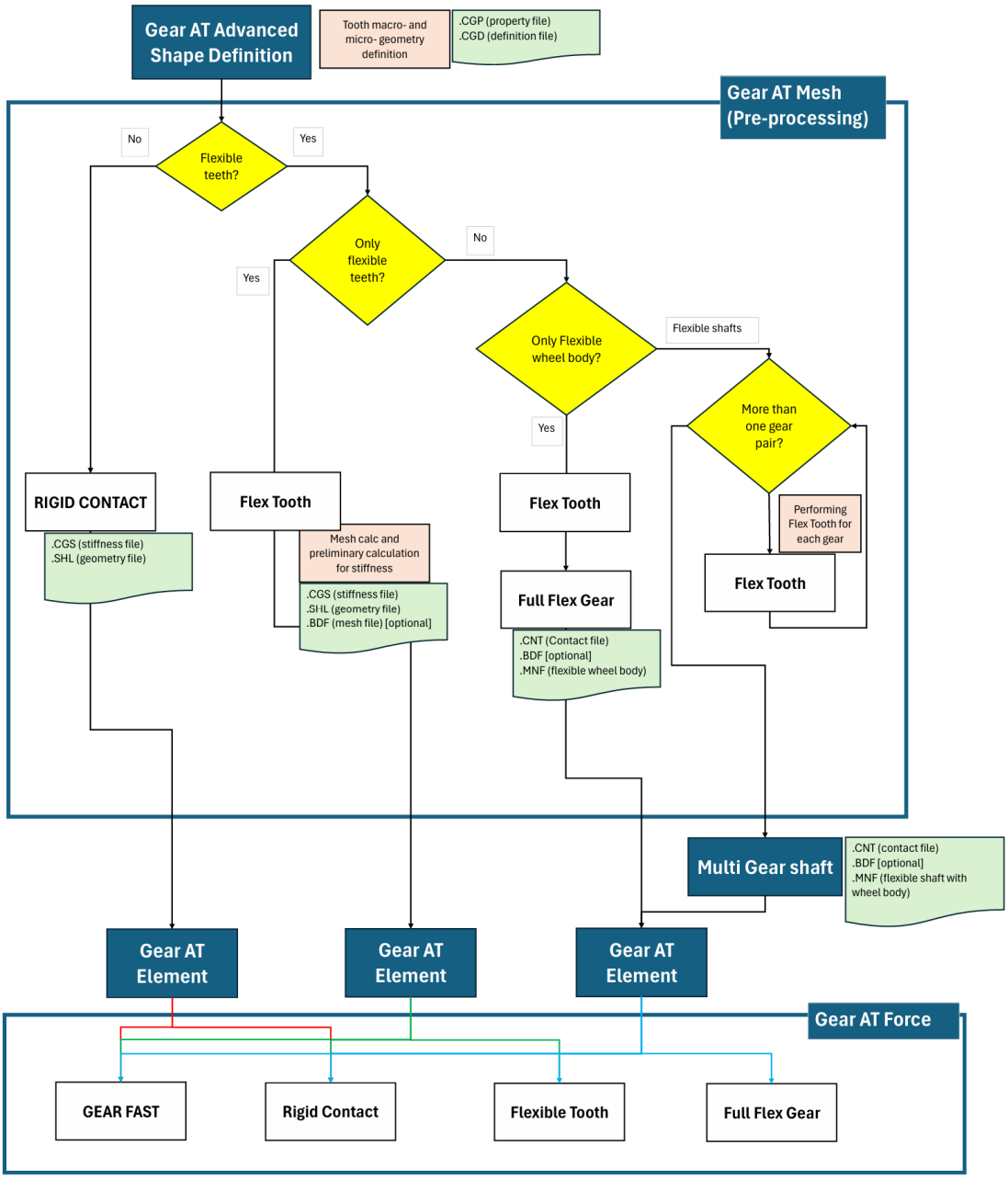


*Figure 12: Flow chart to create a gearbox model in Gear AT*

Concerning the above flow chart (Figure 12), it is important that each step is followed in the right order because gear files (like the gear property file created at the very first step) will be constantly updated. In such way the software can create the gear model by referring only to a few files, like the gear property file.

### Gear AT Advanced Shape Definition

Firstly, one must define the tooth geometry through the *Gear AT Advanced Shape Definition.* Through this step it is possible to define general geometric features of the gear (such as module, number of teeth, pressure angle and so on), mass properties, tooth profile, tolerances (such as backlash), tooth profile modifications, deviations to consider gear manufacturing errors and measurement data to better match the true ideal flank geometry.

As a result of the completion of this step two files are obtained as output:

- *Property file* that stores all the gear element parameters that define the tooth profile characteristics (.CGP, Cylindrical Gear Property if a cylindrical gear is generated)
- *Definition file* that stores all settings for gear profile generation such as tool parameters and everything that one can find in a gear datasheet (.CGD, Cylindrical Gear Definition)

The two files are then used to proceed into the next steps of the model generation, starting from the mesh generation through *Gear AT Mesh*.

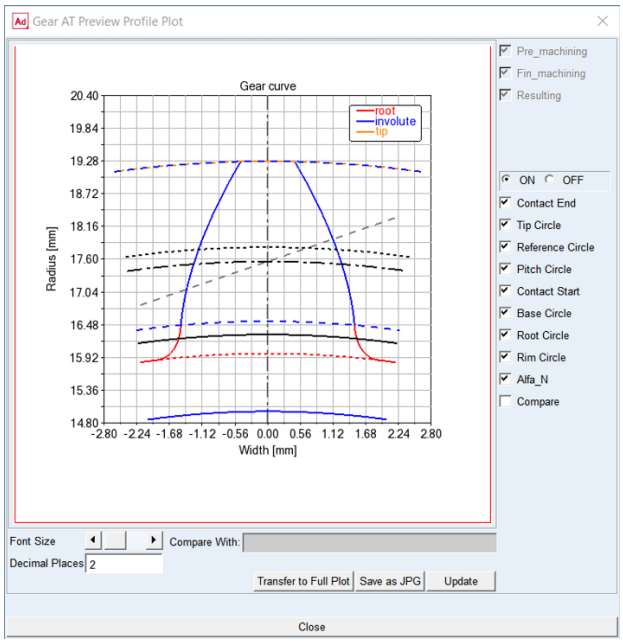


*Figure 13: Example of tooth profile preview in GearAT Advanced Shape Definition [7]*

Figure 13 shows the tooth profile preview, available after having specified its geometric characteristics in Gear AT Advanced Shape Definition.

### Gear AT Mesh

This is the second step after the gears data are obtained. *Gear AT Mesh* allows to preprocess the gear tooth FE model to get contact surfaces and stiffness matrix for contact simulation.

Gear AT mesher offers three main modes of operation:

- *Rigid Contact*
- *Flex Tooth*
  - *Full Flex Gear* (available only after having selected *Flex Tooth*)

By selecting the *Flex Tooth* option and through the information provided by the property and definition files obtained before Gear AT mesher allows one to obtain the following files:

- *Stiffness file* (.CGS) evaluated after a SOL101 (Linear Static Analysis) is executed by means of the NASTRAN solver embedded in Adams (this mainly permits to evaluate the bending stiffness of the tooth through the static application of several load cases on one of its flanks)
- *Geometry file* (.shl)
- *Mesh file* (.bdf) of the tooth, if desired

The tooth mesh is generated by setting the parameters shown in the following figure:

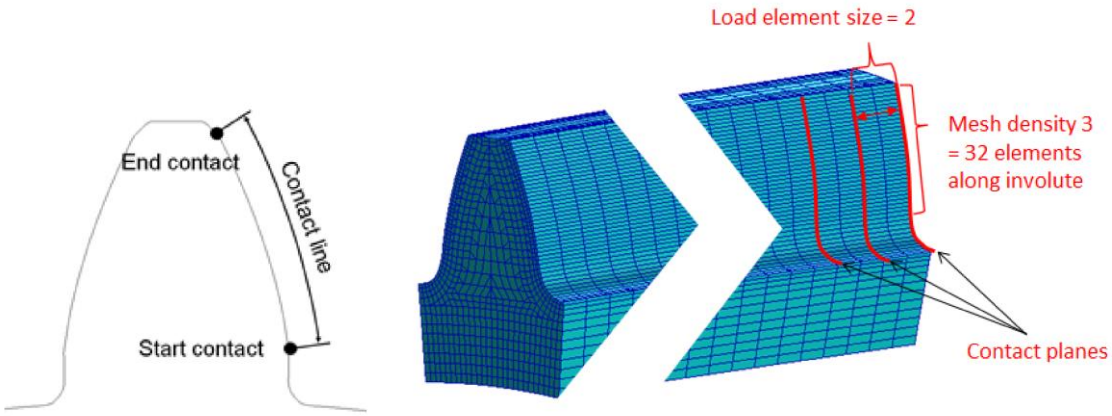


*Figure 14: Tooth FE mesh parameters [7]*

Where the:

- *Contact line* is the portion of tooth active profile (portion of the flank that participates in the contact), it coincides with the involute profile portion of the tooth and it is delimited by the *Tip Form Diameter* and the *Root Form Diameter* [7]
- *Mesh Density* defines the number of finite elements along the contact line. One can choose the *Mesh Density* for values from 0 to 5 which correspond to 8, 16, 24, 32, 40 and 48 elements along the contact line
- *Contact Planes* are the divisions along the tooth flank in the lead direction and are specified with the exact number of divisions along the lead

direction. Contact between mating gears is checked at each contact plane so a small number may lead to numerical noise

- *Load Element Size* defines the number of finite elements in lead direction per section, where each section is delimited by two contact planes. In this case, as for the contact planes, one must specify the exact number of elements between two contact planes

The CPU time will increase with mesh density, number of contact planes and load element size.

If the flexibility of the wheel body must be considered, it is necessary to also select the *Full Flex Gear* option that allows one to obtain:

- *Modal Neutral File* (MNF) of the wheel body
- *Mesh file* (.bdf) of wheel body and gear rim glued together

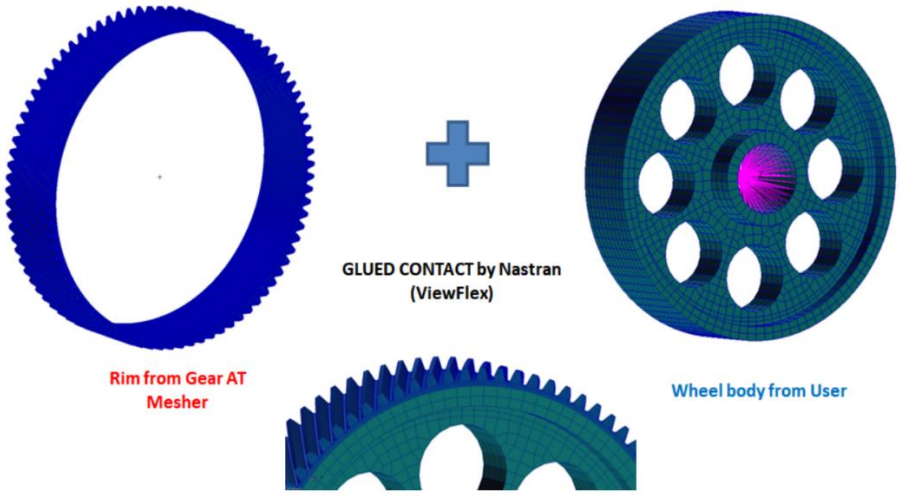


*Figure 15: Joining process description for Full Flex Gear option [7]*

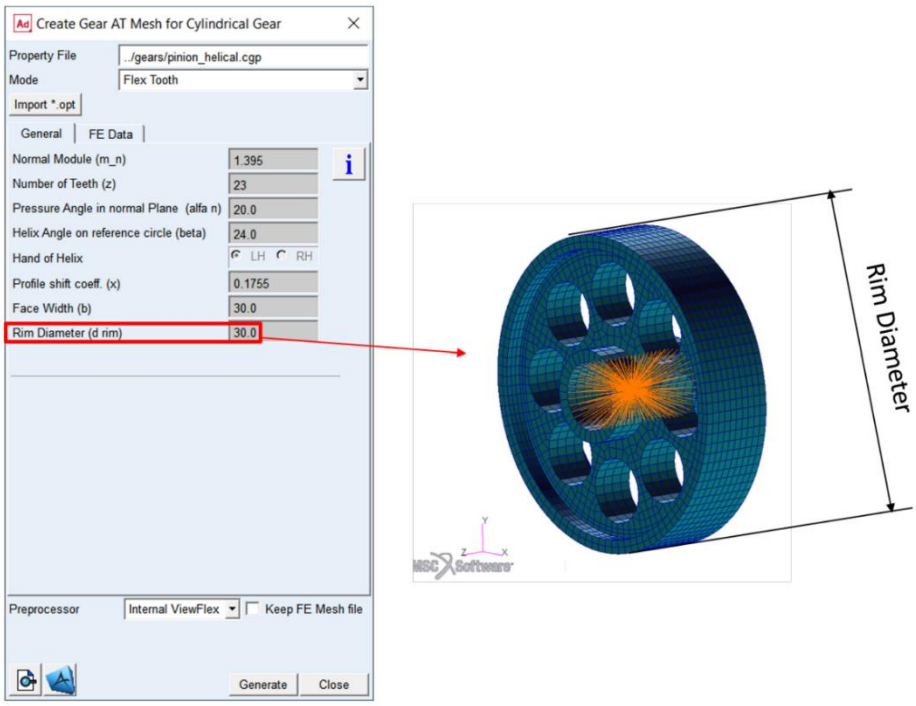


*Figure 16: Common Rim Diameter for wheel body and gear rim [7]*

The MNF of the wheel body is obtained through the execution of a SOL103 (Linear Eigenvalues Analysis) by exploiting the previously mentioned NASTRAN solver. To obtain the MNF it is necessary to import the mesh file (.bdf) within the Gear AT environment. Such mesh file should contain the wheel body without the gear rim as shown in Figure 15 and its external radius must be equal to the *Gear Rim Diameter* (Figure 16) defined during the first step so that the NASTRAN solver can detect contact surfaces of wheel body and gear rim. If the two surfaces are within a tolerance of 0.05 mm Gear AT mesher glues them together by means of the NASTRAN glued contact feature [12]. This latter allows to connect surfaces with two different mesh densities, as for the case of wheel body and gear rim, a condition that is usually preferrable to accurately describe the interactions at tooth level while trying to reduce computational costs.

From a practical perspective to connect the gear rim to the wheel body it is necessary to refer to a node in the middle of the gear width that lies on its

rotation axis. Such a node will be taken as interface node during the dynamic reduction and must be the independent node of an RBE2 or the dependent node of an RBE3. In the Adams Machinery User's Guide [7] it is not specified whether an RBE2 is better than an RBE3 for flexible gear system applications or vice versa, the only limitation in that regard is that one must preserve all six DoF of the reference node for the generation of the MNF (ASET DoF: 123456 [10]), as shown in Figure 17.

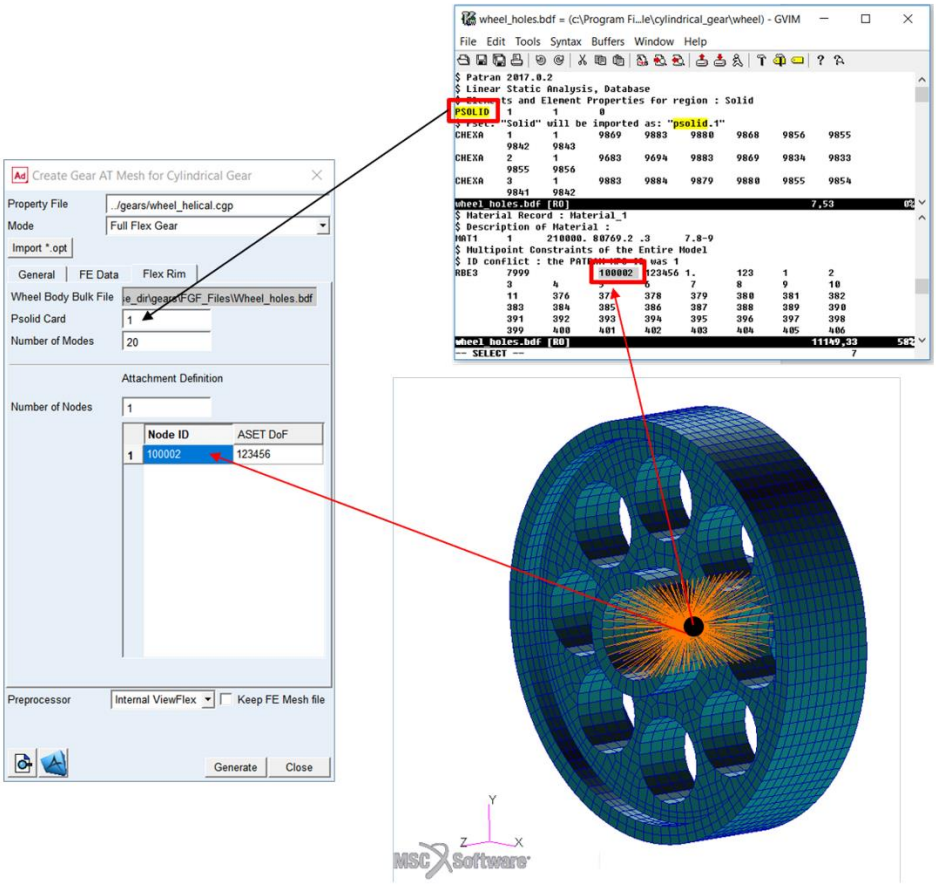


*Figure 17: Generation of the wheel body MNF*

Through the option *Full Flex Gear*, it is possible to consider the wheel body flexibility but not to consider the eventual shaft flexibility at which the wheel body is attached. To consider the two as a unique body one should avoid this option and select *Multi Gear Shaft*.

After the completion of this step the gear property file is modified to refer to the now available information on stiffness, gear mesh and/or shaft mesh.

### Multi Gear Shaft

This option is only available for cylindrical gear models (both spur and helical gears) and it allows the user to follow the same procedure previously described for the Full Flex Gear option but allowing one to obtain an MNF of a complete gear shaft (considering gear teeth, wheel body and shaft as a unique deformable body). To select this option one should avoid passing from Full Flex Gear, after the pre-processing of the tooth mesh (through the Flex Tooth option) the user must exit from Gear AT Mesh and select Multi Gear Shaft.

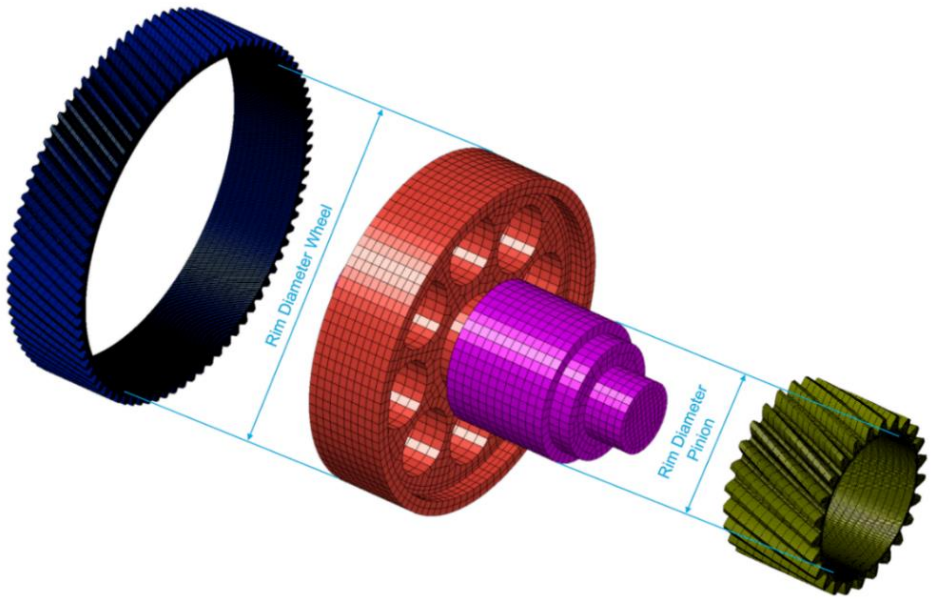


*Figure 18: Joining process description for Multi Gear Shaft option [7]*

In Figure 18 the components that play a role in the generation of the MNF are the same as the Full Flex Gear option but instead of a wheel body it is now possible to introduce the mesh file of a shaft with multiple gears on it. Since in this case more than one gear rim must be glued to the shaft it is necessary to

refer each gear to the right node as described for the Full Flex Gear option. Both for this option and for Full Flex Gear, once the MNF is created, this should be imported into the model and positioned coherently with the correspondent Gear AT Element orientation. After the completion of this step the gear property file is modified to refer to the now available information on stiffness, gear mesh and/or shaft mesh.

### Gear AT Element

The Gear AT Element represents the gear model by storing all the parameters obtained up to now in the Adams View model database. After the definition of a Gear AT Element the gear model will be visible in the user interface, and one can access it through the objects list on the left part of the screen.

To create a Gear AT Element it is necessary to define the marker with respect to which the gear model will be referred. This marker, which is called *reference marker*, must lie on the rotation axis of the gear, in the middle of the gear width and must have its z-axis oriented according to the rotation axis of the gear.

During the creation/modification of a Gear AT Element, it is possible to consider the previously defined profile modifications by simply clicking on a flag in the Gear AT Element window. In Gear AT, the micro-geometry modifications of the tooth profile are considered as a very fine mesh based on the deviation from the uncorrected (macro-)mesh. This fine mesh is used to solve contact between tooth flanks; loads are then transferred to the latter mentioned mesh in an iterative process during the simulation.

Once the user has indicated the property file of the gear model the software will automatically select the .shl file, obtained in previous steps, for the visualization of the gear in the user interface.

**Gear AT Force**

This last step defines a gear pair contact force for previously created Gear AT Elements, exploiting the .CGS files (containing stiffness properties of the gears) for the definition of the contact forces. Each Gear AT Force can only be defined for a single gear pair, where one gear will be denominated *Gear 1* and the other will be *Gear 2.* There are two possible cases:

- If gears are both external → Gear 1 will be the one with smaller width
- If one gear is internal → That gear will be Gear 2

Several parameters can be changed during the creation/modification of a Gear AT Force regarding:

- Contact mode
- Friction
- Damping (provided by oil film between mating gear teeth)
- Lubrication

About the contact mode, there are four possible options that allow one to execute system simulation with different levels of detail:

- *Gear FAST*
- *Rigid Contact*
- *Flexible Tooth*
- *Full Flex Gear*

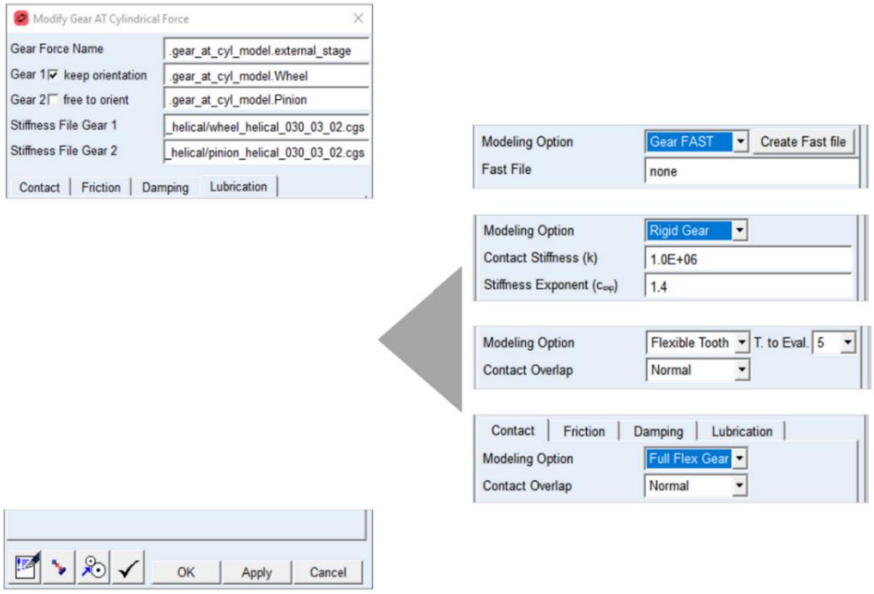


*Figure 19: Contact modeling option for Gear AT Force [7]*

In Figure 19 it is possible to see how to select different modeling options for Gear AT Force.

Besides the *Gear FAST* option which offers pre-computed contact formulation for preliminary studies, the other three options exploit a contact-to-contact algorithm for the contact detection, considering also the contribution of micro-geometry. For what concerns the contact forces, a distinction must be done between *Rigid Contact* option and *Flexible Tooth/Full Flex Gear* options.

For *Rigid Contact* the contact forces are calculated following the equation below:

$$F_{cnt} = k \cdot \delta^{c_{exp}}$$

Where:

- k is the contact stiffness
- $\delta$ is the penetration evaluated as the overlap of the tooth flank surface of *Gear 1* into *Gear 2*
- $c_{exp}$ is the (contact) exponent of the force law

When defining a Gear AT Force using the *Rigid Contact* mode, it is possible to set contact stiffness and stiffness exponent. Therefore, the system is characterized by a non-linear description of the contact force (*Hertz Contact*).

Whereas, if one selects Full Flex Gear or Multi Gear Shaft option, the contact force considers the contribution of teeth and/or teeth and wheel body compliances, thus the stiffness exponent is usually only slightly higher than one leading the system to exhibit a more linear behavior. For both options it is possible to select the amount of the so-called *Contact Overlap* that works as an additional 'flexibility' for the flank surface (which has a small contribution compared to the tooth flexibility) which allows to prevent poor quality results in very high or very small loading conditions, by setting *Small* or *High* respectively.

From a modeling point of view, it is essential to distinguish between the *Full Flex Gear* option and the *Multi Gear Shaft* option. The former allows one to consider the flexibility of gear tooth and wheel body only (not considering shaft flexibility) and requires the MNF of the wheel body created in the Gear AT Mesh pre-processing phase by selecting the same option. Whereas the latter permits one to consider tooth, wheel body and shaft as a unique deformable body and it requires the *Flexible Tooth* option in the Gear AT Force definition.

Once a new Gear AT Force is created the so-called *contact coordinate system* (CCS) is created:

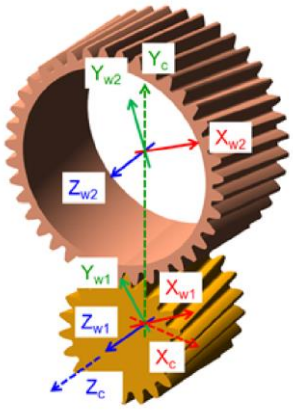


*Figure 20: CCS example for helical gear pair [7]*

As shown in Figure 20, the CCS is unique for each gear pair for which the Gear AT Force has been created. It consists of a reference frame having origin on the reference marker of Gear 1 with the Y-axis that passes through the reference markers of both gears. With the Z-axis coinciding with that of Gear 1, the Y- and X-axis represent respectively the radial and tangential directions for the contact forces.

After a simulation, forces between gears can be displayed separately as a radial and tangential contribution (represented in the CCS), or as total forces on single teeth by exploiting the numbering convention shown in Figure 21:

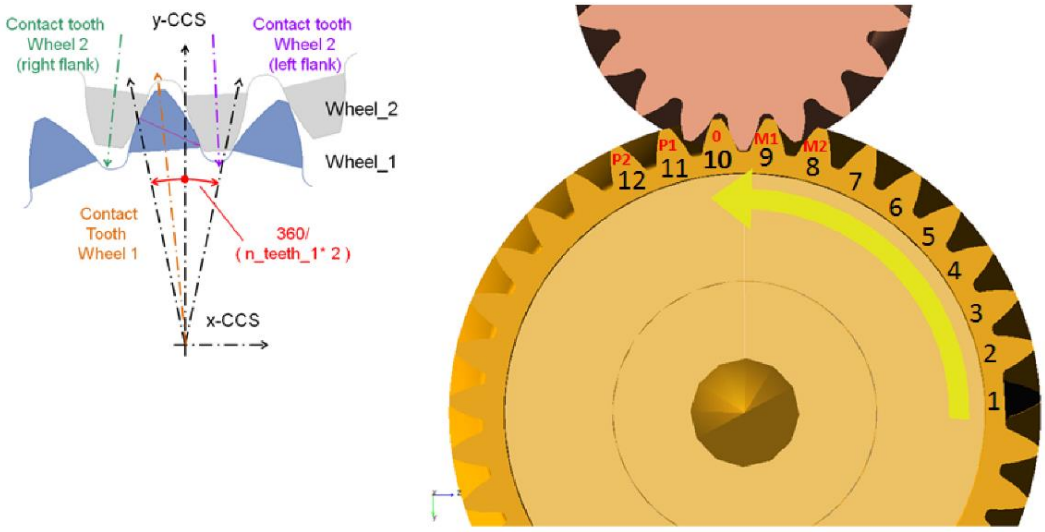


*Figure 21: Teeth enumeration convention for Gear AT Results [7]*

Where tooth 0 is the one with the smallest deviation from the Y-Z plane of the CCS and teeth from -2 to +2 (M2, M1, 0, P1, P2) follow the rule of the right hand with the thumb in the Z-axis direction of gear 1. This numbering convention allows one to have a visualization of the contact ratio of the gear pair because it is quite easy to see when the contact is sustained only by a pair of teeth or by two pair of teeth.

An example of Gear AT results is shown in Figure 22:

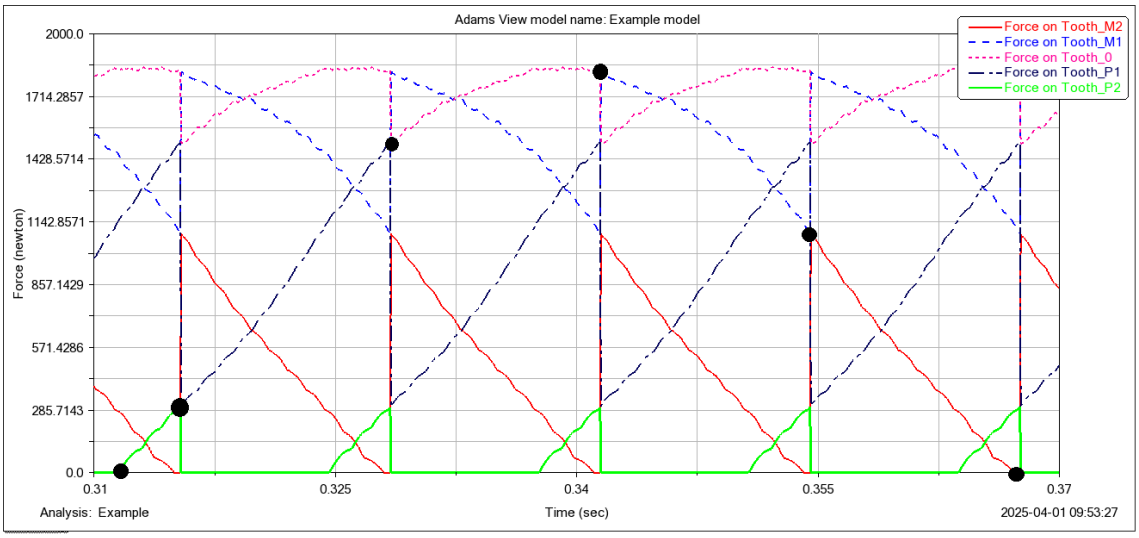


*Figure 22: Contact forces for helical gear pair*

The graph above was obtained from a helical gear pair provided as an example for Gear AT users (see reference [16] to learn more about this example). Each black dot in the figure represents a point in which the name of that tooth changes during the simulation (from P2 to P1 and so on). If one follows the curve with the black dots from left to right, it is possible to describe the loading/unloading cycle of each tooth during the simulation.

The results related to teeth forces shown in chapter 4 will follow this convention.

# 2. 4DOF ROTOR MODEL

In this chapter, the test case of a 4-DOF rotor model developed in MSC.Adams is presented. A preliminary study was performed by comparing it with an equivalent model implemented in MATLAB.

The chosen model serves to gain familiarity with the software and to evaluate its performance in the execution of:

- Modal analysis
- Dynamic simulation of (rigid) rotors

Two configurations of the model were constructed:

- "Disc" model
- "Long rotor" model

As thoroughly described in [1], a 'disc' denotes a rotor whose polar moment of inertia $J_p$ exceeds its transverse moment of inertia $J_t$ ($J_p > J_t$), whereas a 'long rotor' denotes a body whose transverse moment of inertia is greater than its polar moment of inertia ($J_p < J_t$).

Two distinct models were developed in order to achieve, in the case of the disc model, the best correspondence between the theoretical counterpart implemented in MATLAB and the model built in Adams; and, in the case of the long-rotor model, to excite at least two modes of the system by simulating a static unbalance of the shaft during a dynamic simulation.

Such unbalance is produced, for both models, by applying an additional mass (implemented as a Part in Adams) attached to the disc via a joint that constrains all its degrees of freedom relative to the disc.

For both models, the following outputs were extracted:

- Campbell diagram of the system
- Rotor displacement in a dynamic simulation

The model developed via the MATLAB script, which will serve as the reference for the activities conducted in this chapter, is effectively a MATLAB implementation of the material presented in the theoretical introduction to the Jeffcott rotor. This model is used solely to generate a reference Campbell diagram, obtained by iteratively computing the gyroscopic matrix over a range of rotor rotational speeds.

## 2.1. "Disc" model

The model is depicted in the following schematic (Figure 23):

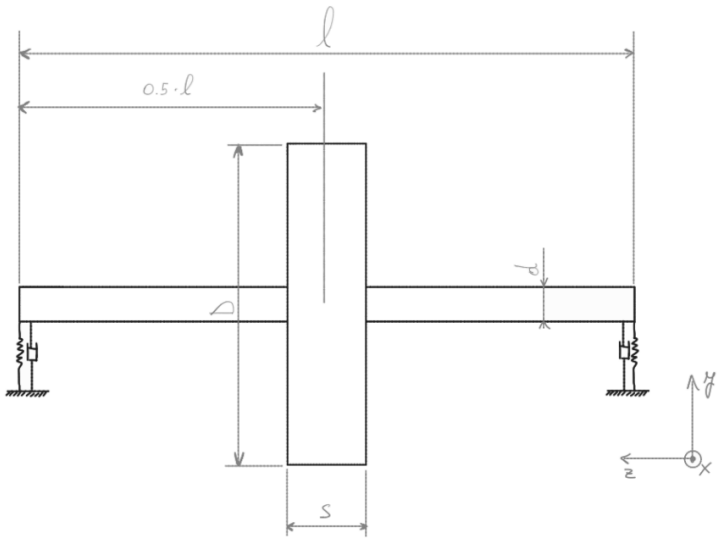


*Figure 23: Disc model scheme*

Where:

- $l = 500mm$
- $d = 20mm$
- $s = 20mm$
- $D = 300mm$

As for the system's mass properties:

- $J_p = 1.241e + 05kg \cdot mm^2$

- $J_t = 6.240\text{e} + 04\text{kg} \cdot mm^2$
- $m = 11.03\ kg$

To construct a model as close as possible to its theoretical counterpart, the shaft to which the disc is attached is assumed to be massless; therefore, the mass indicated above pertains solely to the disc.

The model in Adams is shown in the following figure (Figure 24):

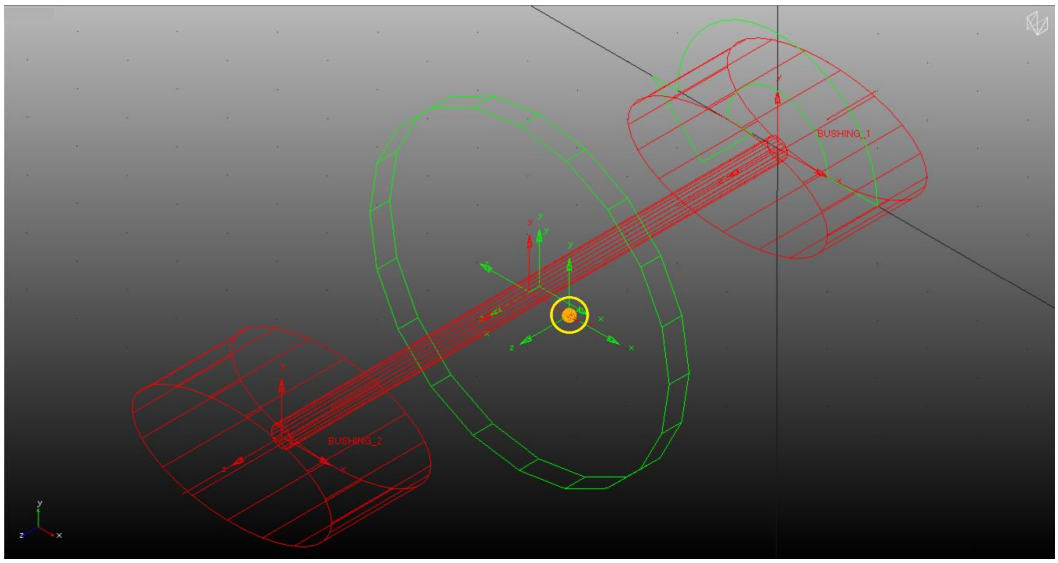


*Figure 24: Disc model in Adams*

The mass highlighted in yellow is used to simulate the shaft unbalance. This point mass is placed at an eccentricity $e$ of 1 mm and has a mass $m$ of 1 kg. The Z axis is the rotor's axis of rotation, and the X and Y axes lie in the plane of the disc.

The rotor is constrained to ground by elements called *bushings*, represented in the software as red ovals located at the shaft ends, as shown in the figure. These constraints behave as stiffness and/or damping elements and, in the present model, act along the $x$ and $y$ directions.

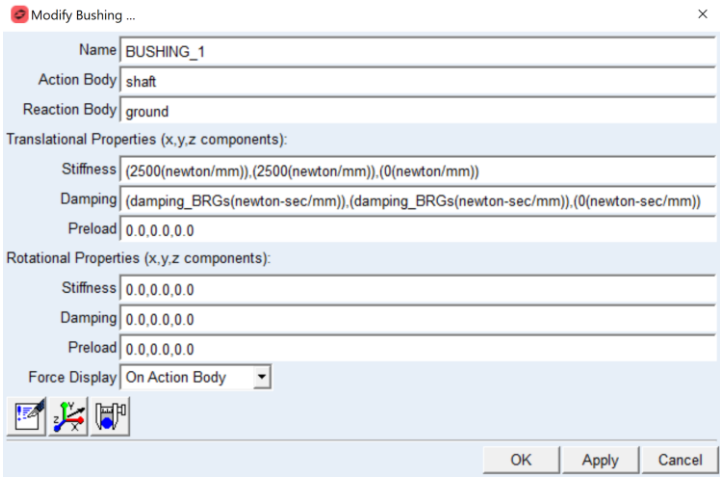


*Figure 25: Stiffness and damping values of the constraints*

In Figure 25, the stiffness and damping values associated with the bushings are reported. Only translational stiffness and damping have been assigned, and only along the $x$ and $y$ axes, as indicated by the last value, corresponding to the $z$-axis, which has been left at 0. The damping value will be modified later in the simulations to assess its effects.

An additional constraint (not visible in fig. 21) was imposed on the system to suppress the axial degree of freedom.

The green arrow located at one end of the shaft in fig. 21 represents the imposed rotational motion applied to the system for dynamic simulation. As can be seen in the figure, the imposed motion is a rotation of the rotor about the $z$ axis.

### Campbell diagram comparison

For the construction of the Campbell diagram in Adams/View, a simulation called *Rotor Dynamic Simulation Series* (circled in red in fig. 23) was executed. This procedure enables a sequence of dynamic simulations, at the end of each of which the system's eigenvalues are extracted.

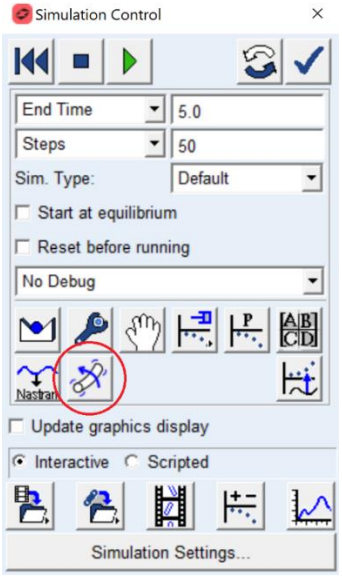


*Figure 26: Rotor Dynamic Simulation Series from "Simulation Control" panel*

In Figure 26, the option used for the simulation aimed at obtaining the Campbell diagram is circled in red.

The speed profile followed by the system during the simulation is prescribed as in any other simulation; in this case, a constant acceleration of 5 rev/s$^2$ was imposed:

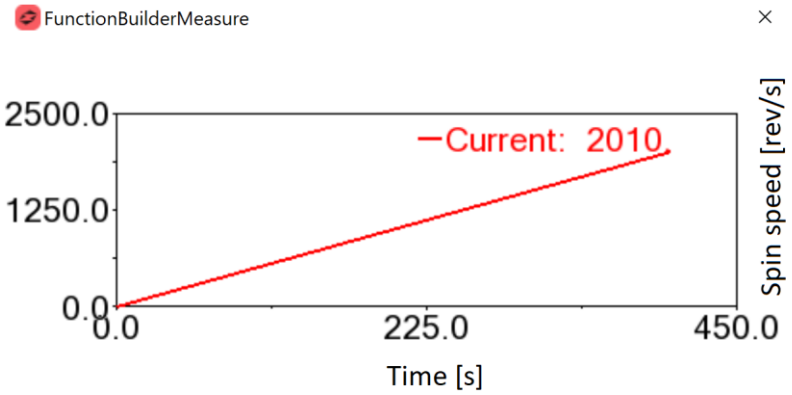


*Figure 27: Imposed angular velocity profile for Campbell diagram*

As can be seen from the graph above (Figure 27), the maximum speed reached during the simulation is 2010 rev/s in 402 s. In this case, the eigenvalues were

extracted every 2 s of simulation time, corresponding to a speed increment of 10 rev/s at each step.

The resulting output from this simulation is as follows:

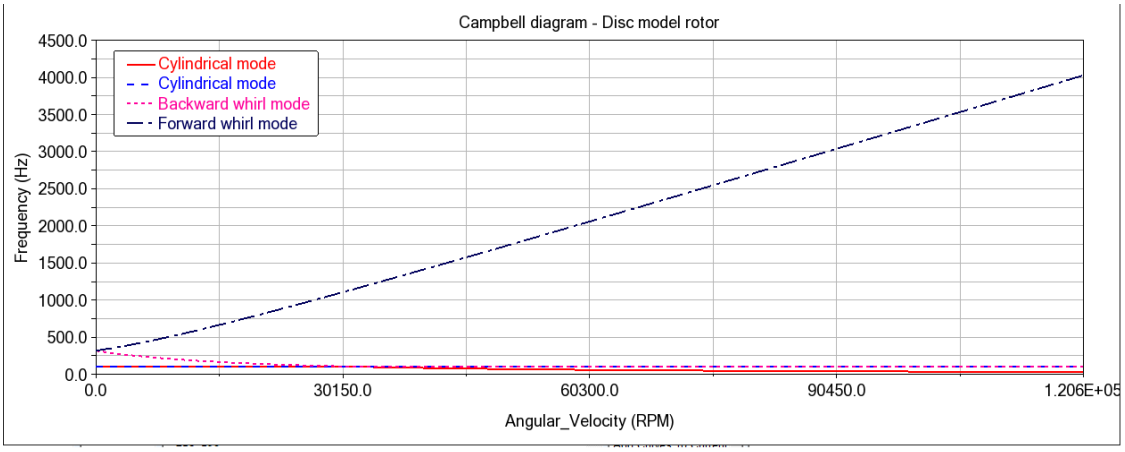


*Figure 28: Campbell diagram of the Adams model*

As shown in the graph extracted from Adams/PostProcessor (Figure 28), the influence of the gyroscopic effect on the backward and forward whirl modes is evident, whereas, as predicted by theory, this effect is negligible for the system's cylindrical modes.

Quantitatively, this result is corroborated by comparison with the MATLAB model (Figure 29), which exhibits an almost perfect agreement with the obtained plots.

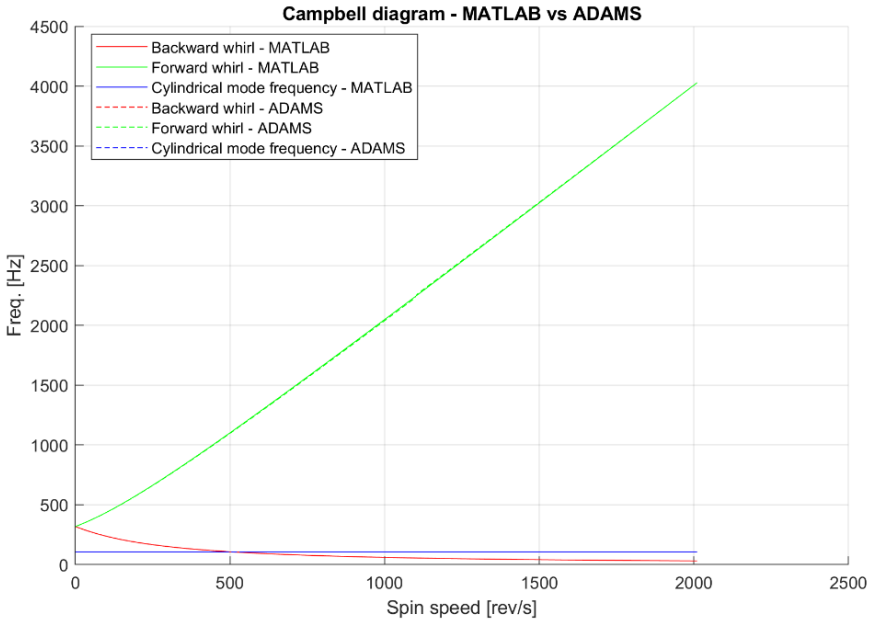


*Figure 29: Campbell diagram comparison between Adams and MATLAB models*

The dashed lines represent the results obtained with the model developed in Adams/View, and as can be observed, these are almost perfectly superimposed on the solid curves representing the values obtained with the MATLAB model. The largest discrepancy between the two models is 0.47%, identified in the forward whirl mode.

### Dynamic simulation with unbalance

For the simulations presented in this section, the following options were selected:

- Time step size = $10^{-4}$ s
- Time duration = 40 s

For all simulations, the following speed profile was imposed (Figure 30):

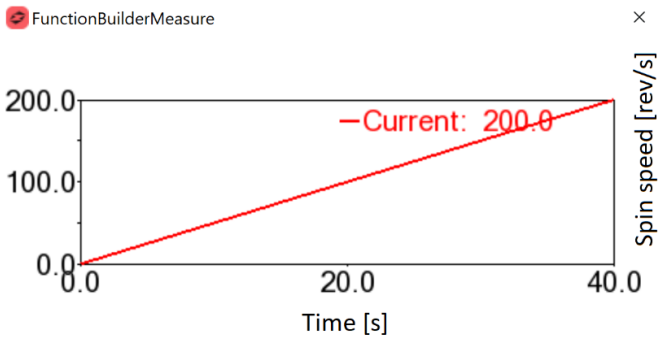


*Figure 30: Imposed angular velocity profile for transient analysis*

In this case as well, a constant acceleration of 5 rev/s$^2$ was imposed, bringing the rotor's maximum speed to 200 rev/s at the end of the simulation. The acceleration and simulation duration parameters were chosen to allow the system's forcing, in this case the rotor's static unbalance, to reach the critical speed of the cylindrical mode, so as to qualitatively assess the effects of different damping values applied to the supports.

The modal frequencies of the system at zero speed and at the critical speed are reported below (Table 1):

| Mode number | Frequencies at $\Omega = 0$ | Frequencies at $\Omega = \Omega_{crit}$ |
|---|---|---|
| 1 | 106.19 Hz | 106.19 Hz |
| 2 | 106.19 Hz | 106.19 Hz |
| 3 | 318.50 Hz | 233.62 Hz |
| 4 | 318.50 Hz | 444.73 Hz |

Table 1: Model frequency at stand still and at critical speed

In this case, the forcing term by its nature has the same frequency as the rotor's rotational speed; therefore, the critical speed will be equal to $\Omega_{crit} = 106.19\, rev/s$:

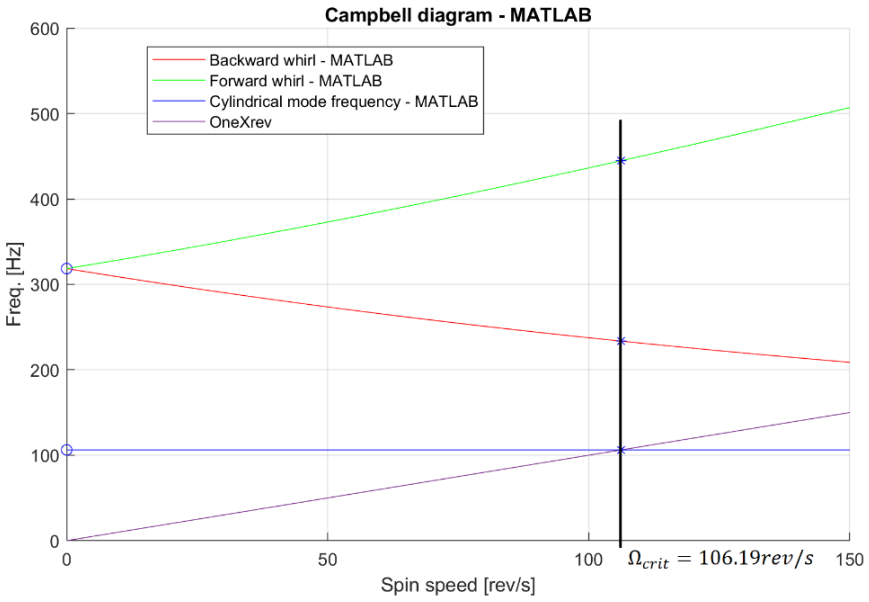


*Figure 31: Campbell diagram with critical speed crossing*

In Figure 31 it is possible to see the crossing of the unbalance force frequency with the critical speed for the cylindrical mode of the system.

With the acceleration imposed on the system, the critical speed is reached at approximately 21.24 s during the simulation; therefore, around that instant, an excitation of the first mode is expected.

To observe the crossing of the first mode by excitation, the displacement along the X direction, perpendicular to the axis of rotation, was extracted:

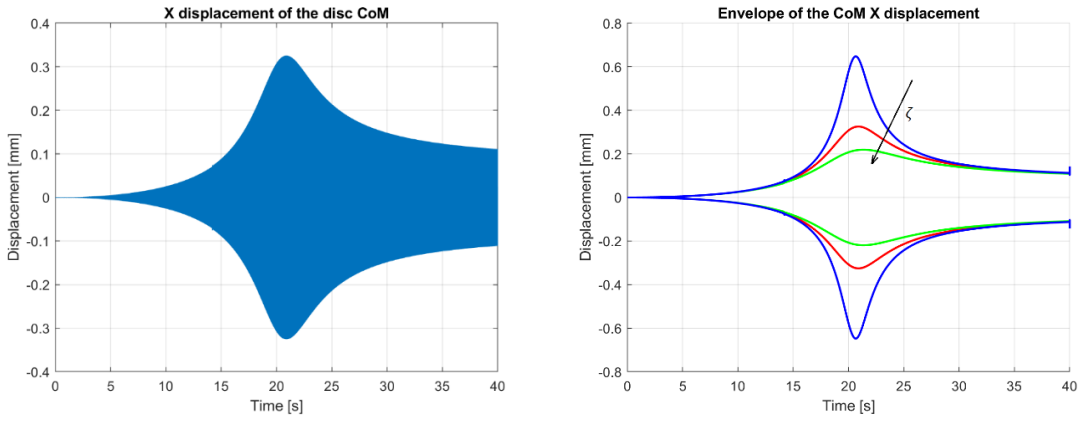


*Figure 32: Center of Mass (CoM) x-displacement for different damping ratios*

As previously anticipated, a marked increase in the oscillation amplitude can be observed shortly after 20 s of simulation.

Three different simulations were performed with three distinct damping values applied to the connections:

- Case 1 (green): 1.5 Ns/mm → $\zeta = 0.19$
- Case 2 (red): 1.0 Ns/mm → $\zeta = 0.13$
- Case 3 (blue): 0.5 Ns/mm → $\zeta = 0.06$

From the results obtained, it can be concluded that, at least from a qualitative standpoint, the model responds as predicted by theory to the presence of a static unbalance and to the addition of damping at the connections.

## 2.2. "Long rotor" model

The model is depicted in the following schematic (Figure 33):

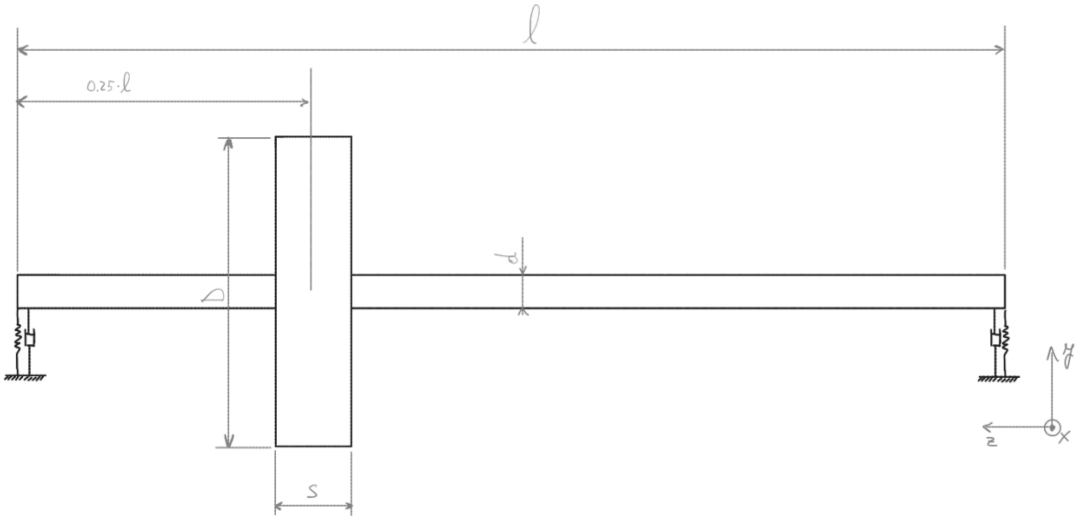


*Figure 33: Long rotor model scheme*

Where:

- $l = 1000mm$
- $d = 20mm$

- $s = 20mm$
- $D = 300mm$

As for the system's mass properties:

- $J_p = 1.242e + 05kg \cdot mm^2$
- $J_t = 3.920e + 05kg \cdot mm^2$
- $m = 13.48\,kg$

The principal differences from the previous model lie in the presence of a shaft with non-negligible mass, sufficiently long to yield $J_t > J_p$, and in the placement of the disc, which in this case is no longer at the rotor's center.

The need to achieve a transverse moment of inertia greater than the polar moment arises from the attempt to excite the forward whirl mode via an unbalance-like excitation. The disc's placement and the resulting shift of the rotor's center of mass also promote excitation of the aforementioned mode; however, this configuration likewise enhances coupling between the translational and rotational degrees of freedom. Consequently, the modes are no longer purely conical or cylindrical but are instead predominantly conical- or cylindrical-type. The model is shown in Figure 34:

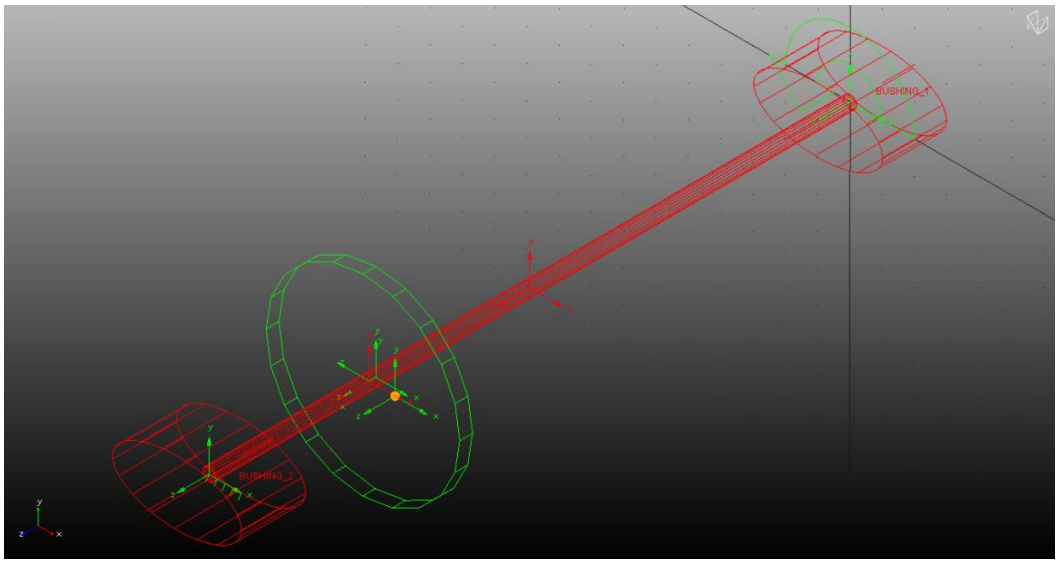


*Figure 34: Long rotor model in Adams*

The model exhibits the same stiffness properties at the connections; the damping will be varied across the different cases during the dynamic simulations, as was done in the previous case.

### Campbell diagram comparison

In this case as well, to obtain the system's Campbell diagram from the Adams/View model, a *Rotor Dynamic Simulation Series* was carried out. The simulation was executed with the same settings and inputs as in the previous case, reported below:

- Time duration = 402 s
- Step time size = $10^{-4}$ s
- (Constant) angular acceleration = 5 rev/s$^2$

The resulting diagram, generated with Adams/PostProcessor, is as follows:

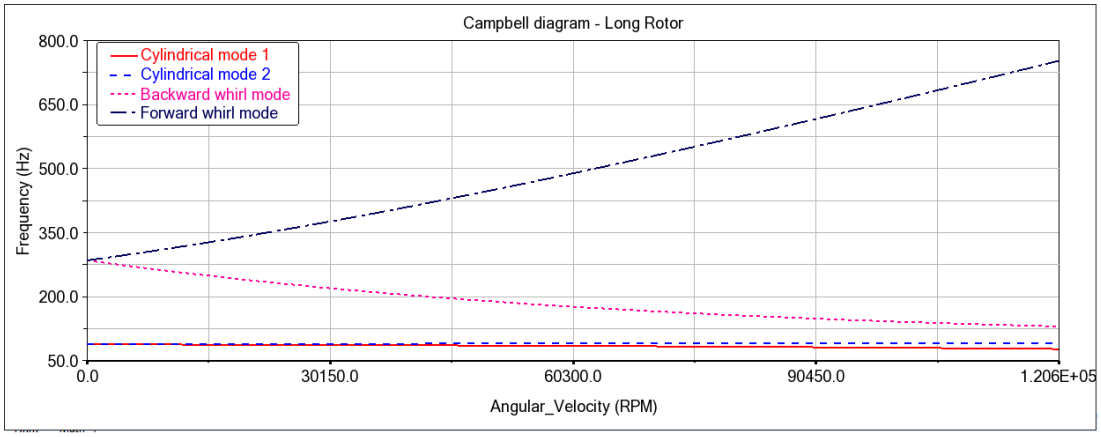


*Figure 35: Campbell diagram of the Adams model*

From the graph (Figure 35) it can be observed that, in this case, the cylindrical modes exhibit a slight dependence on angular speed, an effect which, as anticipated above, is caused by the coupling between the translational and rotational degrees of freedom.

The comparison with the equivalent MATLAB model yields the following results (Figure 36):

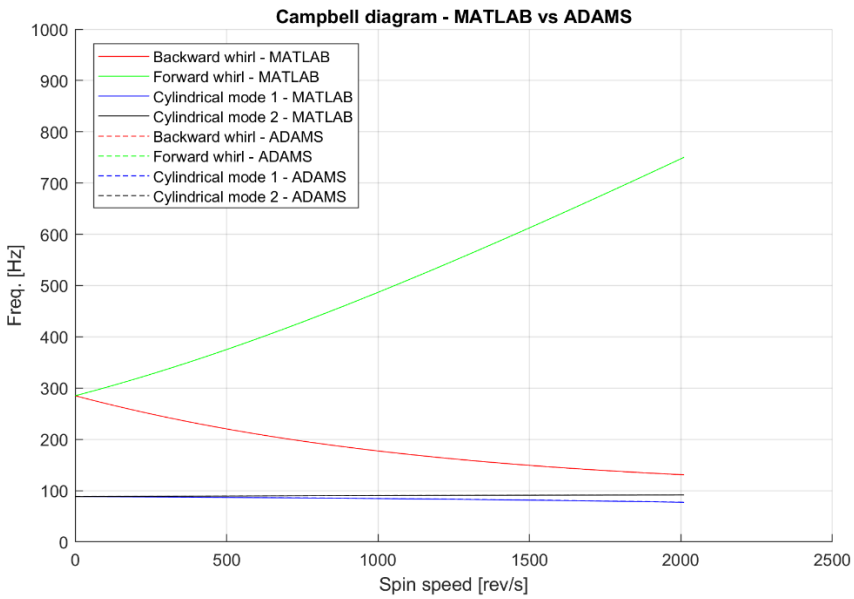


*Figure 36: Campbell diagram comparison between Adams and MATLAB models*

In this case as well, the differences between the MATLAB model and the one developed in Adams/View are negligible; in particular, a maximum error of 0.5% is obtained with respect to the value computed by the MATLAB script for one of the two (predominantly) cylindrical modes.

### Dynamic simulation with unbalance

For the simulations presented in this section, the following options were selected:

- Time step size = $10^{-4}$ s
- Time duration = 500 s

In this case, the angular speed profile imposed on the rotor differs from the previous one:

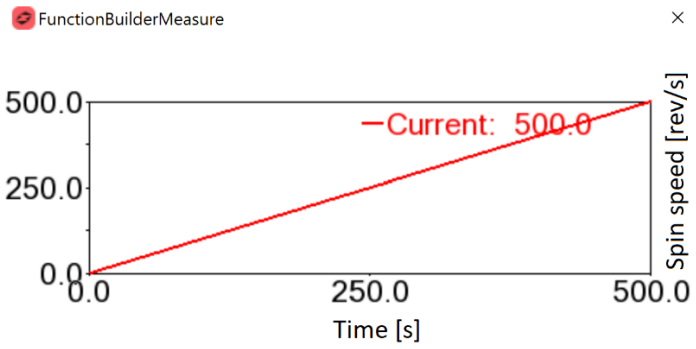


*Figure 37: Imposed angular velocity profile for transient analysis*

An angular acceleration of 1 rev/s$^2$ was imposed to reach a speed of 500 rev/s in 500 s, as can be seen in Figure 37. The rationale for selecting a lower acceleration and a much longer simulation duration is to promote excitation of the forward whirl mode, which is more difficult to trigger than the system's first cylindrical mode and occurs at a much higher critical speed.

In this case, in fact, there are two critical speeds to be reached, as shown in the following graph (Figure 38):

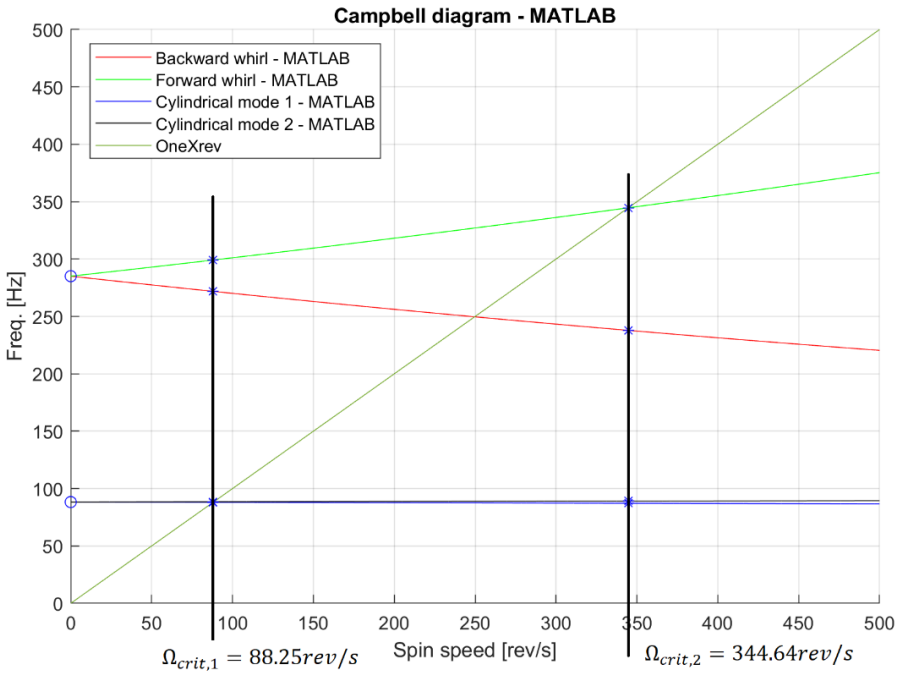


*Figure 38: Campbell diagram with critical speed crossings*

The modal frequencies at zero speed and at critical speeds are as follows (Table 2):

| Mode number | Frequencies at $\Omega = 0$ | Frequencies at $\Omega = \Omega_{crit,1}$ | Frequencies at $\Omega = \Omega_{crit,2}$ |
|---|---|---|---|
| 1 | 88.26 Hz | 88.25 Hz* | 87.22 Hz |
| 2 | 88.26 Hz | 88.25 Hz* | 89.10 Hz |
| 3 | 285.10 Hz | 299.1 Hz | 237.90 Hz |
| 4 | 285.10 Hz | 271.9 Hz | 344.64 Hz |

Table 2: Center of Mass (CoM) x-displacement for different damping ratios

Where the first critical speed was obtained as the mean value of the two speeds 88.01 rev/s (crossing with the first cylindrical mode) and 88.49 rev/s (crossing with the second cylindrical mode).

Given that an angular acceleration of 1 rev/s$^2$ was imposed, increases in oscillation amplitude due to the excitation of the cylindrical modes and the forward whirl mode are expected at approximately 88.25 s and 344.64 s of simulation, respectively.

Below (Figure 39) are the displacements of the disc along the X axis (perpendicular to the axis of rotation):

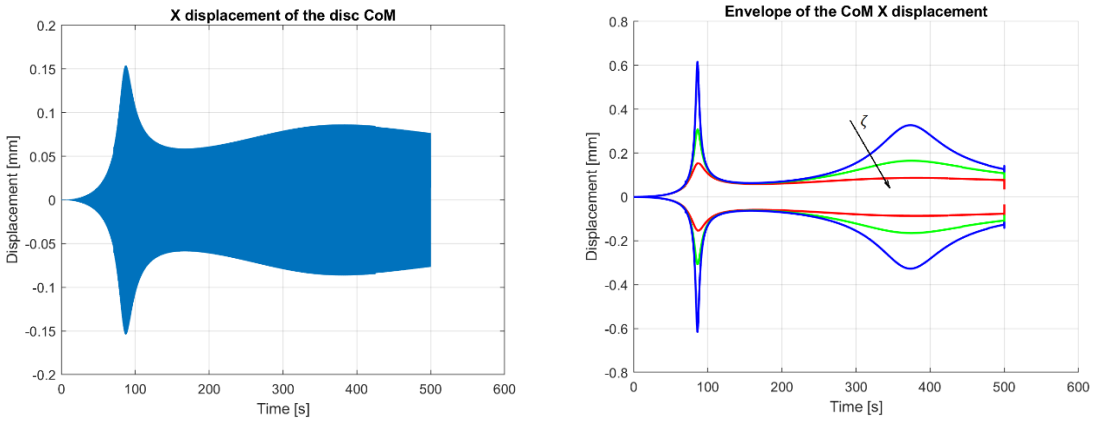


*Figure 39: Center of Mass (CoM) x-displacement for different damping ratios*

In this case as well, three simulations were performed with three different damping values:

| Damping | Damping ratio ($\zeta$) | Critical speed |
|---|---|---|
| 1 Ns/mm | 0.11 | $\Omega_{crit,1}$ |
| | 0.38 | $\Omega_{crit,2}$ |
| 0.5 Ns/mm | 0.06 | $\Omega_{crit,1}$ |
| | 0.19 | $\Omega_{crit,2}$ |
| 0.25 Ns/mm | 0.03 | $\Omega_{crit,1}$ |
| | 0.10 | $\Omega_{crit,2}$ |

Table 3: Modal damping ratio for different values of constrains damping

For Table 3 damping ratio values were obtained through a modal analysis of the system performed within the software.

In this case as well, from a qualitative standpoint, damping reduces the amplitude of the system's response at the crossing of the two resonances.

# 3. FLEXIBLE ROTOR MODEL

In this chapter, a model similar to those described in the previous chapter will be presented; however, instead of a rigid shaft on compliant supports, a deformable shaft with ideal constraints (hinges) is considered. This model was developed primarily to explore and validate the capabilities offered by Adams/Flex for incorporating flexible bodies within a multibody simulation environment.

Figure 5.b (introduction) depicts a model similar to those in the previous chapter, whereas figure 5.a represents the model discussed in the current chapter.

### Creation of the flexible body

The incorporation of deformable bodies within Adams must be performed using one of the following two options:

- Use of the Adams View Flex option
- Import of a MNF (Modal Neutral File) generated by external software

The first option enables, through the NASTRAN solver included within the software, the automatic discretization of an already existing rigid part in the model.

The second option requires the use of external FEA software to generate the MNF file to be imported into Adams (see user guide). This latter approach was selected for the development of the model, as it provided full control over mesh generation.

In both cases, it is necessary to perform a reduction of the system's degrees of freedom at the interface nodes. These interface nodes represent the *attachment nodes* for the body within the software, and they serve as the points through which constraints, forces, and/or prescribed motions can be applied. To properly integrate the body within the software, each interface node must belong to an

RBE2/3 (Rigid Body Element), ensuring that each node contributes 6 degrees of freedom to the system. For the model under consideration, RBE2 elements were used [12].

The model is shown in Figure 40:

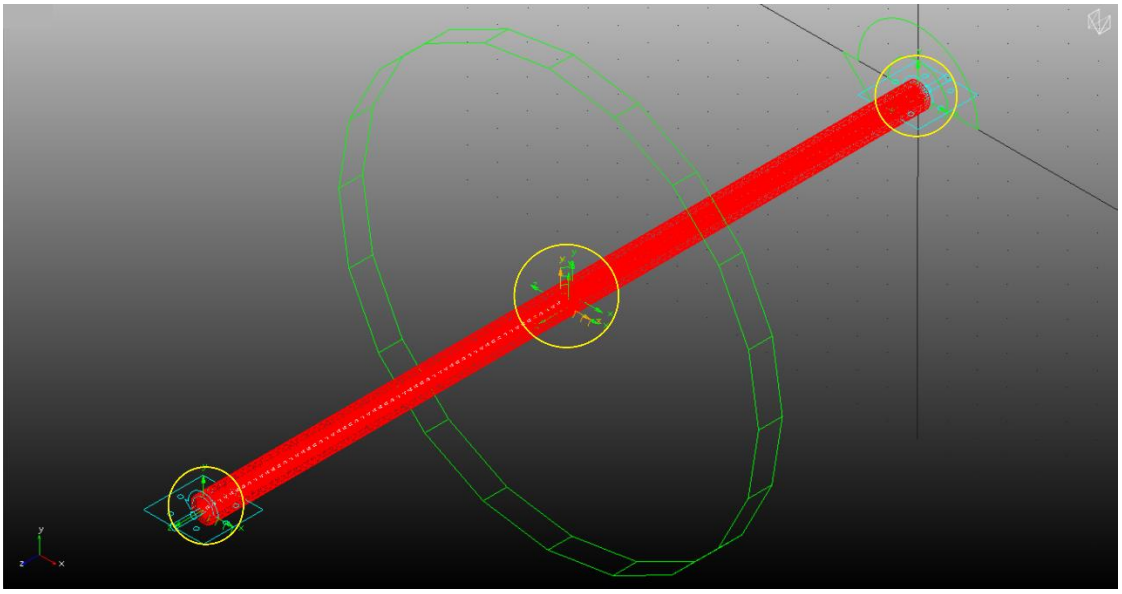

*Figure 40: Rotor model in Adams*

The only deformable component in the model is the shaft (shown in red), whereas the disk is modeled as an infinitely rigid component. The interface nodes selected for the reduction are circled in yellow; those at the ends serve to attach the rotor to ground via two hinges, while the midpoint node is used to connect the rigid disk to the shaft. As is evident from the figure above, the system is not constrained to the ground through the use of spring/damper elements, thus there is no contribution from non-rotating damping and the only kind of damping in the structure is given by the rotating damping on the flexible rotating shaft. By taking as an example the Jeffcott rotor model this condition would lead to a instability condition right after the flexural critical speed is crossed.

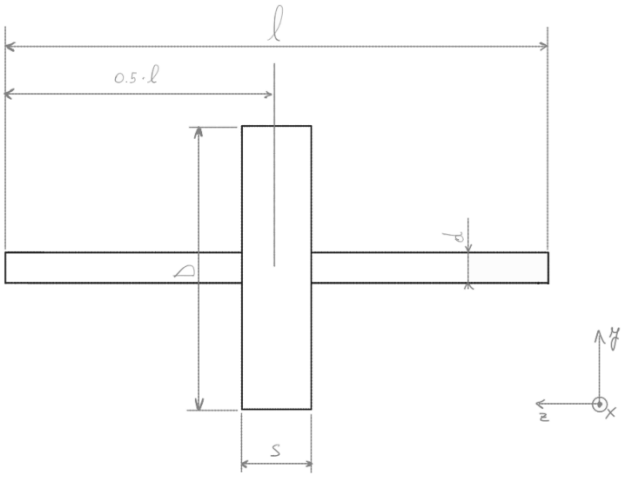


*Figure 41: Rotor model scheme*

In the schematic of Figure 41, the model dimensions are reported as follows:

- l = 1200 mm
- d = 40 mm
- s = 40 mm
- D = 700 mm

The flexible shaft, generated using the (external) NASTRAN solver, was created in two variants employing two different solution sequences:

- Card SOL 103 → Case 1
- Card SOL 107 → Case 2

Both solution sequences are used to perform a modal analysis of the component; however, in the latter case the component can be identified as a rotor, which enables accounting for effects such as centrifugal stiffening and gyroscopic coupling during simulation. To include these effects, the *Rotor Dynamics* option must be selected in Adams (see Figure 42).

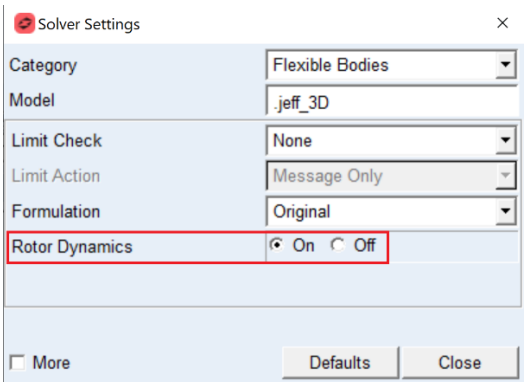


*Figure 42: Rotor Dynamics selection in Solver Settings*

## 3.1. Case 1 (SOL103)

The first step in developing the model is to generate the .mnf file for importing the deformable body into the software.

The file, containing information such as mass, stiffness, and (if requested) damping matrices, as well as the modal matrix, etc. [9], is generated via an Adams/NASTRAN interface command following a modal analysis performed using the SOL 103 sequence. The component was reduced at the interface nodes (as described above), truncating modes above 15,000 Hz.

### 3.1.1. Modal analysis comparison

An initial validation of the model was performed by comparing the system's modal frequencies, as represented in Fig. (screen), with those of the unreduced (FULL-3D) model to verify that both the reduction and the MNF file generation were carried out correctly. To enable a like-for-like comparison between equivalent models, *Single Point Constraints* (SPC1 card) were applied at the ends of the deformable shaft to represent the hinges used in the Adams model, and a *Concentrated Mass* (CONM2 card) was placed at the midspan of the shaft to represent the disk. For details regarding the NASTRAN cards employed, refer to the bibliographic source [12].

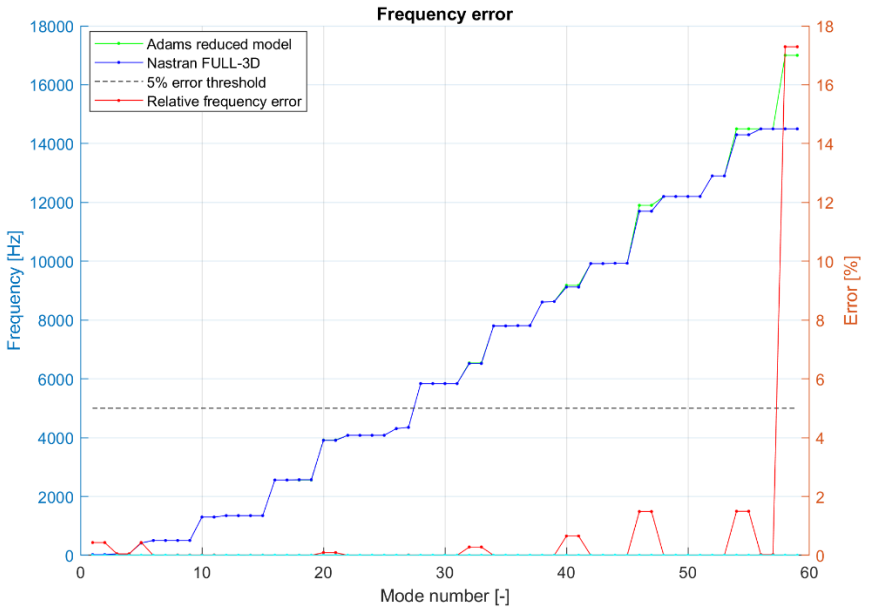


*Figure 43: Mode frequencies comparison between reduced model in Adams and full model (stand still)*

As can be seen from the plot of Figure 43, the relative error between the two models, the reduced model (Adams) and the unreduced model (NASTRAN), remains low for most modes, while it exceeds the 5% threshold substantially for the last two modes. Overall, it can be concluded that the model was imported correctly into Adams, since the final deviation in the modal frequency values is attributable to the reduction process applied to the deformable body, a process that, by its nature, introduces approximations.

### 3.1.2. Dynamic simulation

As carried out for the 4DOF rotor model, a dynamic simulation was performed in which the forcing due to the rotor's static unbalance was simulated by adding a point mass fixed to the rotating disk.

The imposed speed profile used for the simulation is shown in the following plot (Figure 44):

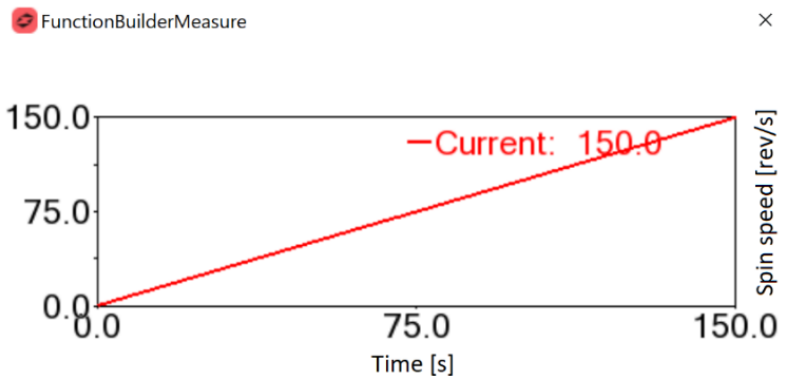


*Figure 44: Imposed angular velocity profile for transient analysis*

A constant acceleration of 1 rev/s$^2$ was imposed to reach a final speed of 150 rev/s in 150 s. The objective is to excite the first bending mode of the rotor at the crossing between the forcing frequency and the system's natural frequency.

The first ten modes of the system are as follows:

| Mode n° | Frequency [Hz] |
|---|---|
| 1 | 24.07 |
| 2 | 24.07 |
| 3 | 48.36 |
| 4 | 48.36 |
| 5 | 420.56 |
| 6 | 504.56 |
| 7 | 504.56 |
| 8 | 506.36 |
| 9 | 506.36 |
| 10 | 1304.46 |

Table 4: Frequencies of the first 10 modes

The highlighted frequencies in Table 4 correspond to the first bending mode of the rotor; therefore, given the imposed speed profile, the first critical speed is expected to be reached at 24.07 s of simulation.

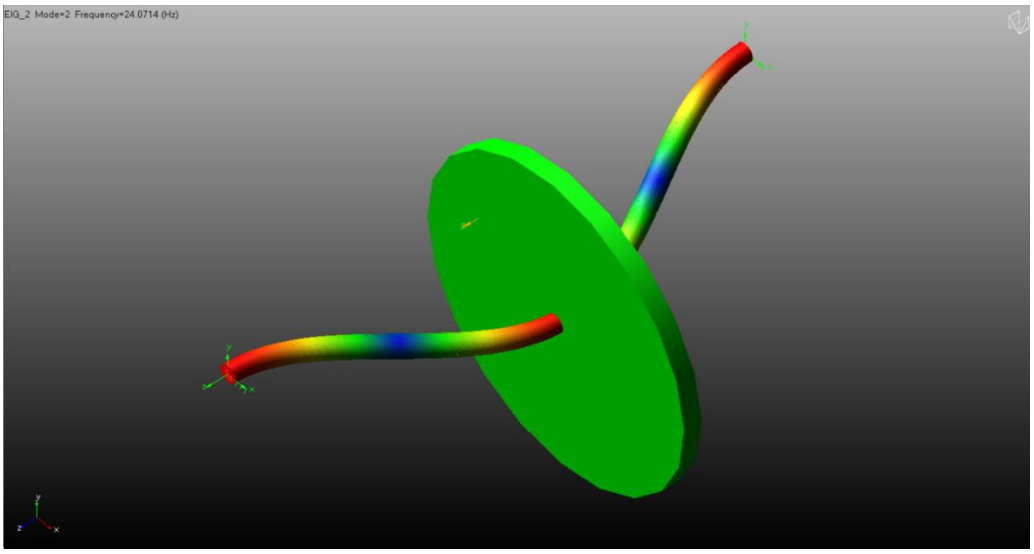


*Figure 45: First bending mode shape of the model*

Figure 45 shows the first bending mode of the system excited at the crossing of the first critical speed of the rotor.

A decisive factor influencing the simulation outcomes was the value of damping assigned to the rotating deformable structure. For a deformable body in Adams, there are two ways to assign damping:

- After importing the body into Adams, via the Damping Ratio setting
- Before import, within the FEA software during MNF file creation

In the first case, modal damping is applied, i.e., a specific damping ratio is assigned to each mode of the deformable body (see Adams/Flex). In the second case, proportional damping can be specified by defining Rayleigh coefficients to be used [12].

The simulations were performed using different damping values assigned to the rotating deformable component:

- Damping ratio (Adams) = 0% → For all modes
- Damping ratio (Adams) = 5% → For all modes
- Damping ratio (Adams) = 10% → For all modes
- Damping ratio (Adams) = 15% → For all modes

- Proportional damping (from NASTRAN)

For the first four simulations, the damping ratio was introduced after the import of the MNF of the flexible shaft, whereas for the last case the damping matrix was created before the generation of the MNF.

To act on both the contributions see the two highlighted options in Figure 46:

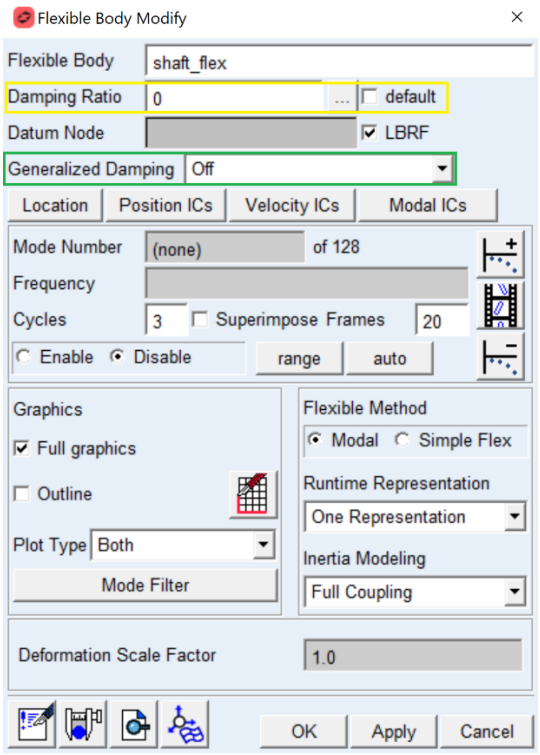


*Figure 46: Damping Ratio (Adams) and Generalized (External) damping*

By acting on the yellow highlighted option it is possible to introduce modal damping after MNF generation, whereas by acting on the green highlighted option it is possible to whether consider a generalized damping matrix that must have been created prior to MNF generation of the flexible body.

For each simulation, the displacement of the disk's center of mass along the x-axis was extracted, and a waterfall analysis was performed.

The results are presented in the following figures:

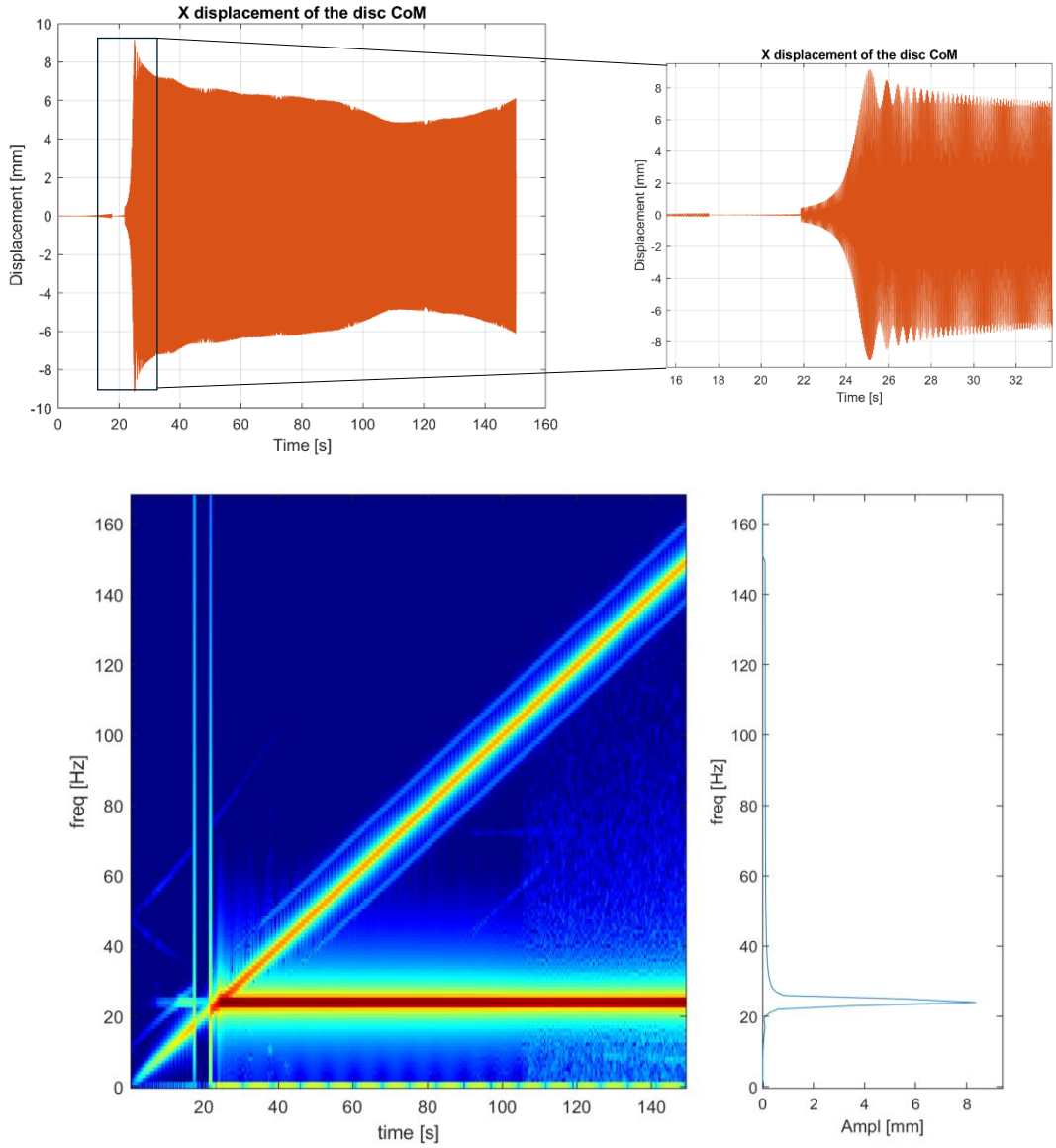


*Figure 47: CoM displacement and its waterfall for Damping Ratio = 0%*

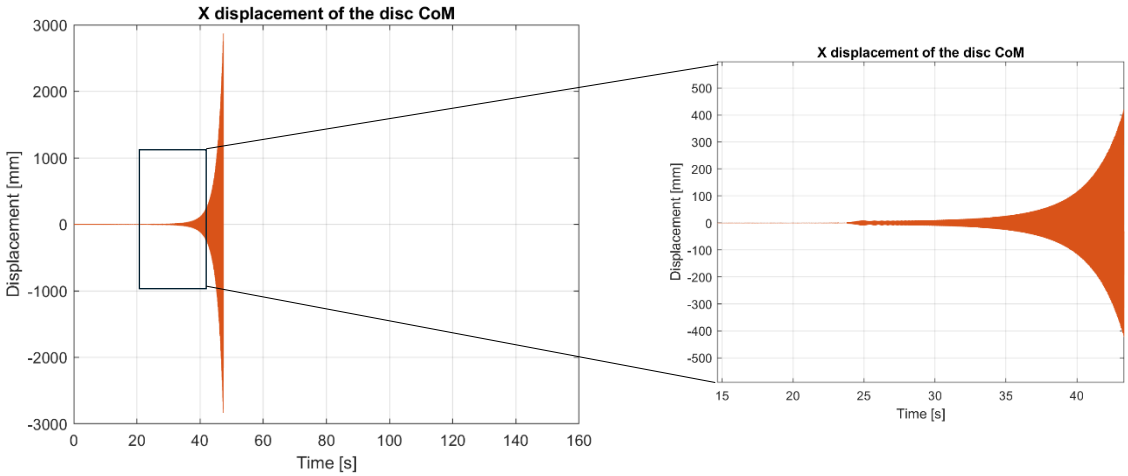


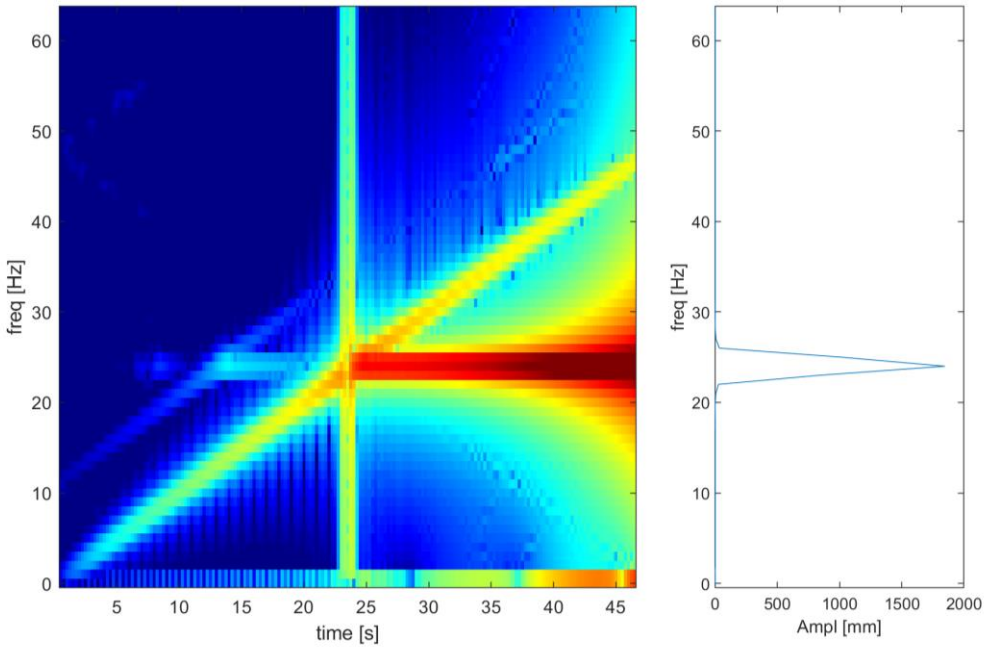


*Figure 48: CoM displacement and its waterfall for Damping Ratio = 5%*

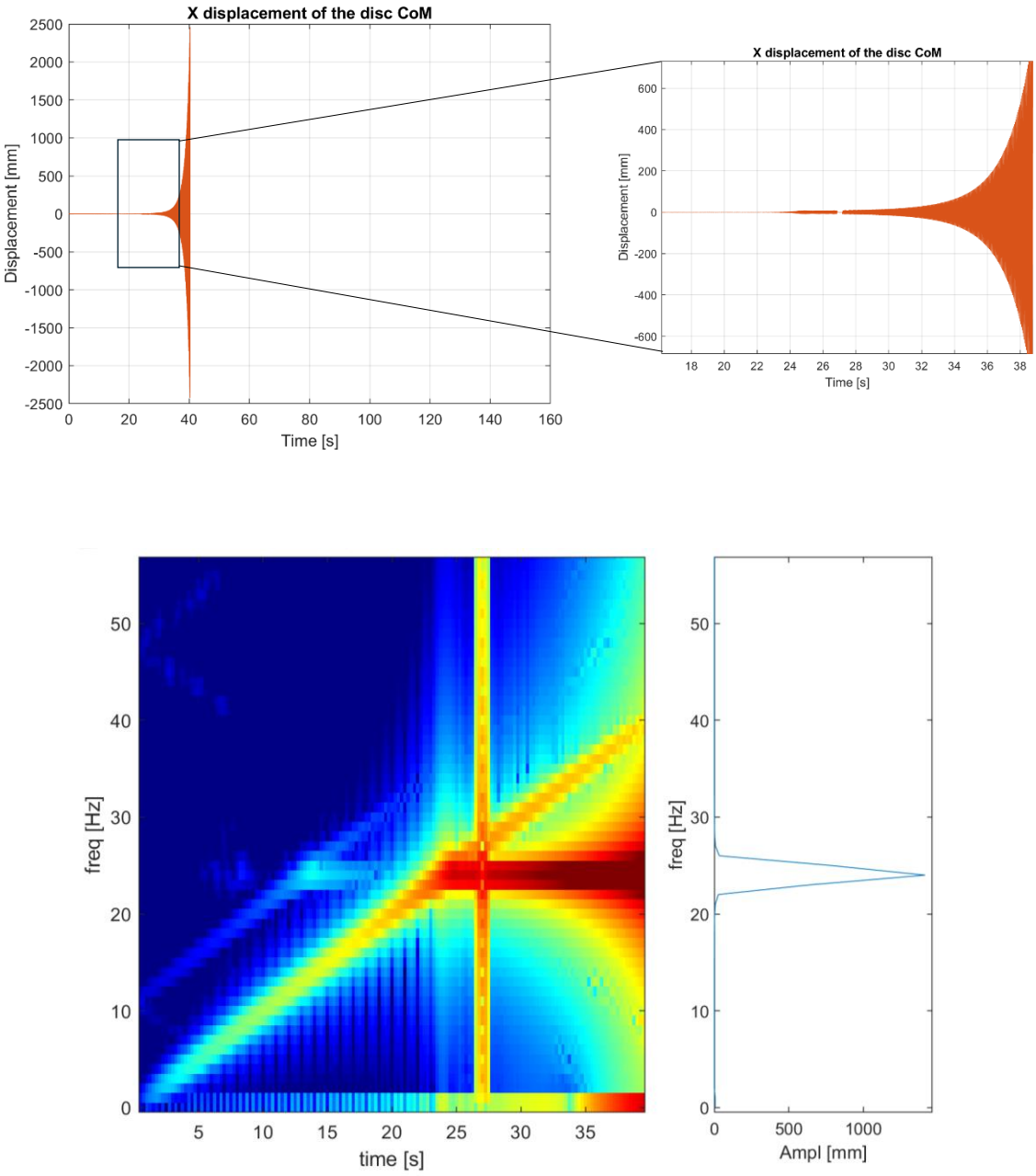


*Figure 49: CoM displacement and its waterfall for Damping Ratio = 10%*

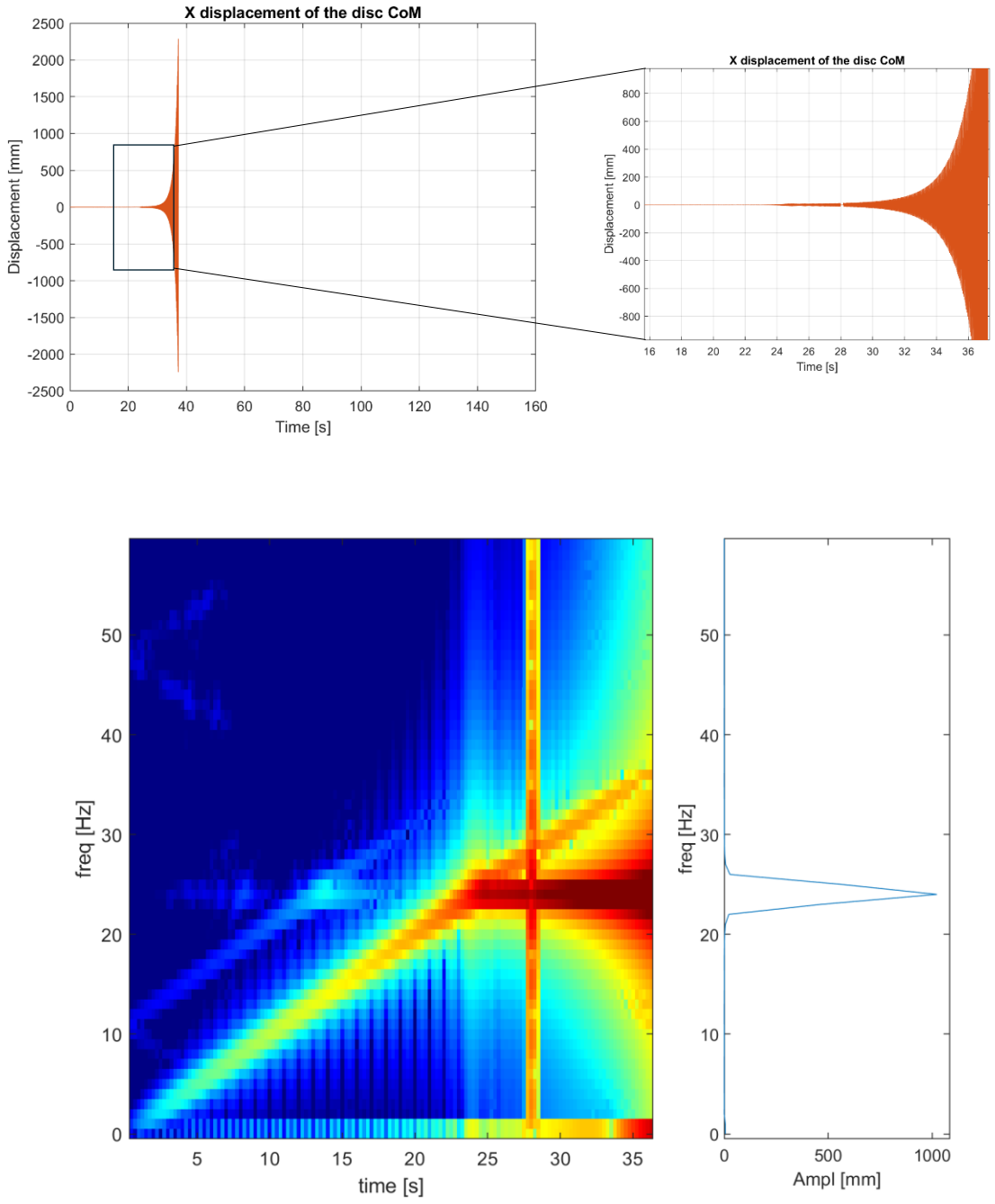


*Figure 50: CoM displacement and its waterfall for Damping Ratio = 15%*

From Figure 47 to Figure 50 the results of simulation ran with damping ratio going from 0% to 15% are shown. Starting from Figure 47 there are two possible

scenarios: the acceleration is high enough to limit the oscillations caused by the crossing of the critical speed or the oscillations increase in magnitude at the crossing causing the shaft displacement to exceed the displacement limit set in the integrator, consequently causing a simulation crash. However, in this case one notes that the absence of damping does not cause the oscillations to diverge to infinite at the crossing with the system's critical speed, this happens also if the speed is kept constant when it reaches its critical value. Furthermore, the system begins to oscillate at its first modal frequency and continues to do so until the end of the simulation (see the signal waterfall in Figure 47). These results are quite difficult to interpret but it should kept in consideration that it represents a completely ideal case since it is obvious that no system could have 0% damping ratio.

By increasing the damping ratio of the rotating component (from Figure 48 to Figure 50) it is possible to notice that an unstable behavior of the system starts to arise. In all the cases above presented, after the rotor spin speed becomes higher than its critical value, oscillations start to increase until the previously mentioned displacement limit is reached, causing simulation crash after few seconds.

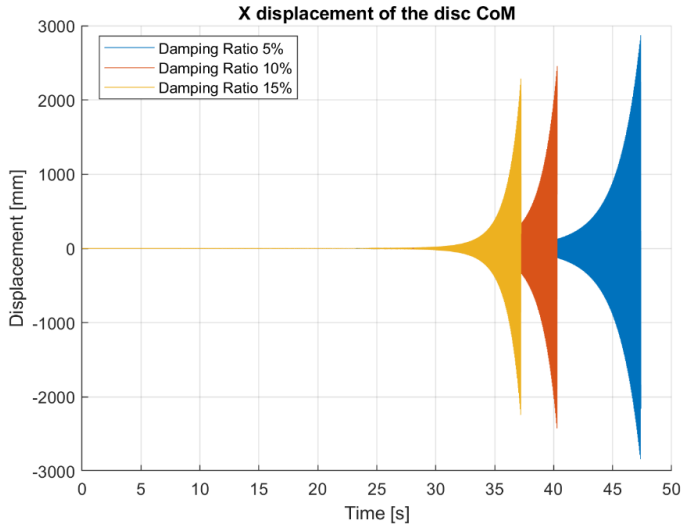


*Figure 51: Transient duration comparison for different damping ratios*

It is evident from Figure 51 how by increasing the damping ratio the simulation crash occurs at lower speeds, indicating a more unstable behavior of the rotor.

A last run has been made by introducing proportional (Rayleigh) damping during the creation of the MNF file. For this purpose, the coefficients alpha and beta were calibrated to achieve the following damping ratio (Figure 52):

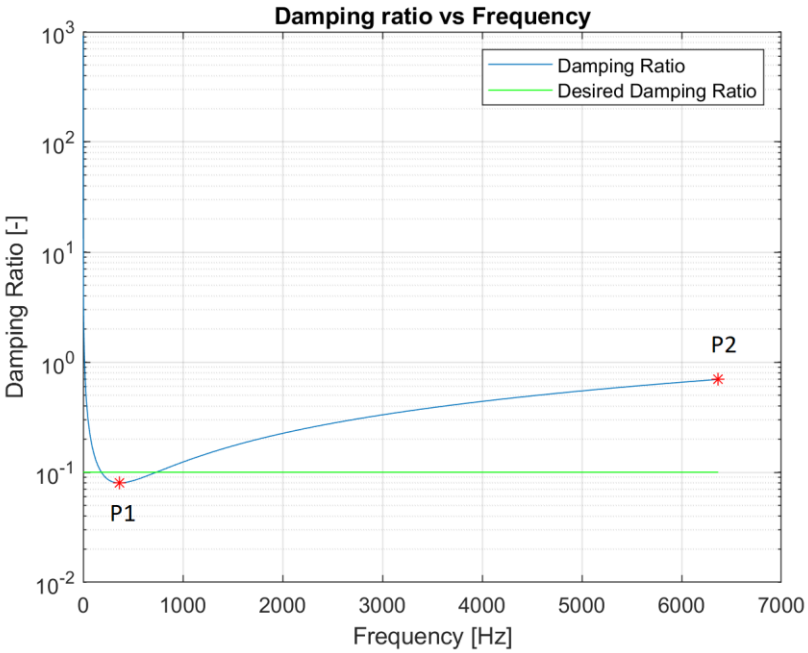


*Figure 52: Damping ratio obtained using alpha and beta Rayleigh parameters*

The target damping value in this case is 10%. The alpha and beta parameters were calibrated to obtain a damping ratio as close as possible to 10% over the frequency range from 100 Hz to 1000 Hz. At points P1 and P2 correspond respectively with damping ratio of values 0.08 and 0.7.

The frequency range was selected based on the frequencies of the first six non-rigid body modes of the unconstrained deformable body alone:

| Mode n° | Frequency [Hz] |
|---|---|
| 1 | 127.10 |
| 2 | 127.10 |
| 3 | 347.67 |
| 4 | 347.67 |
| 5 | 677.63 |
| 6 | 677.63 |

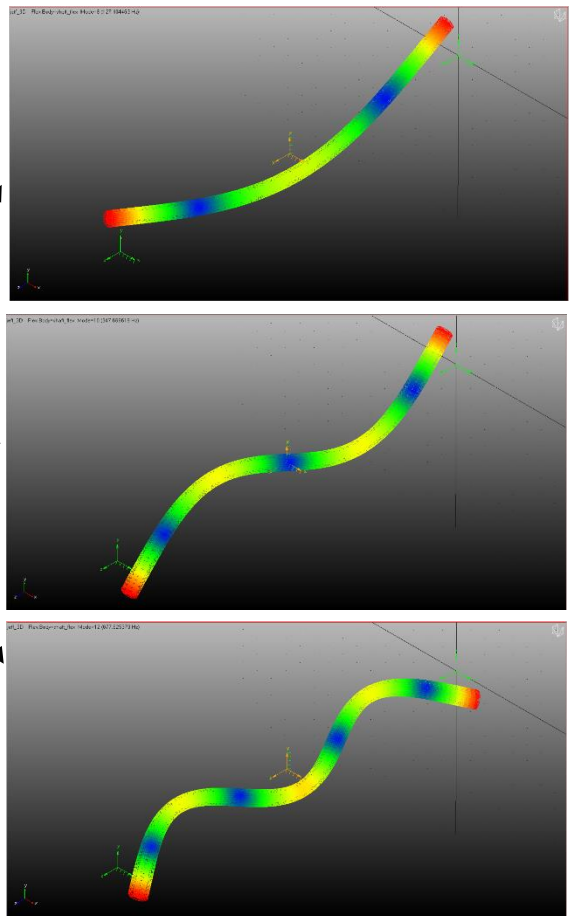

*Figure 53: First three mode shapes and frequencies of the sole flexible body*

The modes associated with the first six natural frequencies shown in Figure 53 were assumed to be the modes giving the highest contribution to the shape of the first mode of the complete system.

The results of the simulation with the damping shown above are as follows:

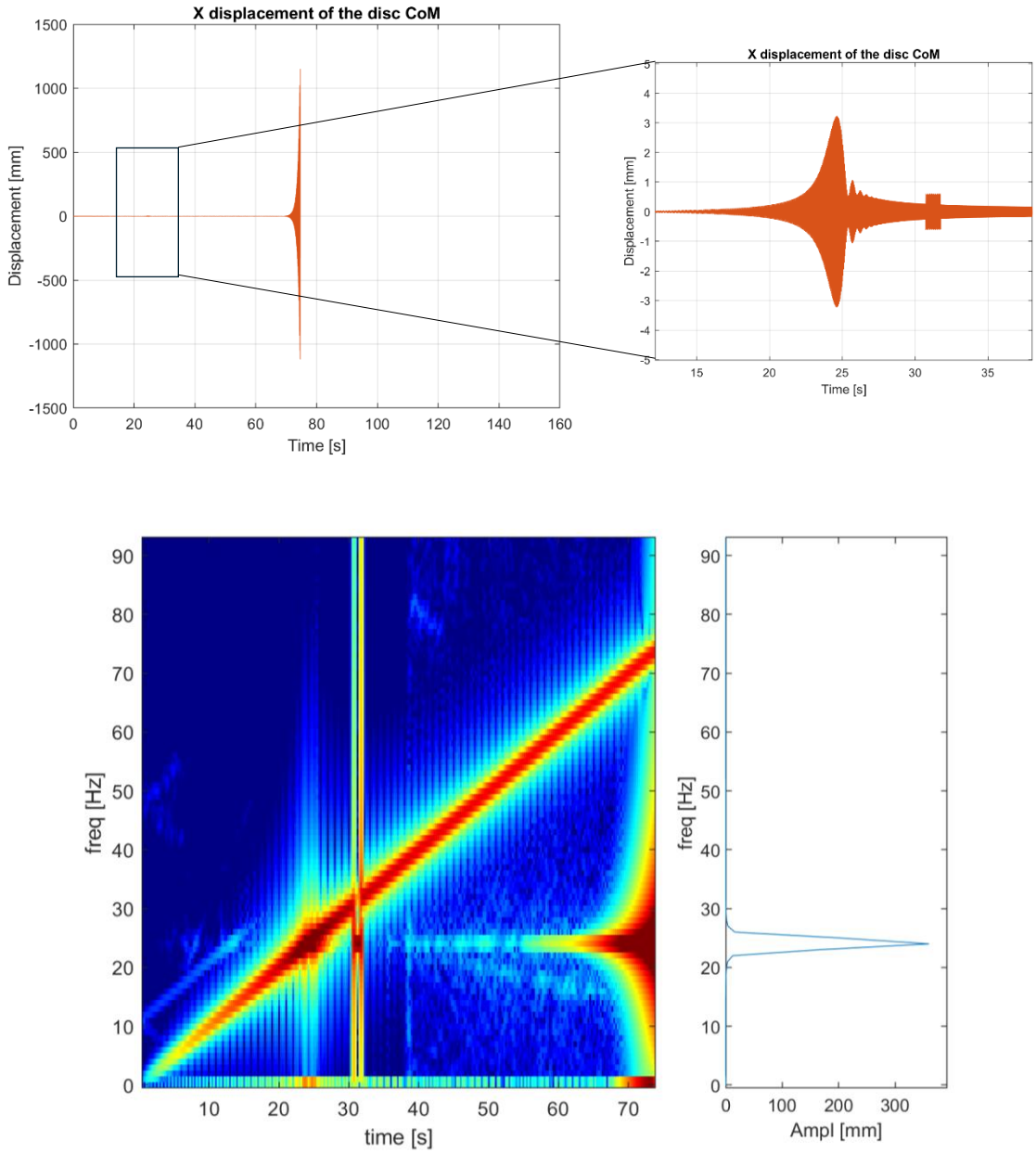


*Figure 54: CoM displacement and its waterfall for proportional damping*

From Figure 54, it is observed that the first mode is traversed at approximately 24 s and that, although oscillations are initially attenuated, as the speed increases the mode resumes its oscillatory motion, diverging toward progressively larger amplitudes until the simulation eventually crashes.

What is noticeable in this case is the different behavior when using the modal damping ratio set after the generation of the MNF and the proportional damping introduced before the generation of the MNF of the flexible shaft. In this case for example, oscillations at the first mode frequency are initially damped, showing a behavior that is quite unexpected from what was highlighted in the previous results.

The reason why the rotor has shown contradictory and unexpected results could be strictly related to the mathematical formulation used during the generation of the MNF. The FE model of the flexible shaft is indeed made of solid 3D elements in which each node has 3DOF which are the three translations in space. To consider rotation related phenomena a rotational velocity should be defined prior to the generation of the MNF, so that gyroscopic matrix, circulatory matrix due to rotating damping, and differential stiffness matrix can be evaluated and considered in the model [15] (as an example of rotor modelled with 3D solid elements see also [17]).

## 3.2. Case 2 (SOL107)

Given the results obtained, it was decided to use the SOL 107 command (Direct complex eigenvalues) to regenerate the MNF file containing the information for the flexible body. By means of this command, after specifying the maximum rotational speed of the rotor [13], it is possible to include in the file the gyroscopic matrix, the circulatory matrix, and the differential stiffness matrix. The effects of these contributions are considered as a modal force (MFORCE, [14]) distributed along the entire length of the rotor and scaled linearly with the rotational speed [15]. This feature has been implemented only starting from version 2024.1 of MSC.Adams.

### 3.2.1. Dynamic simulation

Also in this case, dynamic simulations were carried out with different damping values. The speed profile imposed on the rotor, the step time size, and the total simulation duration were kept unchanged with respect to the previous model. Five simulations were performed using the following damping values for the flexible body:

| Simulation n° | $\zeta$ imposed to flex body | $\zeta$ for first mode of the system |
|---|---|---|
| 1 | 5% | 0.35% |
| 2 | 10% | 0.71% |
| 3 | 15% | 1.07% |
| 4 | 20% | 1.42% |
| 5 | 30% | 2.13% |

Table 5: Damping ratio imposed on the sole flexible body vs damping ratio of the whole system

The values in the central column of Table 5 represent the modal damping ratio values assigned to the flexible body for all its modes. These values have been introduced through the yellow highlighted option in Figure 46.

Whereas the values in the right-hand column correspond to the damping ratio of the first mode of the whole system obtained by performing a modal analysis of the system including the constraints and the disc.

The results are presented in the following figures:

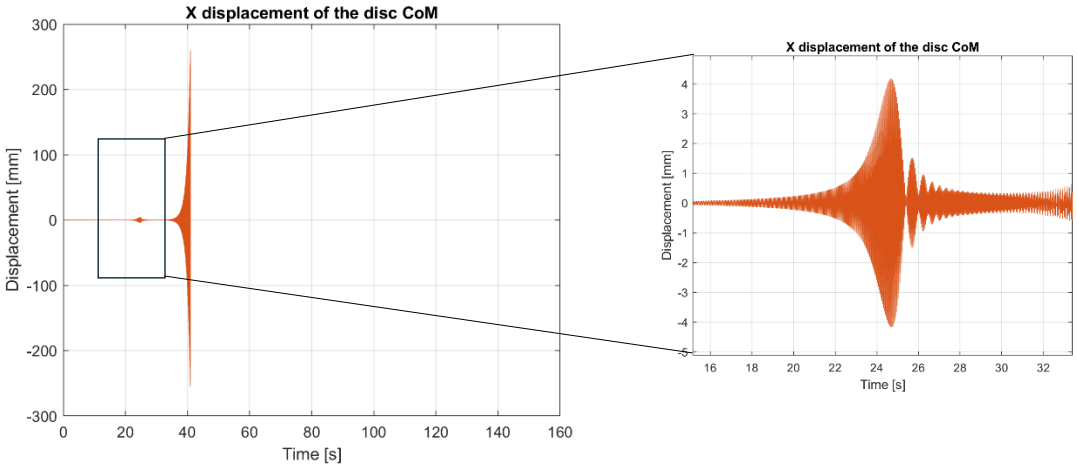


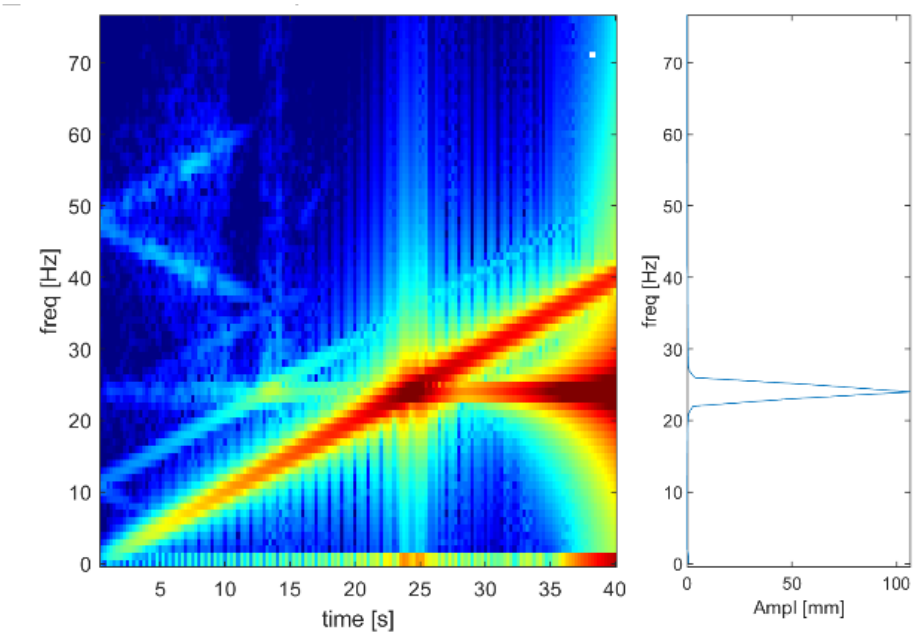


*Figure 55: CoM displacement and its waterfall for Damping Ratio = 5%*

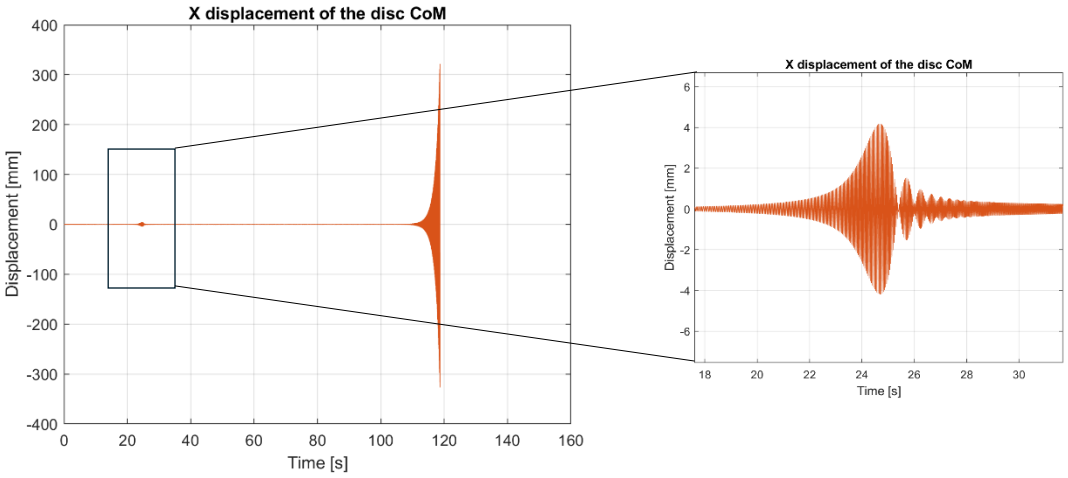


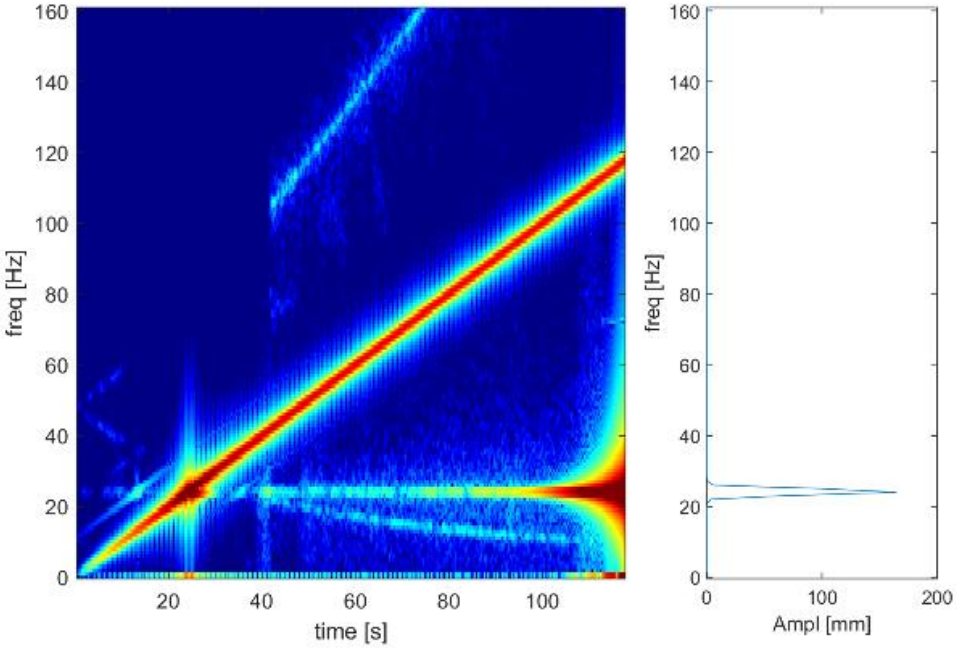


*Figure 56: CoM displacement and its waterfall for Damping Ratio = 10%*

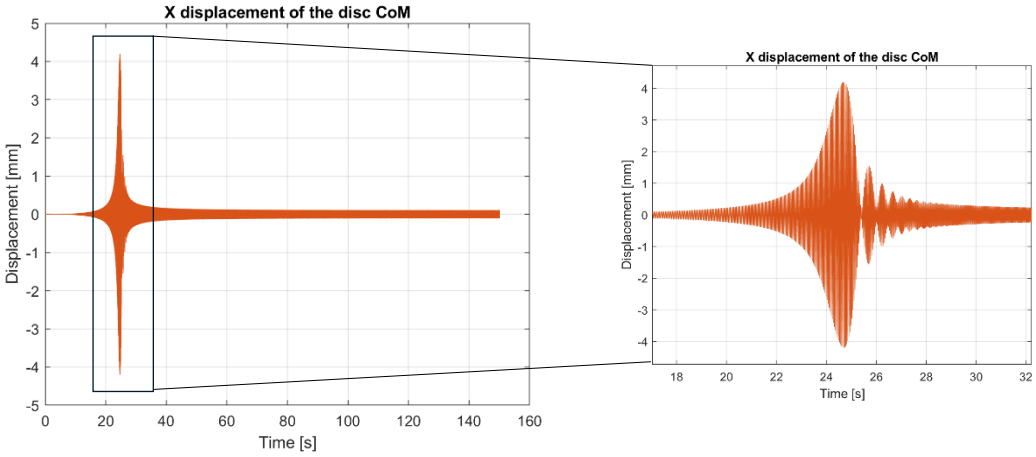


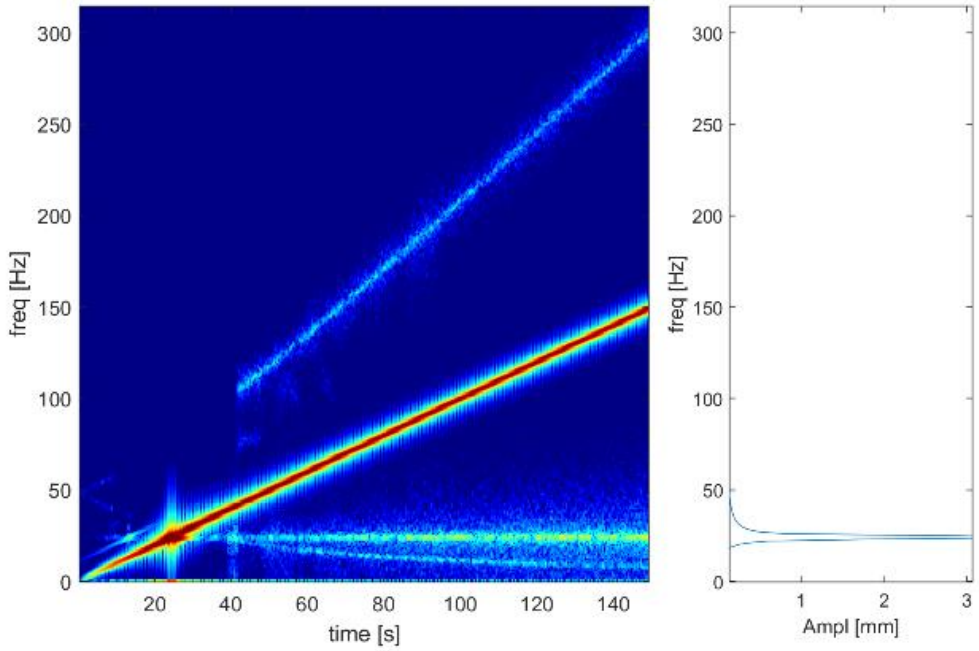


*Figure 57: CoM displacement and its waterfall for Damping Ratio = 15%*

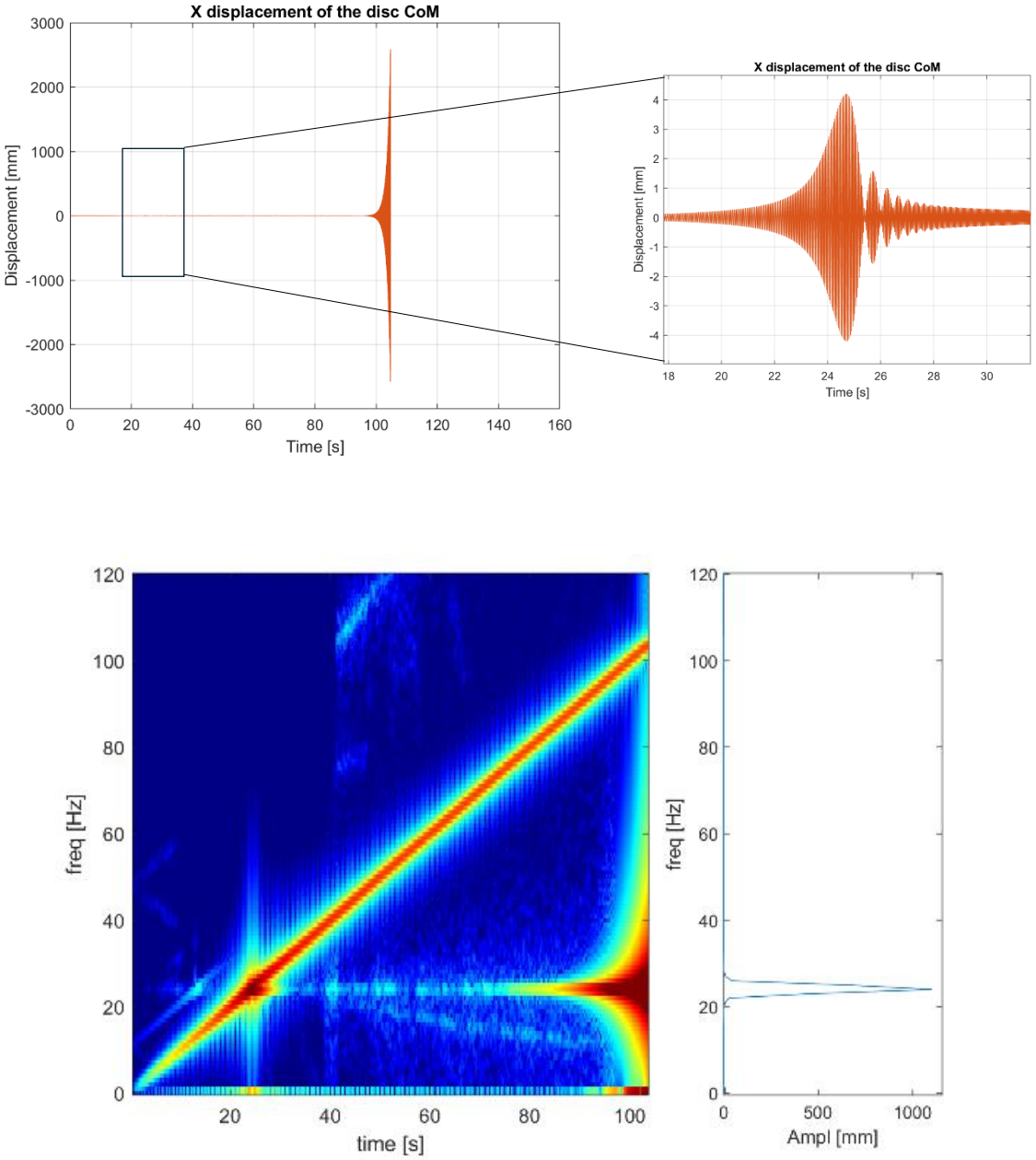


*Figure 58: CoM displacement and its waterfall for Damping Ratio = 20%*

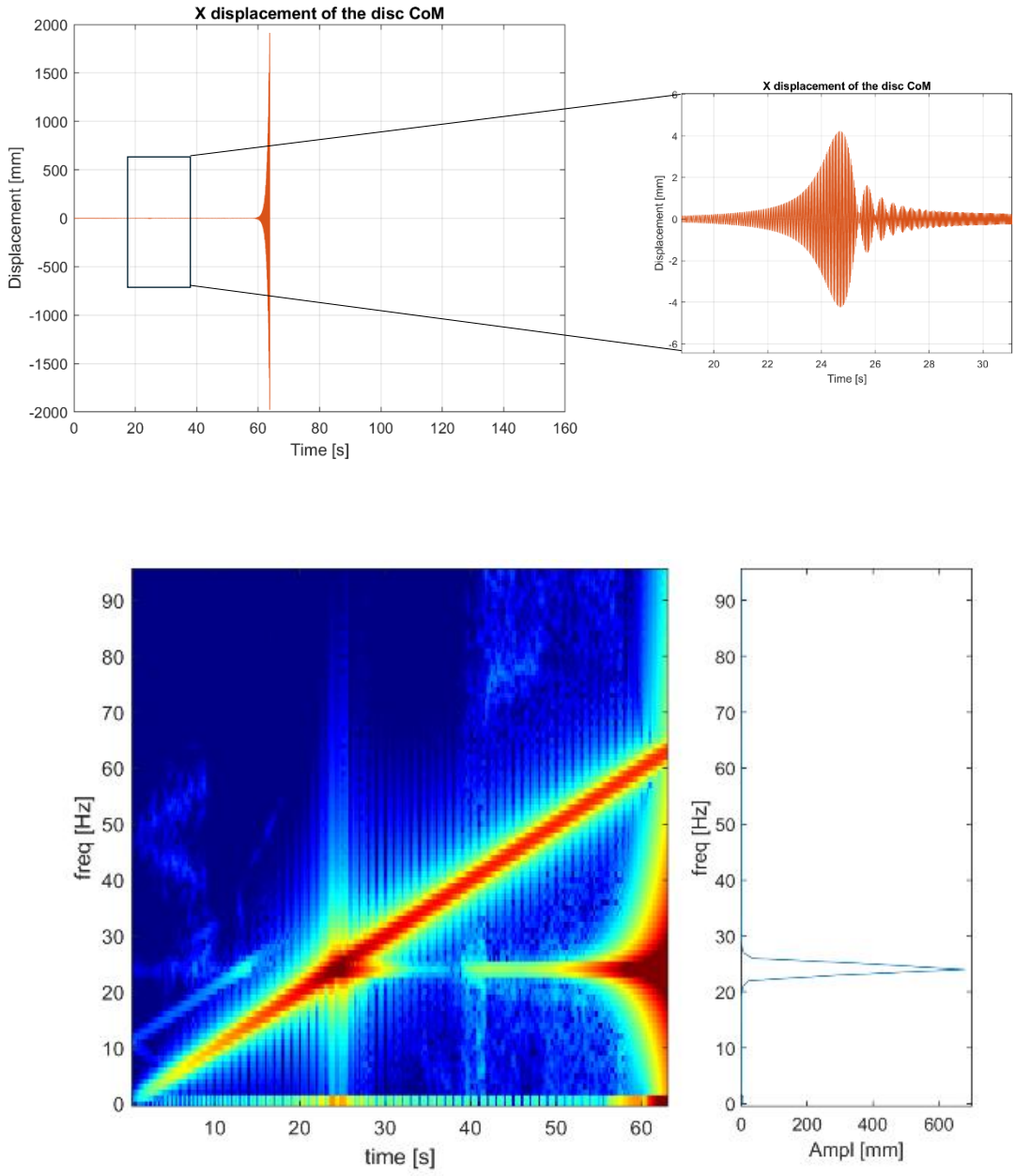


*Figure 59: CoM displacement and its waterfall for Damping Ratio = 30%*

By using the new MNF which should consider rotational speed-related phenomena, the results obtained are quite different from that of Case 1.

From Figure 55 to Figure 59 the damping ratio has been gradually increased as indicated in Table 5. What arises from the results is that for smaller values of damping ratio the initially damped oscillations, after the critical speed crossing,

start to increase in amplitude at supercritical speed showing an unstable behavior, until they eventually cause the simulation crash (in a similar way of what has been seen in Case 1 by adopting proportional damping). As the damping ratio has been increased an increase in the simulation time has been witnessed and for a value equal to 15% the system appears to work in stable conditions until the end of the simulation. However, if the damping ratio is again increased to 20% and 30% the system shows an unstable behavior causing again an increase of the oscillations leading to a simulation crash.

By referring to the Jeffcott rotor model described in [1] none of these results is adherent to what is known from theory. Besides the amplitude of the peak resonance that seems to be independent from the amount of rotating damping that have been introduced in the system, the total absence of non-rotating damping should make the instability field to exist for the whole supercritical speed range, whereas it seems that, at least for the first values of damping ratio, increasing the rotating damping enlarges the system stability field.

It should also be noted that the damping in this case is added after the generation of the MNF, thus after the flexible body is imported into the software. This latter could also be a reason for this counter intuitive behavior of the system, probably due to a not proper integration of the damping matrices with the flexible shaft model.

The study of this model for this thesis project ends here but these results should be studied more in detail, perhaps through a change in the geometry of the system or by adding damping through other methodologies.

# 4. POWER GEARBOX MODEL

With the objective of investigating the capabilities of the Gear AT module in MSC.Adams, a test case was prepared for the power gearbox (PGB) used within a commercial turboprop engine. The unit is a two-stage, spur-gear epicyclic train in star configuration with the carrier fixed to the engine casing.

The test case is particularly compelling because, due to its geometry, the deformability of the components is expected to strongly affect the dynamic behavior of the system. Said component flexibility will be considered by exploiting what has been learned with the previous chapter on integration of flexible bodies in MSC.Adams together with the module Gear AT of the software.

## 4.1. Test case presentation

In this section, the model developed for the test case of interest is presented. For commercial reasons, it was not possible to include the numerical values related to the number and geometry of the gear teeth, nor the dimensions of the drive shafts and the positions of the bearings. Moreover, the plots obtained from the performed simulations are reported either without numerical values or with values normalized to the highest one.

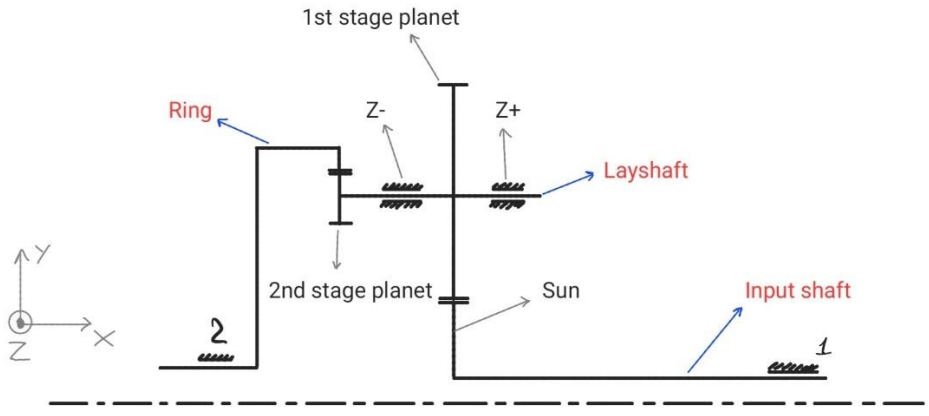


*Figure 60: Gearbox model schematic: side view*

The schematic in Figure 60 represents the actual construction of the gearbox, which consists of:

- *Input shaft*
- *Layshafts*
- *Ring*

The input shaft, flanged to the low-pressure turbine, transmits the rotational motion to the remaining gearbox components via the pinion (*sun*), meshing with the first-stage gears (*large planets*). The latter are mounted on the layshafts together with the second-stage reduction gears (*small planets*), which ultimately mesh with the ring, directly connected to the propeller.

In the configuration shown, the layshafts are supported by bearings that, throughout the document, are referred to as Z−, to identify the bearing located between the first and second stages, and Z+, to identify the bearing on the input-shaft side.

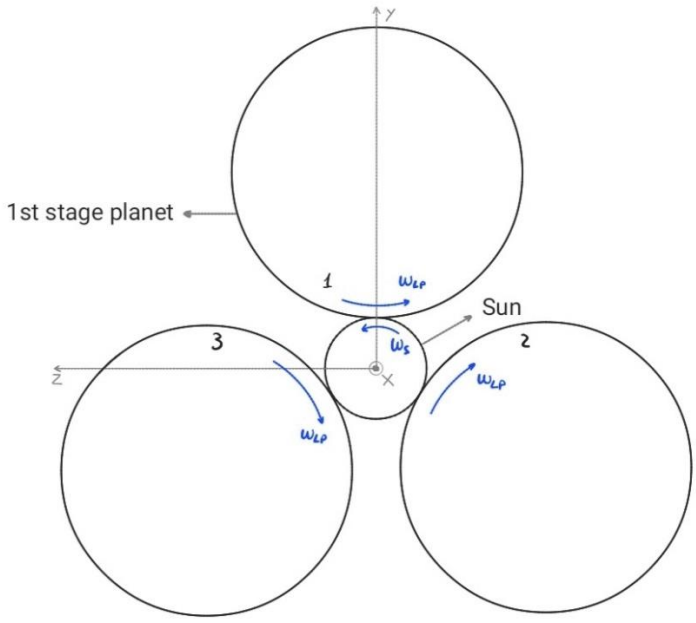


*Figure 61: Gearbox model schematic: first stage*

The schematic in Figure 61 depicts the details of the first reduction stage, comprising the sun and three large planets arranged at angular offsets of from one another. The reduction ratio is therefore given by:

$$i_I = \frac{\omega_S}{\omega_{P1}}$$

where $\omega_S$ is the angular velocity of the sun gear and $\omega_{P1}$ is the angular velocity of the planet gear.

Conversely, in Figure 62 the detail of the second stage is shown, whose reduction ratio is given by the following expression:

$$i_{II} = \frac{\omega_{P2}}{\omega_R}$$

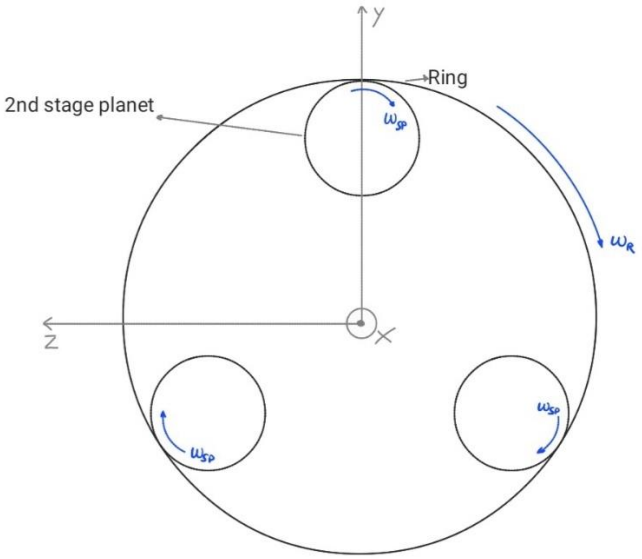


*Figure 62: Gearbox model schematic: second stage*

Where $\omega_{P2}$ is the angular velocity of the planet gear and $\omega_R$ is the angular velocity of the ring gear (and consequently of the propeller). The overall reduction ratio is therefore given by the following:

$$i_{PGB} = i_I \cdot i_{II}$$

### 4.1.1. Model construction

The model was developed in MSC.Adams using the Gear AT module integrated within the software. To progressively increase the system's level of complexity, the model was implemented in four different configurations:

- Rigid bodies – rigid contact – no microgeometry
- Rigid bodies – flexible teeth – no microgeometry
- Rigid bodies – flexible teeth – with microgeometry
- Flexible bodies – flexible teeth – with microgeometry

The main modeling difference arises in the transition from rigid bodies to flexible bodies, which requires invoking the dedicated MSC.Adams/Flex module.

The workflow followed for model development is divided into seven phases:

- Definition of the gear tooth geometry
- Pre-processing of the gear-tooth mesh
- Importing CAD Models (Rigid Bodies)
- Application of constraints
- Creation of *Gear AT Elements*
- Creation of *Gear AT Forces*
- Definition of inputs (speed profile and resisting torque)

When elastic deformations of the drive shafts and wheel bodies are also considered, the import of CAD models is replaced by the *Multi Gear Shaft* option and the subsequent import of Modal Neutral File (MNF).

#### Definition of the gear tooth geometry

In the first phase of model construction, the *Gear AT Advanced Shape Definition* feature was used to define the tooth profile and the corresponding micro-

geometry modifications, as well as to assign the material. For the case under study, the following micro-geometry modifications were applied:

- Tip relief
- Lead crowning

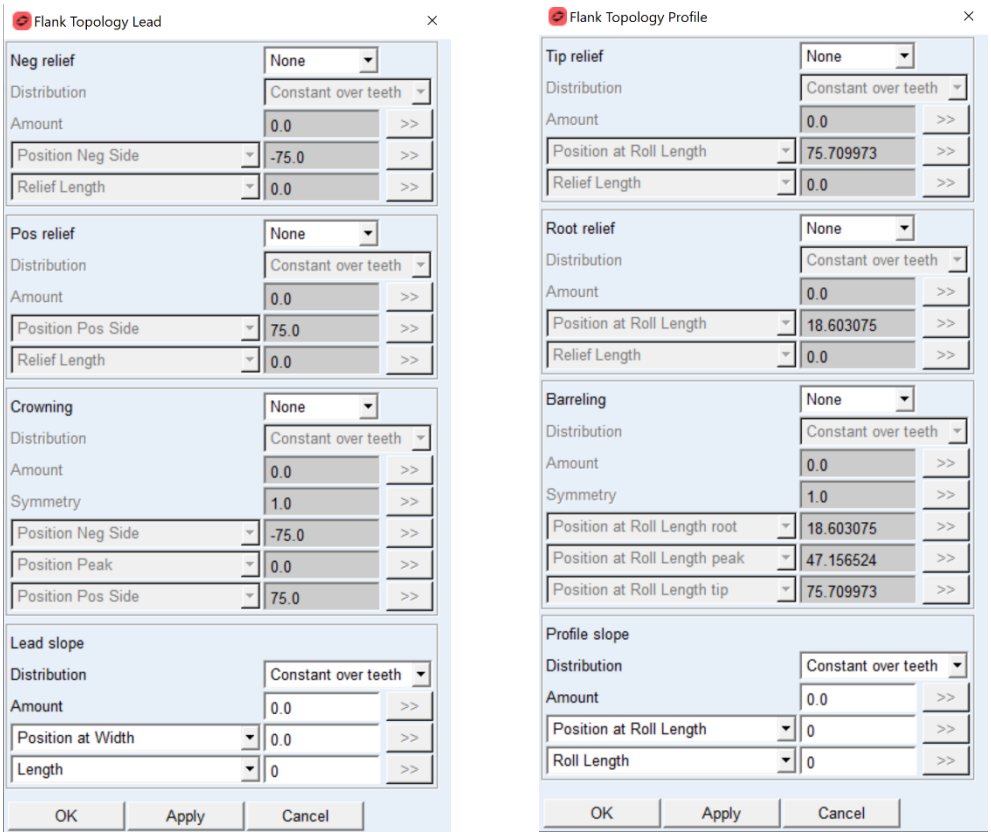


*Figure 63: Lead modification and profile modification (tip and root)*

Figure 63 shows the windows through which it is possible to modify the above-mentioned TPMs, the values present in the text box are default values for MSC.Adams and do not correspond to the actual geometry of the tooth.

In the simulations, TPMs were selectively activated or deactivated as needed in order to better highlight their effects on the results.

### Pre-processing of the gear-tooth mesh

For the case under study, a mesh of moderate density was chosen in order to keep computational times low while, at the same time, avoiding an overly coarse discretization that would fail to adequately capture local effects arising, for example, from a non-uniform pressure distribution on the tooth flank.

Figure 14 in the introduction shows typical Gear AT settings for the mesh generation of the tooth. The settings used for each gear within the model are as follows:

- Mesh density = 2 → 16 elements along the involute profile
- Load element size = 1
- Contact planes = 16

The result is as follows:

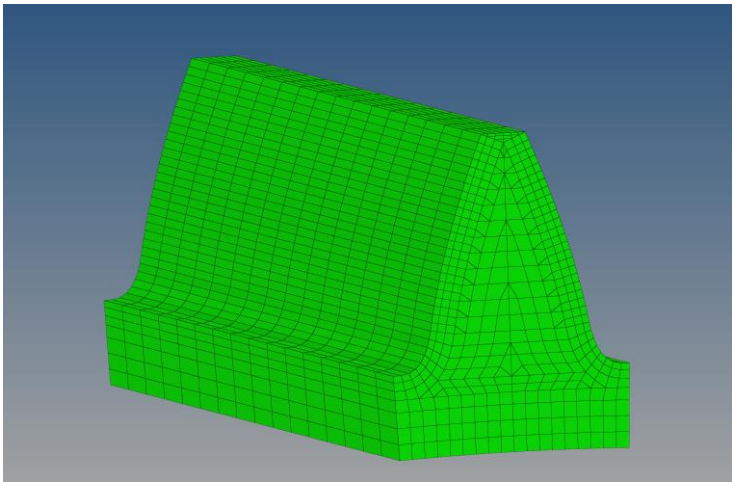

*Figure 64: FE model of a gear tooth resulting from Gear AT Mesh*

The model was developed in two configurations: in one case the drive shafts and the wheel body are treated as ideally rigid bodies; in the other case, the elastic deformations of the bodies under external loading are accounted for. In both cases, however, the option selected for mesh generation is *Flex Tooth* (see Figure 65).

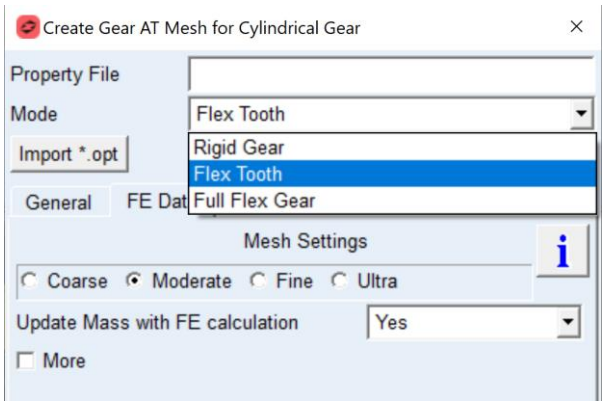


*Figure 65: Modes for Gear AT Mesh*

The reason why the *Full Flex Gear* option was not used in any case is that it is superseded by the *Multi Gear Shaft* option (at least for cylindrical gears).

### Importing CAD Models (Rigid Bodies)

A critical preprocessing step prior to importing the CAD models was the removal of the gear teeth from the original models. The tooth geometry of the meshing gears is generated entirely within Adams, as described in the previous steps (tooth profile and mesh); therefore, the original models must be modified accordingly. It is essential that the teeth be removed starting from the rim diameter, as this value is used by the software as the reference for initiating mesh generation.

Subsequently, for import, it was necessary to adjust the position and orientation of each body so that the mid-face of the gear aligns with the origin of the CAD software's coordinate system.

Finally, the bodies were imported into the Adams environment using the Parasolid format. With respect to the application of constraints, the references for gear positioning, and the potential application of forces and motions, it was necessary to create markers in the Adams environment, which were then strategically placed and assigned to each component of the model.

### Application of Constraints

With the objective of analyzing the motion of the layshafts during a low-speed roll in steady-state condition, bushings elements were selected to represent the Z− and Z+ bearings (see full schematic in Figure 60). These elements allow the specification of constant translational and rotational stiffness and damping values along the three axes X, Y, and Z. In the model described, translational stiffness and damping values were assigned for both bearings in the directions perpendicular to the axis of rotation, whereas only for the Z+ bearing was a (lower) axial translational stiffness (X-axis) introduced.

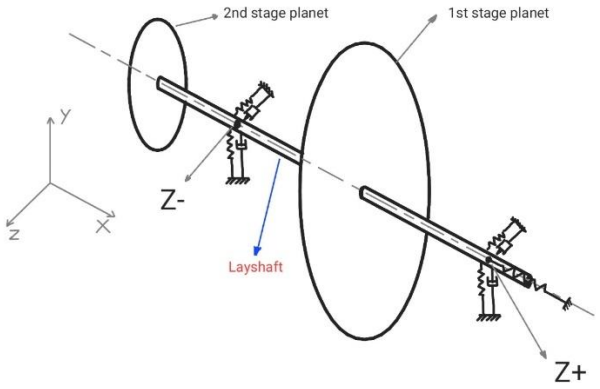


*Figure 66: Layshaft schematic*

In Figure 66 a schematic of the layshaft configuration is presented.

For what concerns instead the input shaft and the ring they have been constrained to the *ground* through infinitely (ideal) rigid constraints that only allow rotation about the x-axis.

### Creation of Gear AT Element(s)

After completing all necessary pre-processing steps for defining the gears and importing the drive shafts, the actual *Gear AT Elements* can be generated. These elements will reference all files created in the preceding phases. Each gear must

be associated with the corresponding *reference marker* belonging to the relevant body. This marker shall be positioned along the shaft's axis of rotation and at the mid-plane of the gear's face width (to be specified under *Ring Gear Reference Marker*, as shown in Figure 67)

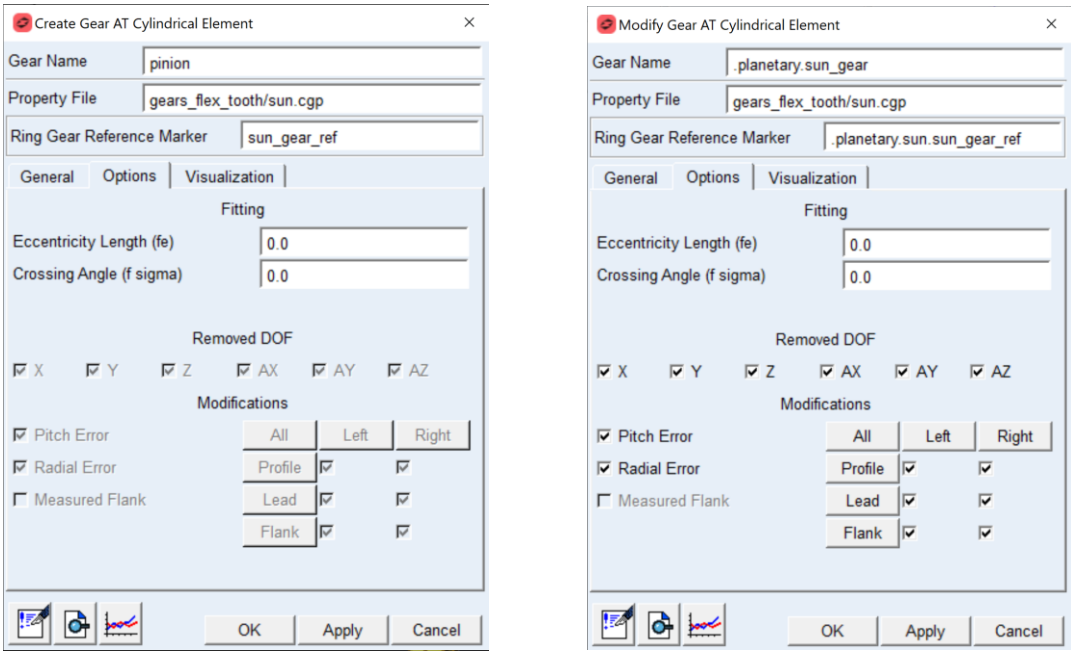


*Figure 67: Create (on the left) and Modify (on the right) Gear AT Element windows*

On the right-hand panel, it is possible to modify certain characteristics of an existing *Gear AT Element*. In particular, one can choose whether to account for the tooth profile's micro-geometry modifications in order to thoroughly assess their influence on the system's behavior. The simulations executed during the development of this thesis have highlighted these effects.

### Creation of GearAT-Forces

This step is required to define the contact between the gears previously created in the Adams environment. In this phase, the gears can be oriented relative to one another to preserve a specified gap between teeth and avoid any element overlapping. The contact model is selected from *Gear-FAST*, *Rigid Contact*, *Flexible Tooth*, and *Full Flex Gear* modes, and the *Contact Overlap* option is

chosen from *Small*, *Normal*, and *High*. For the case under investigation, the effect of tooth deformation on the forces developed at the mesh has been highlighted, specifically how the pressure distribution over the tooth flank varies and how this, in turn, affects the smoothness of the meshing process.

### Definition of Inputs

In the simulations performed, the inputs were not altered to maintain constant external conditions across all four cases. A constant velocity profile was imposed on the input shaft to reproduce typical slow-roll conditions; however, the target velocity was reached gradually by leveraging the STEP function in Adams. A similar approach was adopted for resisting torque profile, which was applied to the ring.

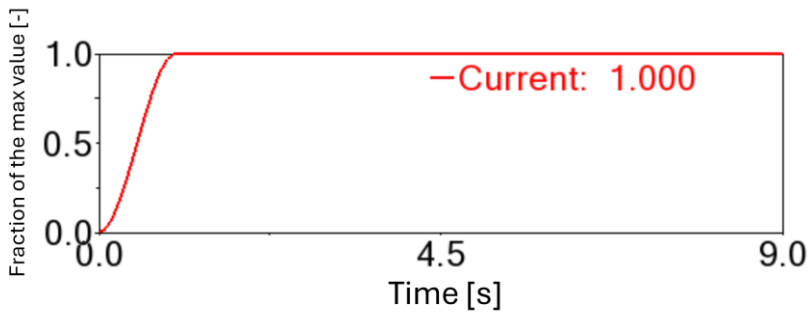


*Figure 68: Imposed angular velocity profile for simulation*

In Figure 68, the abscissa represents the simulation time, while the ordinate shows the normalized value of the imposed torque/velocity. As can be observed, both values start from zero and then reach a (constant) maximum value at $t = 1s$.

**Multi Gear Shaft (MGS)**

The creation of flexible bodies to be introduced into the Adams environment, in this case, is performed via the *Multi Gear Shaft* option, which, by importing a .bdf file (typical of the NASTRAN solver), generates an MNF file that accounts for the mass, stiffness, and damping matrices of the entire body drive shaft and gear rim by leveraging NASTRAN's *GLUED CONTACT* functionality [12].

Analogous to the CAD import workflow, a modification of the bodies' mesh was also performed in this step: specifically, the gear tooth portion was removed, and the underlying mesh was edited so that it could be adjacent to a cylindrical surface with a diameter equal to the *Rim Diameter* defined during the tooth profile creation phase (see Figure 16).

The replacement of the ideally rigid bodies used in the first three simulations was carried out using the *rigid-to-flex* command, which enables substitution of any rigid body within the Adams environment. Through a dedicated interface, each *Attachment Node* of the flexible body is identified and mapped to the nearest markers of any constraints, forces, and/or motions that had previously been assigned to the original rigid body at that location.

To leverage this functionality, the mesh pre-processing performed using the *Flexible Tooth* option must be completed prior to generating the MNF files for the drive shafts, because the property file of each gear is subsequently modified.

## 4.2. Simulation results

As introduced previously, the chosen approach was to increase the model's complexity step by step.

The primary outputs extracted from each simulation are:

- Forces exchanged between the gear teeth

- Displacements of the first and second stage planet gear centers and the sun gear
- Displacements of the *layshafts* at the Z+ and Z− bearings

The following settings were used for all simulations:

- Simulation duration: 9 s
- Integration time step size: 1e-5 s
- Time integrator: HHT (the most suitable for models including Gear AT)

Through the simulations conducted with a progressively higher detail level, the effects of microgeometry modifications and components flexibility on the system quasi-static behavior will be analyzed. By considering the effects given by components flexibility it is expected to witness a sort of orbital motion of the layshafts on the Z-Y plane, as qualitatively shown in Figure 69.

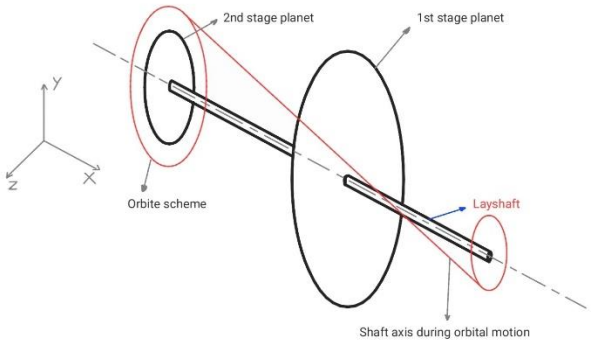


*Figure 69: Schematic of the orbital motion of the layshaft*

### 4.2.1. Rigid Body – Rigid Contact – No microgeometry

For this simulation the following settings have been selected:

- Pre-processing of the tooth mesh → *Flexible Tooth*
- For each *GearAT-Element* → No microgeometry was considered
- Modeling option in *GearAT-Force* → *Rigid Gear*

Regarding the *Rigid Gear* option, the software's default parameters were used for *Contact Stiffness* and *Stiffness Exponent* (Figure 70).

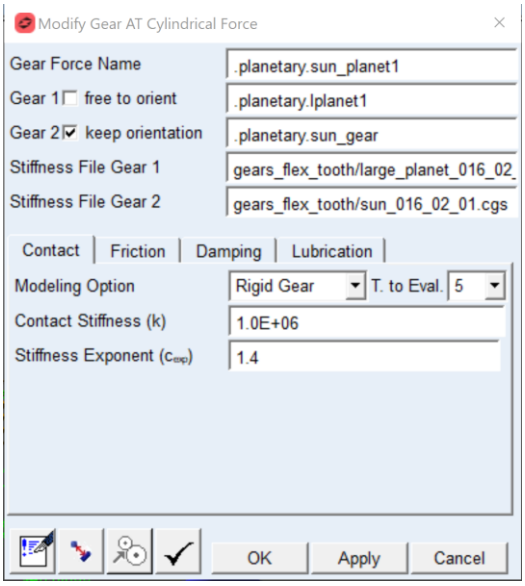


*Figure 70: Selection of the Rigid Gear option in Gear AT Force window*

Furthermore, elastic deformations of the bodies were not considered, since at this stage CAD models imported into Adams were used; consequently, the bodies are treated as rigid in this phase.

### Forces exchanged between the teeth – First stage

The first output is the time history of the forces exchanged between the gear teeth during the simulation. This allows one to determine, at first approximation, whether meshing occurs abruptly or smoothly, to visualize how many teeth are in contact at any given instant of the simulation, and to verify whether the total exchanged force is consistent with the expected (theoretical) value for an equivalent static case.

The results reported refer to only one of the layshafts (denoted as 1 in parentheses hereafter), since the results for the other components are identical due to the system's symmetry.

In this case, the theoretical value serves as the force reference and is computed as follows:

$$F_{tot,th} = \sqrt{{F_{rad,th}}^2 + {F_{tan,th}}^2}$$

where $F_{tan,th} = \frac{C}{r}$ is the tangential force, directly linked to the resistant torque $C$ through the pitch radius $r$, and $F_{rad,th} = \frac{F_{tan,th}}{\cos \alpha}$ is the radial force (with $\alpha$ profile's pressure angle). The subscript *th* indicates a theoretical value.

The data saved during the simulation for the exchanged forces are provided by the software according to the convention discussed in the introduction (in the subsection Adams/Machinery – Gear AT). Accordingly, the quantity hereafter described as the total force exchanged between the teeth is defined as follows:

$$F_{tot} = F_{M2} + F_{M1} + F_0 + F_{P1} + F_{P2} = \sqrt{F_{rad}^2 + F_{tan}^2}$$

In this case, the radial and tangential force components are those obtained directly from the simulation results. The time history of the force exchanged between the sun gear and the first-stage planet gear is as follows:

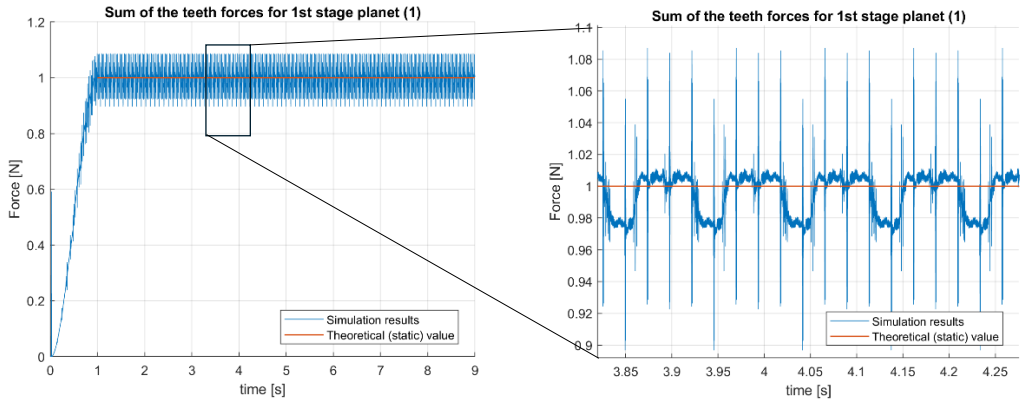


*Figure 71: Total force exchanged at first stage*

Neglecting the transient phase between 0 s and 1 s, during which torque and speed have yet to reach their steady-state values, the plot in Figure 71 shows that meshing occurs rather abruptly; indeed, the total force exchanged between the teeth exhibits pronounced oscillations relative to the theoretical result.

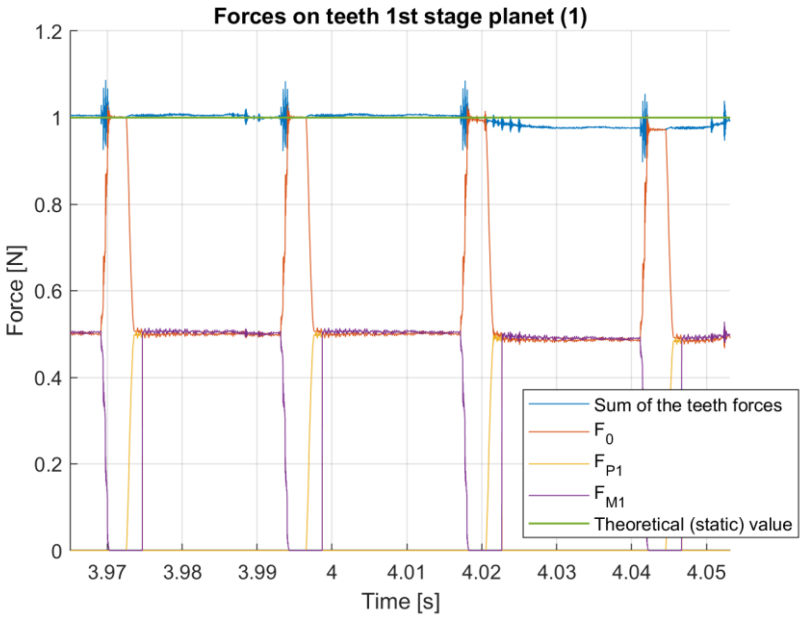


*Figure 72: Total force and single teeth forces exchanged at first stage*

In the plot in Figure 72, a very abrupt meshing behavior is observed. Several force peaks appear shortly before tooth 0 becomes the sole tooth carrying the contact between the two gears.

Owing to the compliant nature of these constraints, the layshafts can displace under the forces exchanged between the two stages. Consequently, the meshing conditions are such that the contact point can no longer be considered concentrated at the mid-width of the gear face.

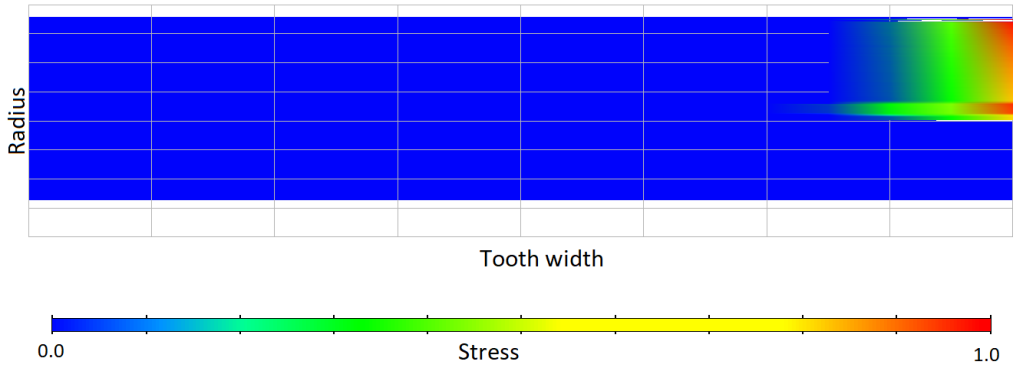


*Figure 73: Pressure distribution on the tooth flank*

As can also be inferred from the result shown here in Figure 73, the layshaft inclination leads to a pressure distribution concentrated at the tooth flank edge (edge contact), which may be the principal reason for the pronounced oscillation relative to the theoretical force value.

Furthermore, performing a waterfall analysis of the aforementioned signal (neglecting the transient segment from 0 s to 1 s) yields the following result:

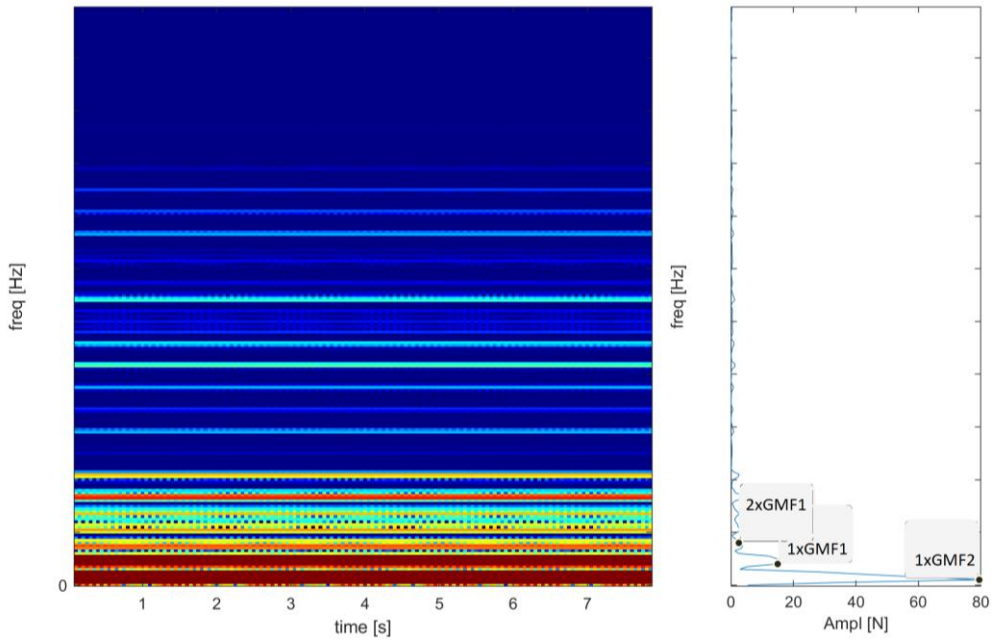


*Figure 74: Waterfall of the total force between meshing teeth*

From the waterfall analysis of Figure 74, the most prominent component in the force signal is the first Gear Meshing Frequency of the second stage (GMF2). Based on this result, it is reasonable to conclude that the influence of the second stage is the primary cause of the force oscillations. The result in (ref) presents the most significant low-frequency components of the force signal (0 Hz–1000 Hz) to better observe the gear meshing frequencies; however, the full spectrum also shows higher-frequency components (of lesser relevance), likely attributable to the abrupt meshing that introduces noise into the force signal.

### Forces exchanged between the teeth – Second stage

For the second stage, similar results are obtained. The total force exchanged between the teeth is as follows (Figure 75):

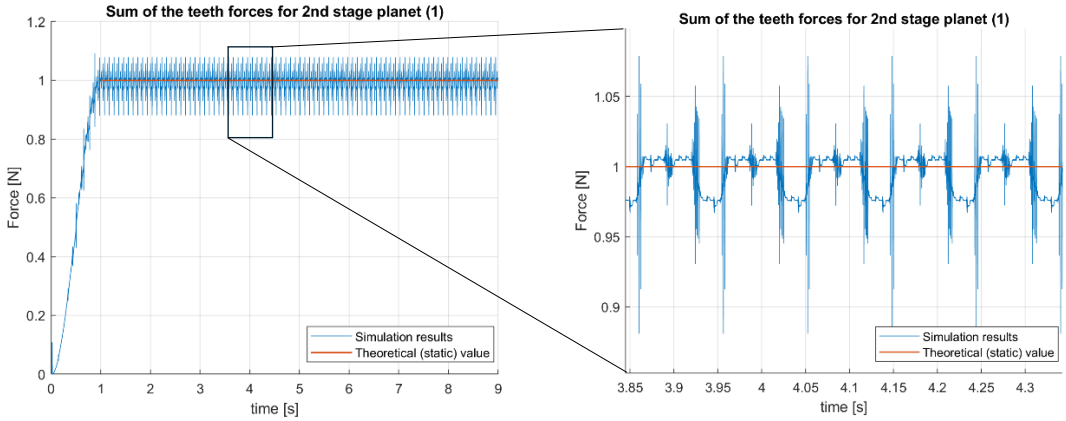


*Figure 75: Total force exchanged at second stage*

By contrast, the per-tooth force values for the second-stage planet differ (Figure 76):

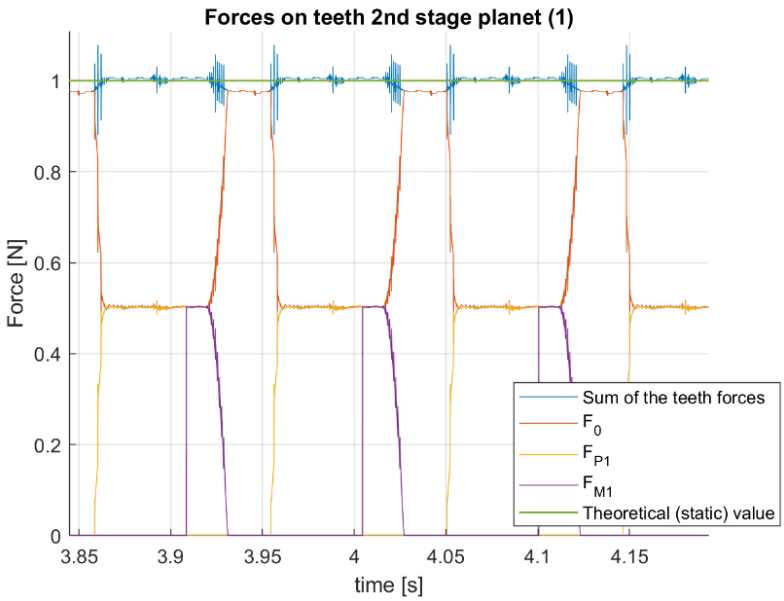


*Figure 76: Total force and single teeth forces exchanged at second stage*

The main difference in this case is due to the different contact ratios of the two gear meshes (first and second stage). Indeed, in this case the intervals during which the contact is carried by a single tooth (tooth 0) are longer.

Here again, the pressure distribution on the tooth flank is concentrated at the edge, resulting in a very abrupt contact:

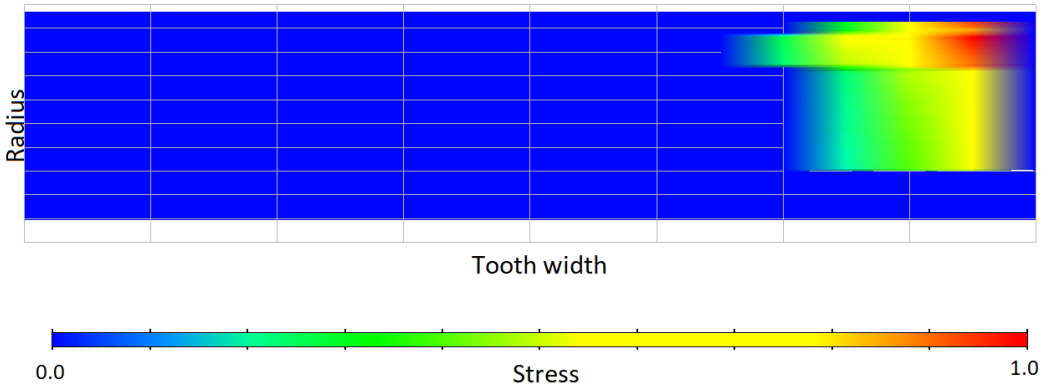


*Figure 77: Pressure distribution on the tooth flank*

As shown in Figure 77, the equivalent point of application of the resultant suggests that the edge contact does not occur on the second-stage planet gear, but rather on the ring gear, which has a smaller face width. Still, the contact pressure is very far from being symmetrical to the face width center.

Performing a waterfall analysis of the force signal, as in the previous case, yields (Figure 78):

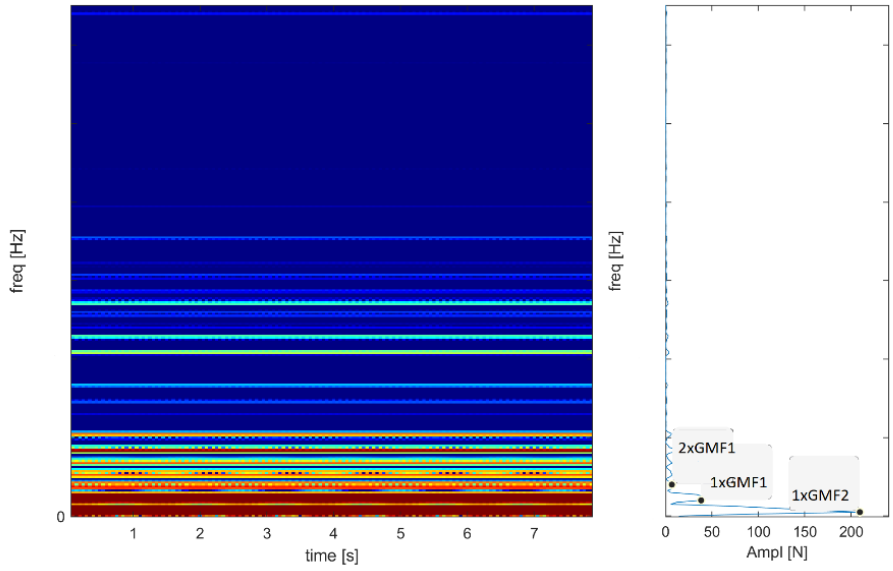


*Figure 78: Waterfall of the total force between meshing teeth*

The frequencies involved are the same as in the previous case, and once again the 1×GMF of the second stage is the most influential component. The observations made earlier regarding high-frequency noise also apply here.

These initial results were obtained using the default settings for the *Rigid Contact* option. Different outcomes could have been achieved by varying the *contact stiffness* and *stiffness exponent* parameters; however, the focus of this activity is to demonstrate the difference in results between a less accurate model (rigid, undeformable tooth) and a more accurate model (deformable tooth, with and without microgeometry).

### Displacements of first and second stage planet gears and sun gear

The displacement results for the first and second stage planet gears and the sun gear are reported here. The objective is to obtain a motion pattern comparable to the internal company reference obtained with proprietary software (i.e., a trajectory resembling a circular orbit).

All results are presented using a scale factor applied to the displacement values to improve visualization.

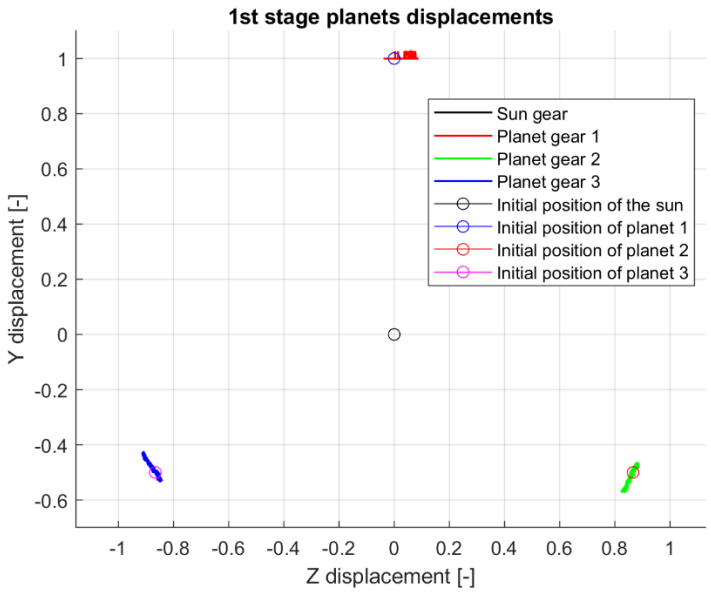


*Figure 79: First stage planet displacements on Z-Y plane*

In the plot of Figure 79, labels 1, 2, and 3 for the planet gears are assigned for clarity, while the red, green, and blue traces denote the displacements of the planet gears relative to their initial positions. As can be seen from the displacements, the expected orbit-like trajectories of the planet gears are not visible in this case. This is primarily due to the neglect of elastic deformations of the bodies, especially that of the input shaft.

A similar behavior is observed for the displacements of the second-stage planet gears and for the bearing displacements (Figure 80):

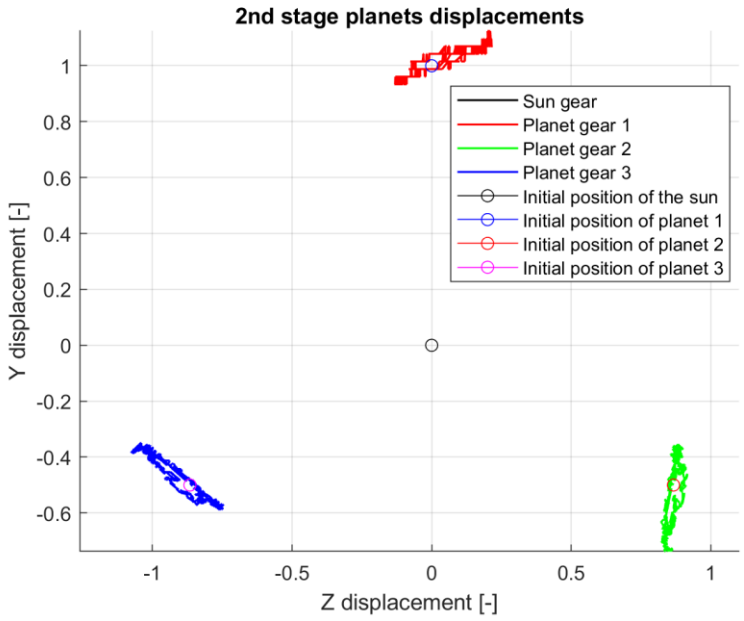


*Figure 80: Second stage planet displacements on Z-Y plane*

The magnitude of the displacements of the second-stage planet gears is much greater than that of the first stage, which is largely attributable to the higher forces exchanged between the teeth.

### Displacements of the layshaft at the Z+ and Z− bearings

Taking the first layshaft as the reference, the time histories of the displacements at the Z− and Z+ bearings are reported in the following plots:

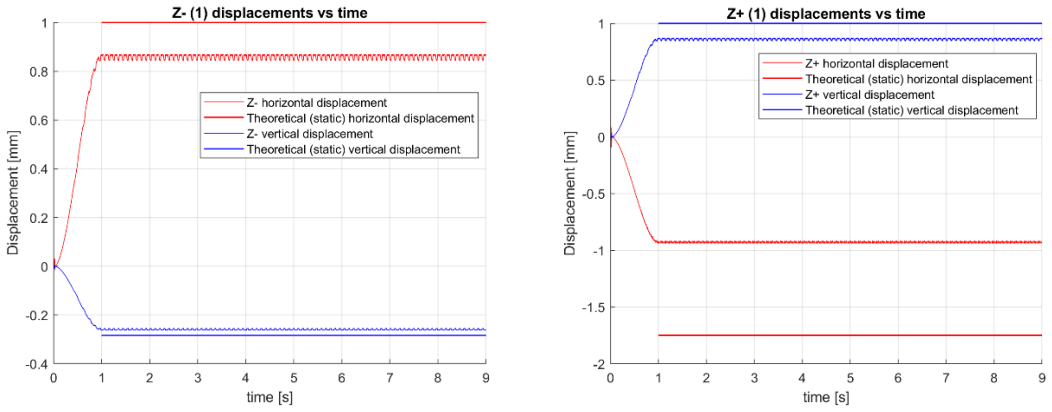


*Figure 81: Bearings displacement over simulation time*

As can be seen from the plots in Figure 81, the displacements obtained during the simulations deviate from theoretical values. The latter were computed by assuming constant forces equal to the total tooth contact force, applied at the mid-width of the gear faces. As will be shown in subsequent results, the discrepancy between the theoretical values and those obtained during the simulation is mainly attributable to the change in the point of application of the force on the tooth.

### 4.2.2. Rigid Body – Flexible tooth – No microgeometry

For this simulation the following settings have been selected:

- Pre-processing of the tooth mesh → *Flexible Tooth*
- For each *GearAT-Element* → No microgeometry was considered
- Modeling option in *GearAT-Force* → *Flexible Tooth*

In this case, the only adjustable contact setting is *Contact Overlap*, which was kept at *Normal* for all simulations.

**Forces exchanged between the teeth – First stage**

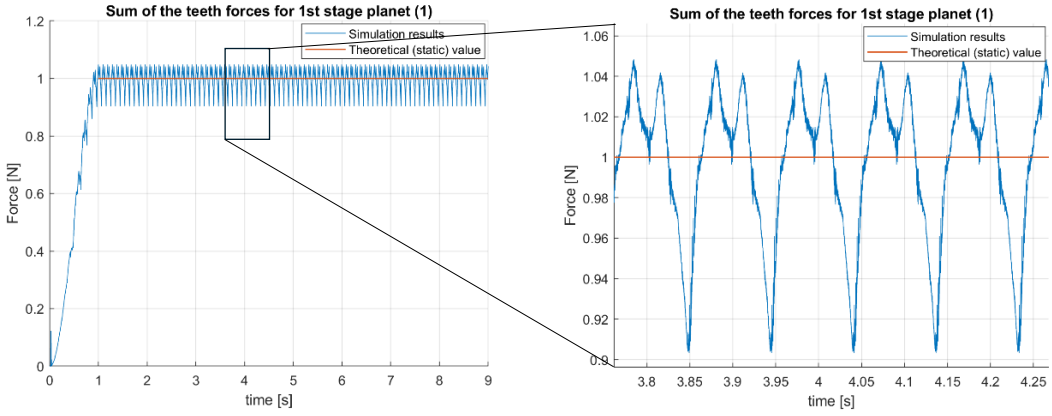


*Figure 82: Total force exchanged at first stage*

In Figure 82, it can be observed that accounting for tooth deformability yields a force history that, while still far from free of oscillations relative to the theoretical value, exhibits fewer force spikes associated with the sudden tooth engagement observed in the previous case.

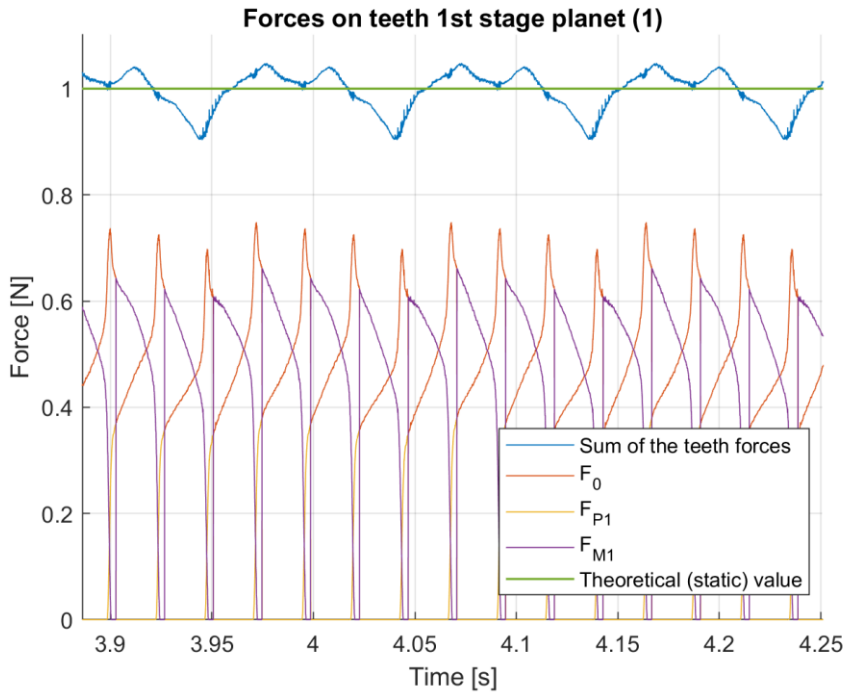


*Figure 83: Total force and single teeth forces exchanged at first stage*

Examining the per-tooth force contributions from Figure 83, it is apparent that, due to the inclination of the first-stage planet gear relative to the sun gear, there is no instant during meshing at which the contact is entirely carried by a single tooth (a condition that would typically occur in a gear with a contact ratio between 1 and 2). Rather, at every instant the contact is sustained by at least two teeth simultaneously, which is quite unexpected for meshing between spur gears. This effect is probably due to the inclination that the layshafts undergo due to the external loads coming from the contact forces of input shaft and ring.

Moreover, compared with the previous case, each tooth engages more gradually over the course of the simulation.

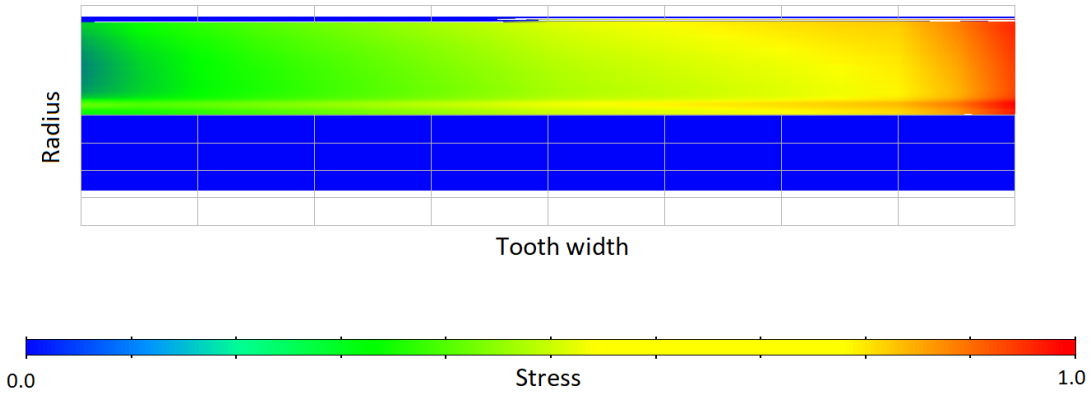


*Figure 84: Pressure distribution on the tooth flank*

As can be seen from the pressure distribution on the tooth flank in Figure 84, accounting for tooth deformability has shifted the resultant force application point closer to the face mid-width; although it remains significantly biased toward the edge, the system is progressively moving away from the pure edge contact observed previously.

Performing a waterfall analysis of the total force exchanged between the gears of the first stage yields the following result:

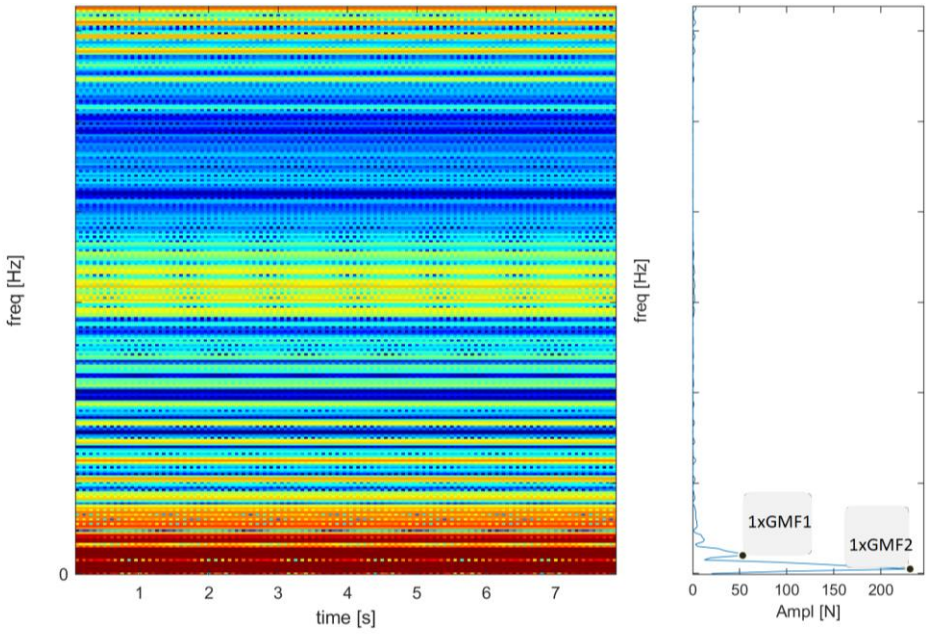


*Figure 85: Waterfall of the total force between meshing teeth*

From the waterfall plot of Figure 85, the same findings as in the previous case can be inferred, except for the near-total absence of significant high-frequency contributions (not visible here), a result that is also reflected in the increased regularity of the time-domain force curve.

### Forces exchanged between the teeth – Second stage

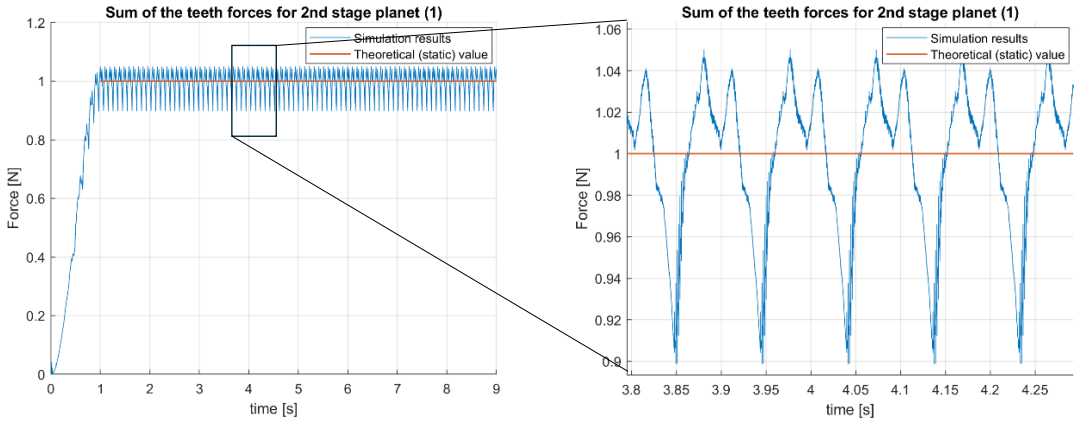


*Figure 86: Total force exchanged at second stage*

As shown in Figure 86, the observed trend is very similar to that of the first stage.

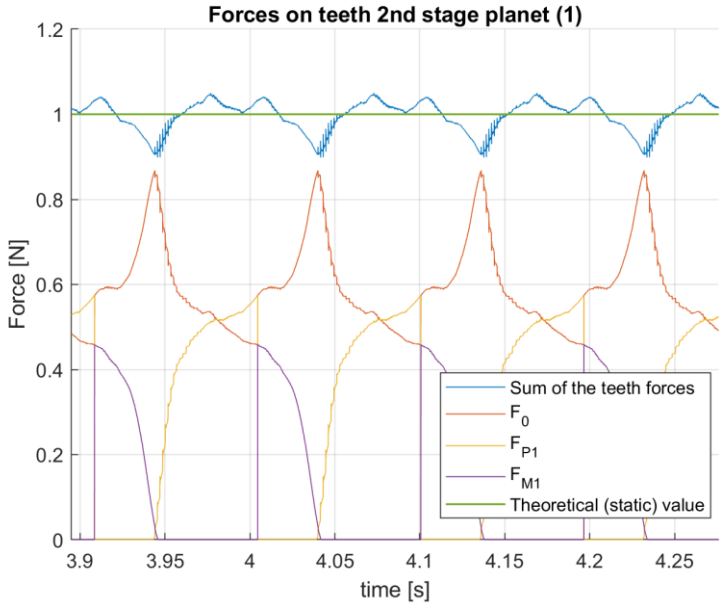


*Figure 87: Total force and single teeth forces exchanged at second stage*

In Figure 87 as well, it can be concluded that during contact the force exchanged between the gears is never borne by a single tooth at any instant; rather, it is always supported by at least two teeth. For the second stage too, the contact is more gradual compared with the *Rigid Contact* case.

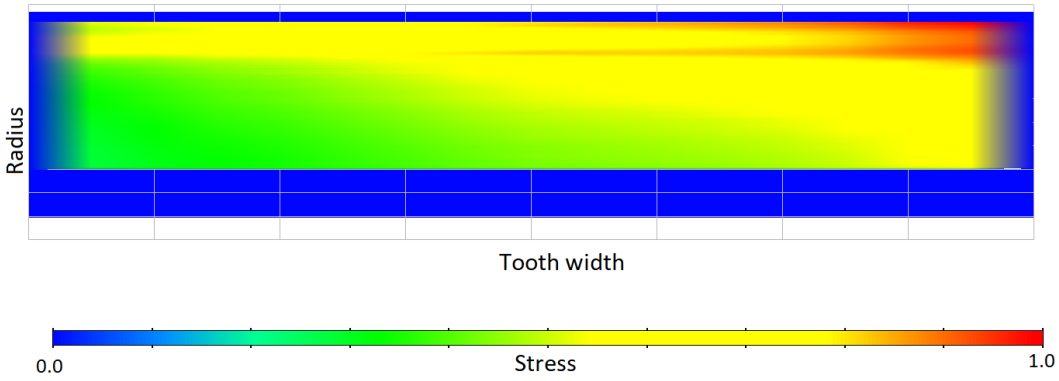


*Figure 88: Pressure distribution on the tooth flank*

Once again, it is evident from Figure 88 that the overall effect of accounting for tooth deformation is a better distribution of the contact pressure over the entire tooth flank, as if one tooth flank, bending under the action of external forces, were conforming to the flank of the mating tooth.

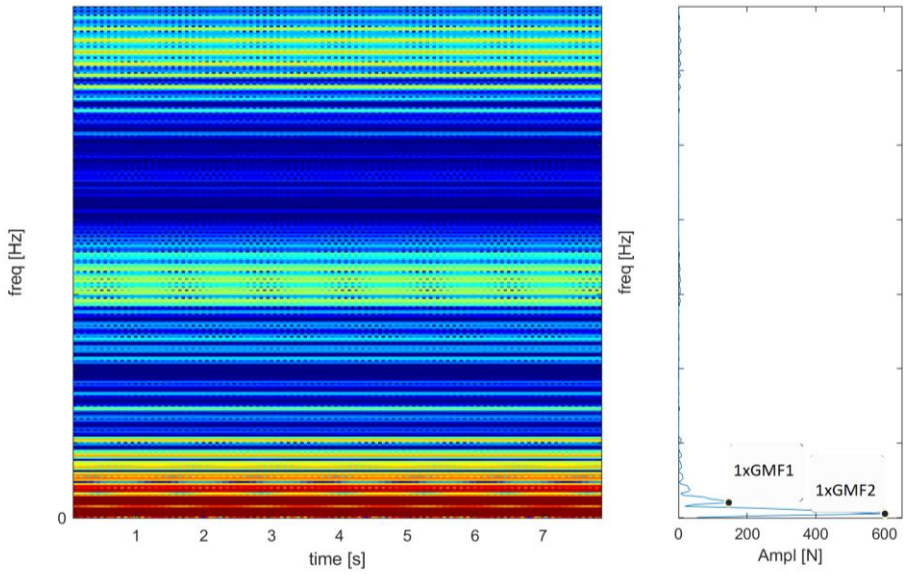


*Figure 89: Waterfall of the total force between meshing teeth*

If a waterfall analysis is performed (Figure 89) on the force signal exchanged between the gears of the second stage, the principal component of the signal is, once again, the second-stage gear mesh frequency (1×GMF2).

### Displacements of first and second stage planet gears and sun gear

The Z–Y plane motion patterns of the first- and second-stage planet gears are reported again to verify the presence of their orbital motion.

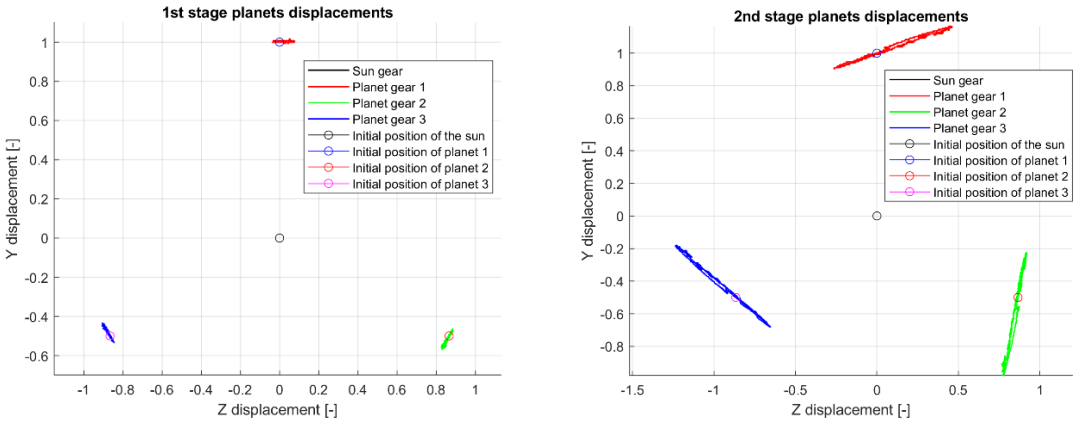


*Figure 90: First and second stage planet displacements on Z-Y plane*

In this case as well, no orbital trajectories are evident (Figure 90). Note that the displacement of the sun gear is scarcely visible compared with the planets, owing to its comparatively small magnitude; this is because the deformations of the input shaft have been neglected.

**Displacements of the layshaft at the Z+ and Z− bearings**

The displacements at the Z+ and Z− bearings for layshaft one are reported here in Figure 91:

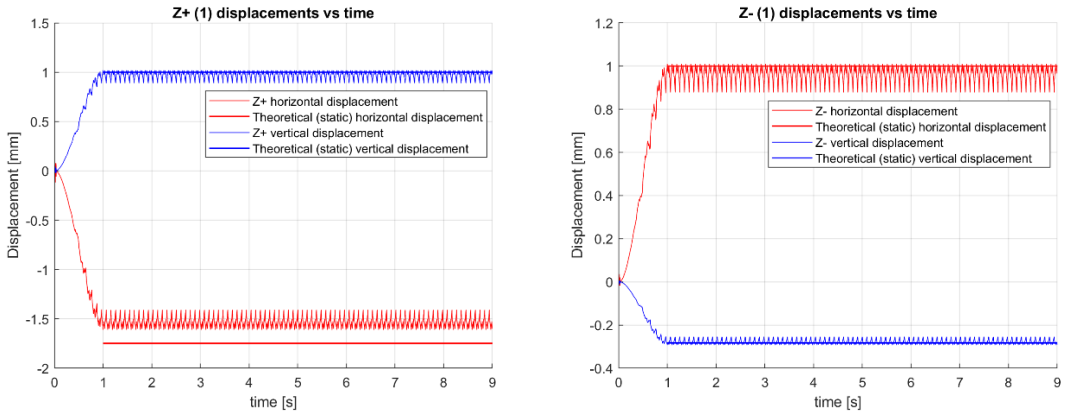


*Figure 91: Bearings displacement over simulation time*

Although the bearing displacements exhibit a distinctly oscillatory behavior relative to their theoretical values, it is evident that the results now align more closely with the theory. This is likely due to the more centered distribution of contact pressure over the tooth flank, which shifts the point of application of the resultant force toward the face mid-width (i.e., closer to the theoretical case).

### 4.2.3. Rigid Body – Flexible tooth – With microgeometry

For this simulation the following settings have been selected:

- Pre-processing of the tooth mesh → *Flexible Tooth*
- For each *GearAT-Element* → Microgeometry is considered
- Modeling option in *GearAT-Force* → *Flexible Tooth*

The main difference compared with the previous case is the inclusion of profile micro-geometry modifications which, as explained earlier, consist of tip relief, intended to achieve smoother contact as a tooth enters or exits engagement (near

the tip of the profile), and lead crowning, the latter being of particular interest for improving the distribution of contact pressure across the tooth flank.

### Forces exchanged between the teeth – First stage

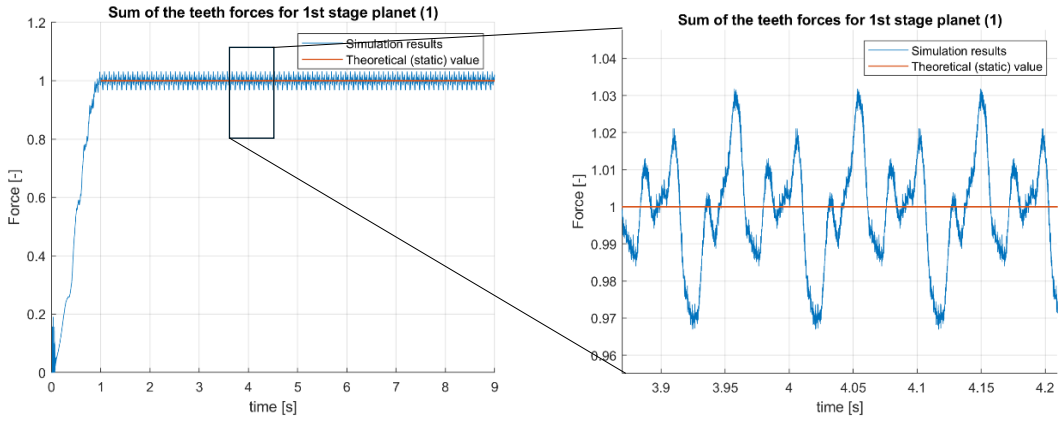


*Figure 92: Total force exchanged at first stage*

As can be seen from the plot of Figure 92, in this case the oscillations of the mesh force between the first-stage gears are visibly reduced compared with the previous cases. This inevitably leads to a marked reduction in transmission error (see [5]). The maximum discrepancy between the theoretical value and the value obtained from the simulation is approximately 3%, still rather significant, but attributable to a simulation in which the deformability of the other gearbox components was not considered.

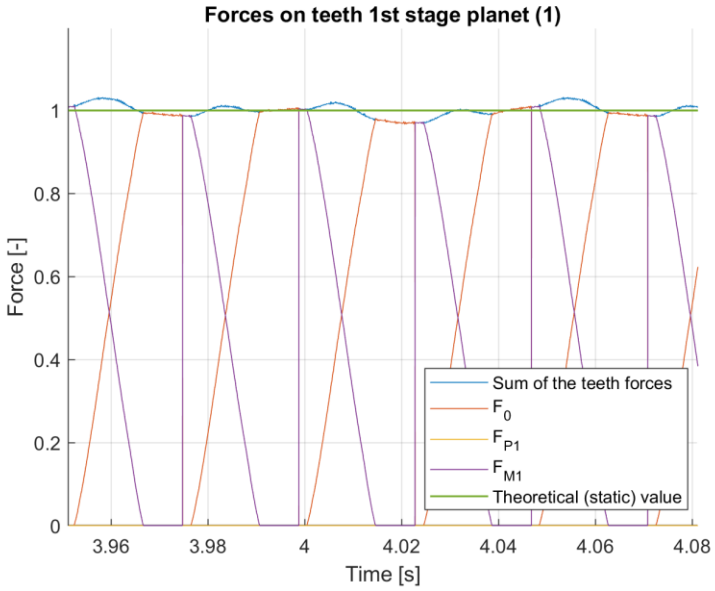


*Figure 93: Total force and single teeth forces exchanged at first stage*

The result shown in Figure 93 demonstrates that the contact is markedly more uniform and gradual than in the previous cases. Note that the sudden decrease of the orange curve together with the abrupt increase of the purple curve are attributable to the tooth numbering assigned by the software to the gears in contact. At that point, tooth 0 becomes tooth M1; consequently, the former tooth P1 becomes the new tooth 0, which shortly after the renumbering begins to enter into contact.

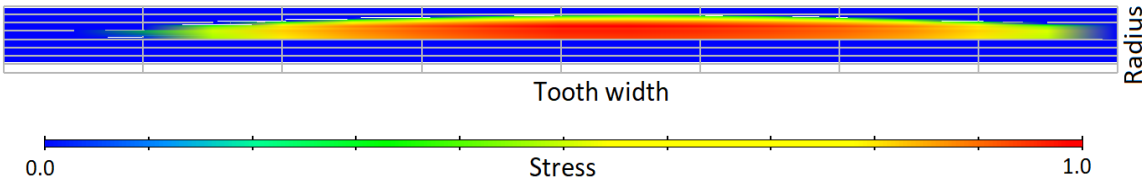


*Figure 94: Pressure distribution on the tooth flank*

As observed from the pressure distribution on the tooth flank in Figure 94, the overall effect of the micro-geometry has been to center the point of application of the force with respect to the face mid-width, which is fundamental to achieving a more gradual meshing of the two gears.

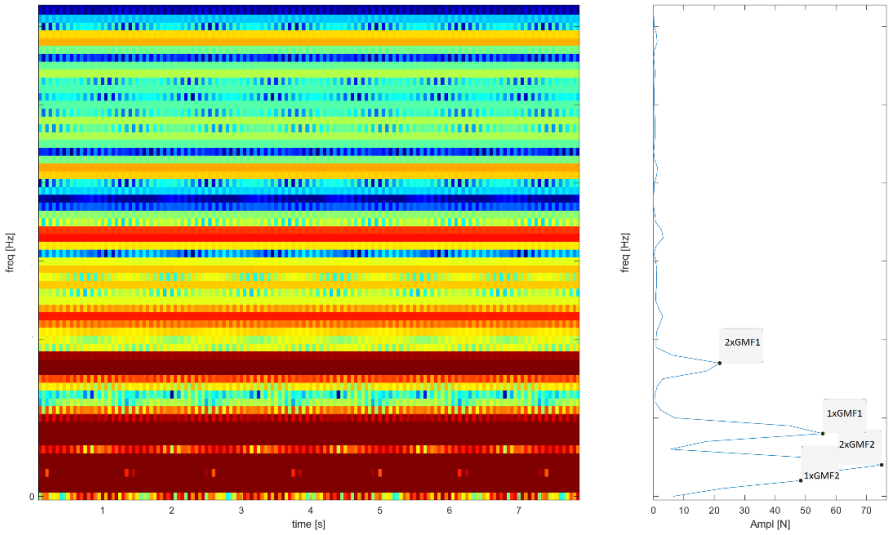


*Figure 95: Waterfall of the total force between meshing teeth*

The main difference relative to the two previous cases is the greater influence of GMF1 on the force signal, which can be seen from the waterfall plot of Figure 95.

## Forces exchanged between the teeth – Second stage

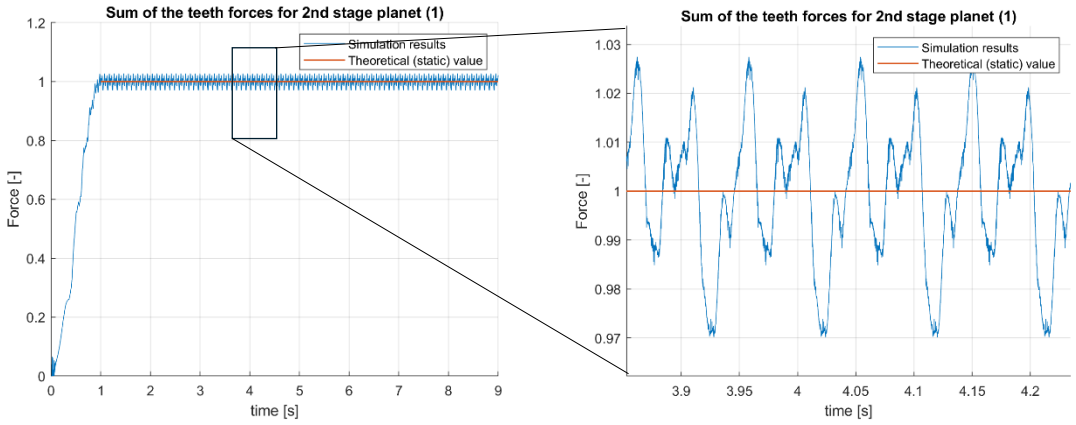


*Figure 96: Total force exchanged at second stage*

The time history of the total force exchanged between the gears of the second stage does not exhibit any differences compared with the first stage.

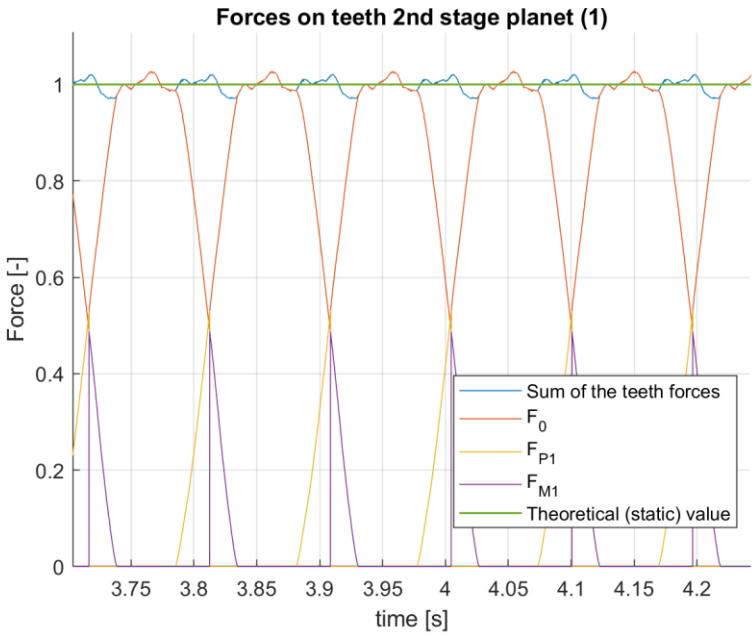


*Figure 97: Total force and single teeth forces exchanged at second stage*

In this case as well, a more gradual gear engagement is observed; thus, it is reasonable to expect that the micro-geometry likewise contributed to achieving a more centered distribution of contact pressure on the tooth flank.

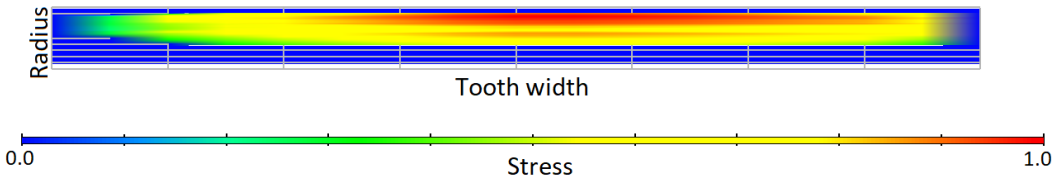


*Figure 98: Pressure distribution on the tooth flank*

If a waterfall analysis is performed on the force signal, the following result is obtained:

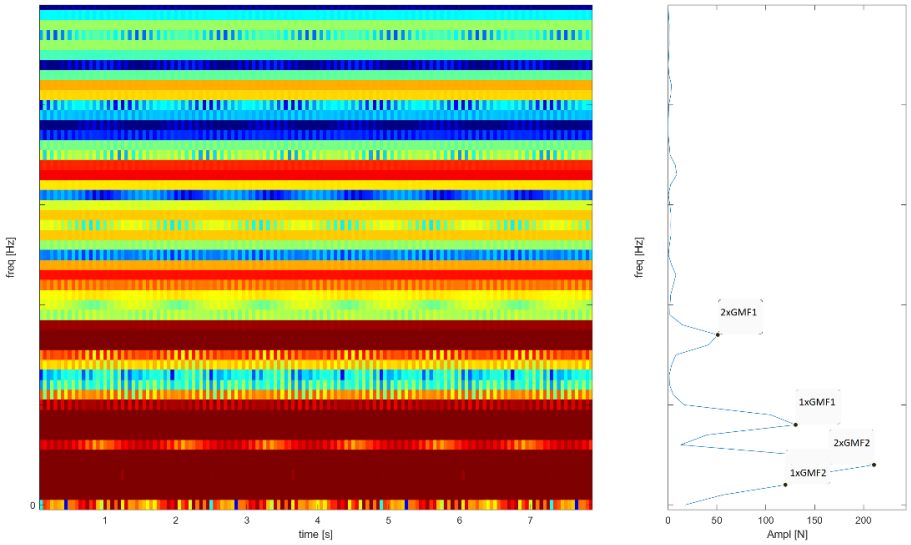


*Figure 99: Waterfall of the total force between meshing teeth*

The waterfall plot of Figure 99 shows similar results with respect to that of the first stage.

## Displacements of first and second stage planet gears and sun gear

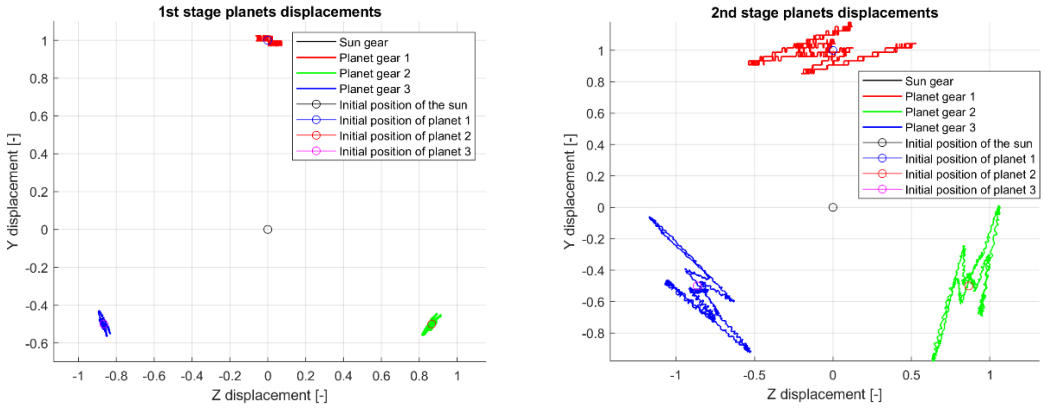


*Figure 100: First and second stage planet displacements on Z-Y plane*

In this case as well, Figure 100 shows that the trajectories traced by the first- and second-stage planet gears are far from the expected circular orbits.

**Displacements of the layshaft at the Z+ and Z− bearings**

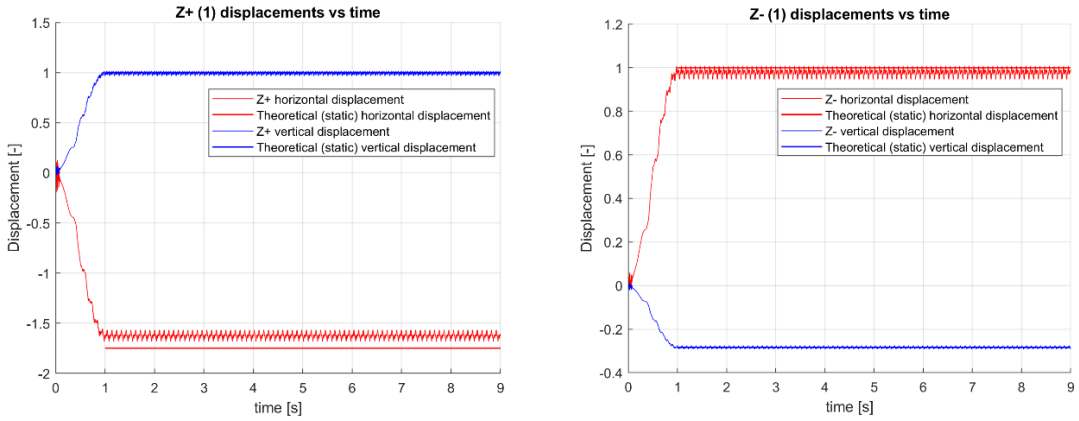


*Figure 101: Bearings displacement over simulation time*

Because of centering the contact pressure on the tooth flanks, the results approach the theoretical reference model, as can be seen in Figure 101. Furthermore, owing to the increased regularity of the contact force, oscillations are much more contained, which translates into a reduction in transmission error.

### 4.2.4. Flexible Body – Flexible tooth – With microgeometry

As anticipated above; in order to account for the deformability of the bodies within the model, it is necessary to introduce a body with a mesh generated in pre-processing using a Finite Element Analysis (FEA) program. The treatment of deformable bodies in Adams is handled by the Adams Flex module; however, when the body in question is a gear body, this can also be managed by the GearAT module of Adams Machinery through two options:

- *Full Flex Gear*
- *Multi Gear Shaft*

The second option is merely an extension of the first (currently available only for spur gears) because, unlike the latter, it allows the wheel body and the shaft to be treated as a single body. By contrast, when using Full Flex Gear, one is compelled to include in the model both the wheel body and the shaft as separate

parts, which must then be joined together using the tools provided by the software (see introduction → Adams/Machinery – Gear AT).

In the case under consideration, the selected option was *Multi Gear Shaft*, which requires the use of the NASTRAN Glued Contact function to connect the so-called Gear Rim to the shaft. During this process, the embedded NASTRAN solver performs a reduction at the interface nodes (Component Mode Synthesis), which will serve as *attachment points* for the body within the Adams environment. The interface nodes are automatically recognized by GearAT because they must necessarily be the independent/dependent nodes of a Rigid Body Element (RBE2/RBE3), respectively [7].

To perform an initial verification of the quality of the process carried out by Adams, a comparison of the modal analysis between the baseline body with the gear teeth generated via the FEA software and the body produced using the *Multi Gear Shaft* option was conducted.

**Modal analysis comparison**

In the following figures, a comparison is presented between the modal analysis of the full 3D mesh of a body (FULL-3D) and the modal analysis of the reduced component on which the NASTRAN Glued Contact function was applied (CB – Glued Contact).

For the input shaft, the following options were selected in the Multi Gear Shaft dialog:

- *Number of Modes* = 70
- Number of interface nodes = 2

The interface nodes for the body in question are used to constrain the input shaft to ground via a revolute joint and to implement the connection of the gear rim to the shaft.

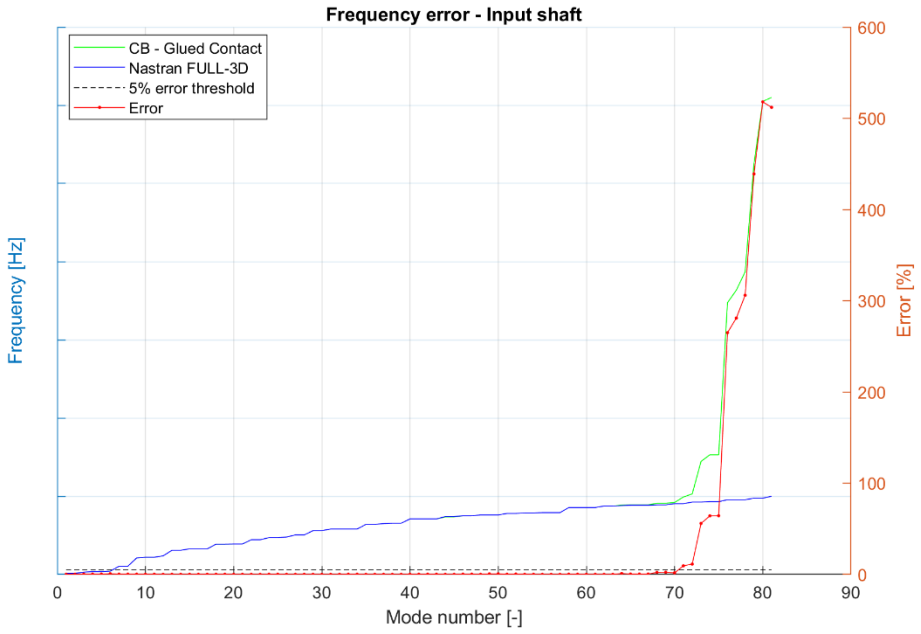


*Figure 102: Frequency error between reduced model and Full 3D model (input shaft)*

As can be observed from the plot in Figure 102, the modal frequency for each mode is essentially the same between the FULL-3D model and the reduced model, with an error almost always below 1% up to approximately the seventieth mode. Beyond this point, the error exceeds 5% as one approach the eightieth mode. This type of divergence is attributable to the model DOF reduction and not to the process performed by Adams for joining the gear rim and the wheel body.

For the layshaft, the following options were selected:

- *Number of Modes* = 70
- Number of interface nodes = 4

In this case, the interface nodes are used for the application of the bushings (Z+ and Z− bearings) and for the first- and second-stage planet gears.

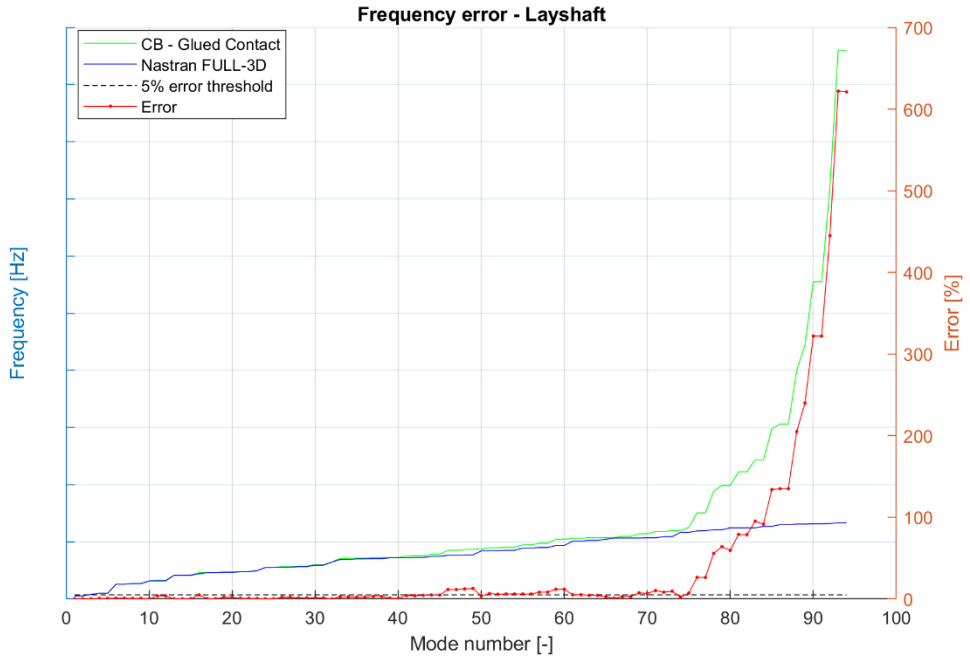


*Figure 103: Frequency error between reduced model and Full 3D model (layshaft)*

Compared with the results obtained for the input shaft, in Figure 103 discrepancies can be observed between the frequencies of the full model and those of the reduced model, particularly for modes numbered 46 through 60. These discrepancies are likely attributable to two factors:

- Presence of two gears mounted on the same shaft
- More wheel-body modes are involved than in the input shaft

The latter appears to be the key factor, given that modes 46–60 are predominantly wheel-body modes radial and out-of-plane of the first-stage planet gear (maximum error within this range = 12.9% for mode 49).

Similarly to what was done for the input shaft, the following options were selected for the ring:

- *Number of Modes* = 70
- Number of interface nodes = 2

In this case, the interface nodes were used to apply the revolute (hinge) constraint between the ring and ground, as well as for the ring gear.

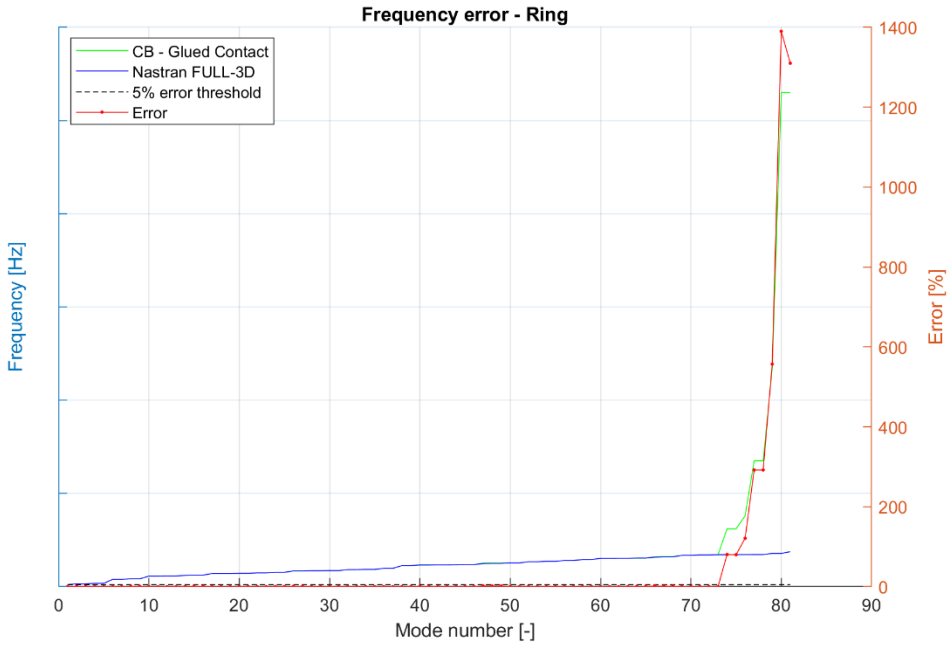


*Figure 104: Frequency error between reduced model and Full 3D model (ring)*

In this case as well, as for the input shaft, the results shown in Figure 104 exhibit good accuracy up to approximately seventy-third mode.

After completing the pre-processing, an MNF file is generated for each part; these files are subsequently imported into Adams, where, via the *Rigid-to-Flex* option, each ideally rigid body used thus far is replaced by the corresponding deformable part.

For this simulation the following settings have been selected:

- Pre-processing of the tooth mesh → *Flexible Tooth*
- For each *GearAT-Element* → Microgeometry is considered
- Modeling option in *GearAT-Force* → *Flexible Tooth*

### Forces exchanged between the teeth – First stage

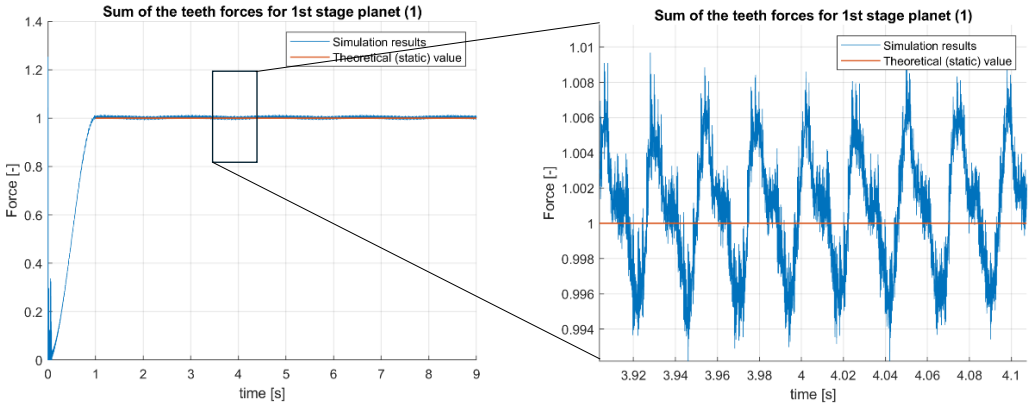


*Figure 105: Total force exchanged at first stage*

As is evident from the first-stage force trend shown in Figure 105, low-frequency oscillations begin to appear. This may be attributable to the large displacements experienced by the sun gear due to the deformability of the input shaft. Moreover, the force magnitude now oscillates far less markedly with respect to the theoretical value than in the previous cases.

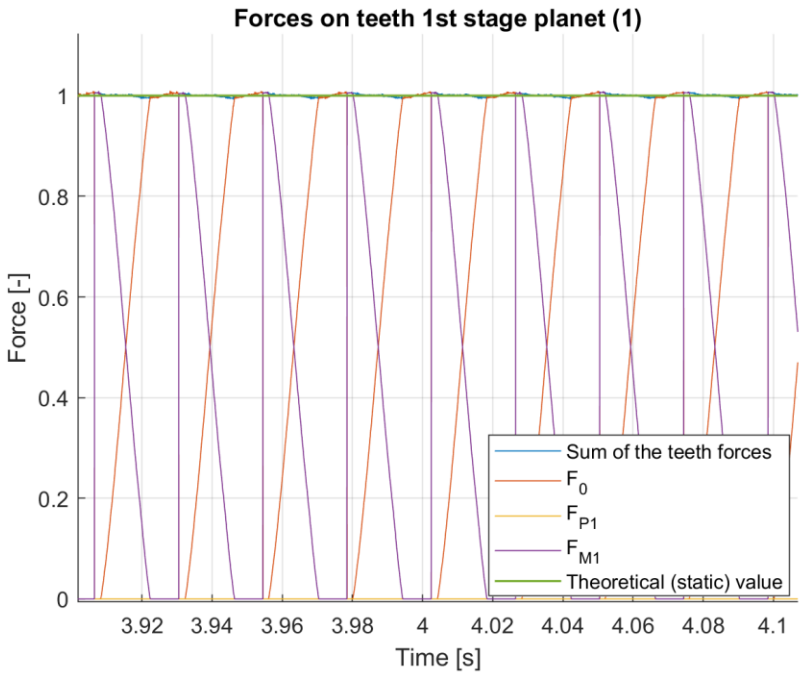


*Figure 106: Total force and single teeth forces exchanged at first stage*

From the plot of Figure 106, it can be inferred that accounting for the components' deformability ensures a more gradual meshing of the gears.

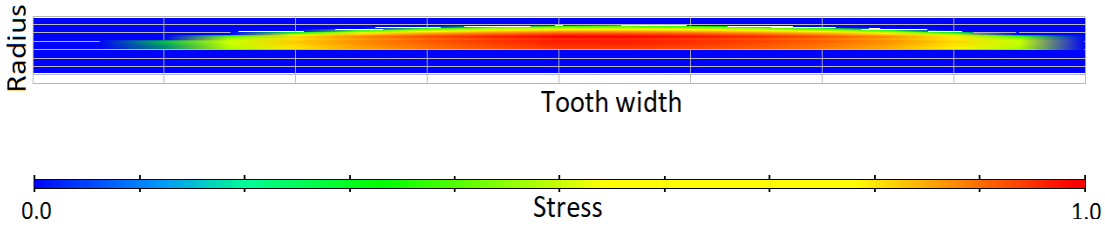


*Figure 107: Pressure distribution on the tooth flank*

The contact pressure map does not exhibit any notable differences compared with the previous case; accounting for the micro-geometry has had the greatest effect in shifting the point of application of the resultant force.

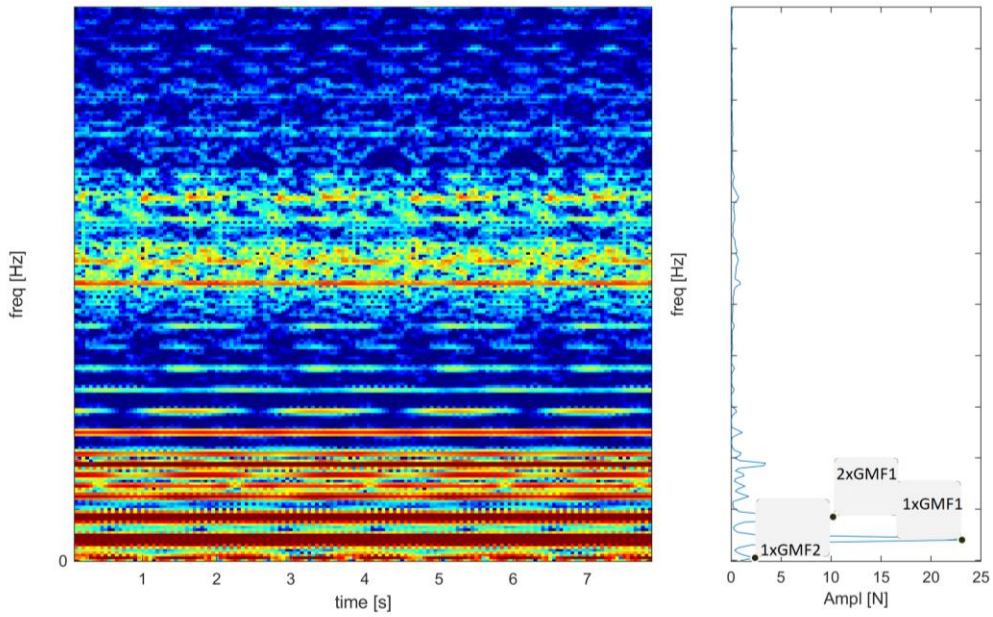


*Figure 108: Waterfall of the total force between meshing teeth*

It is noteworthy that, in this case (Figure 108), the most significant component of the force signal is due to the first-stage gear mesh frequency rather than the second-stage gear mesh frequency, as observed in the previous cases. This phenomenon is likely attributable to the large deformations experienced by the input shaft.

### Forces exchanged between the teeth – Second stage

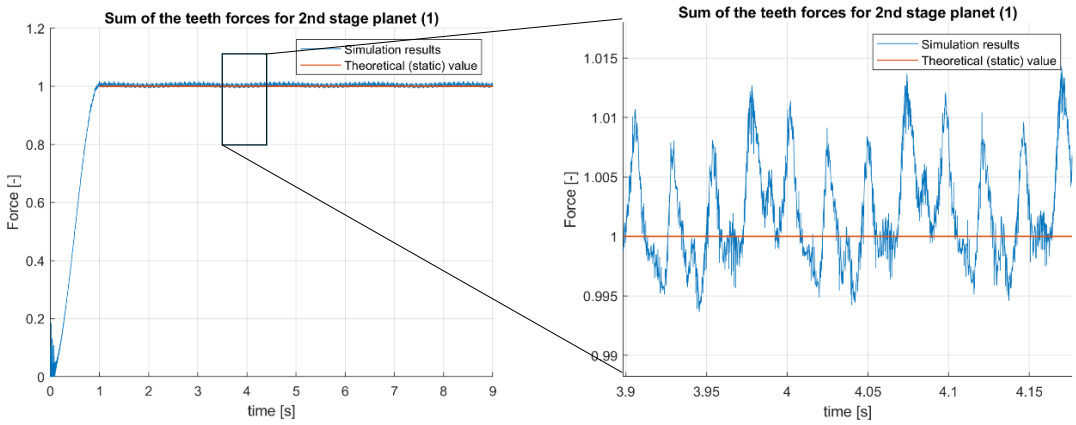


*Figure 109: Total force exchanged at second stage*

For the second stage as well, as shown in Figure 109, low-frequency oscillations are observed in the signal, apparently more pronounced than those present in the first stage.

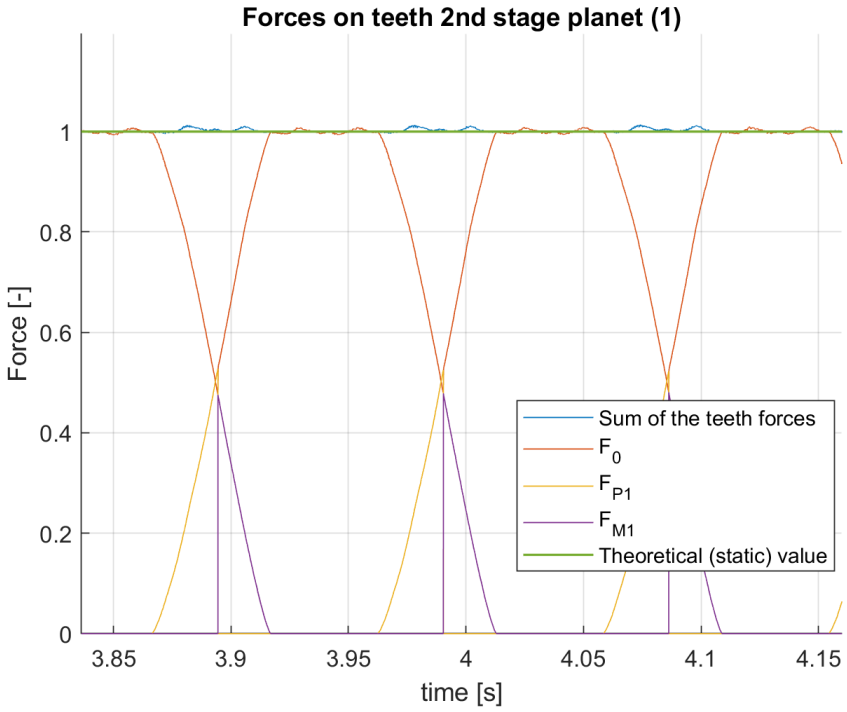


*Figure 110: Total force and single teeth forces exchanged at second stage*

No differences are observed relative to the first stage in Figure 110; here as well, accounting for component deformability has ensured more gradual contact, without sudden force spikes.


*Figure 111: Pressure distribution on the tooth flank*

In this case as well (Figure 111), it can be concluded that the largest effect on the contact pressure distribution was caused by the micro-geometry, not by body deformations.

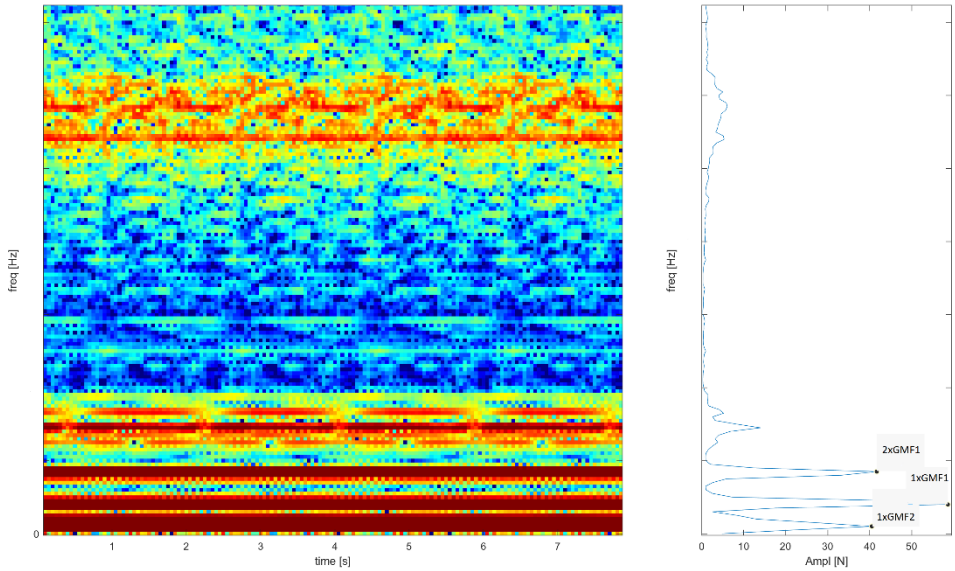


*Figure 112: Waterfall of the total force between meshing teeth*

In the second stage, as in the first, it is evident, from Figure 112, that the most significant component in the force signal is the second-stage gear mesh frequency.

### Displacements of first and second stage planet gears and sun gear

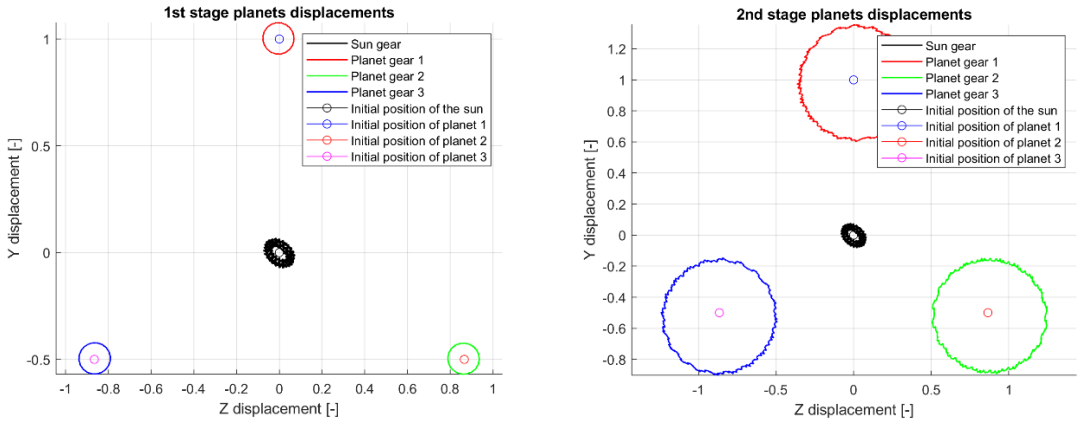


*Figure 113: First and second stage planet displacements on Z-Y plane*

As can be inferred from the plots in Figure 113, the orbits traced by the displacements in the plane perpendicular to the rotation axis of the planet gears are now evident. The peculiarity of this phenomenon is that the oscillations giving rise to these circular trajectories occur at the rotational frequency of the layshafts, underscoring the importance of studying the dynamics of such systems, since at high speed these oscillations may act as an excitation for certain system modes.

### Displacements of the layshaft at the Z+ and Z− bearings

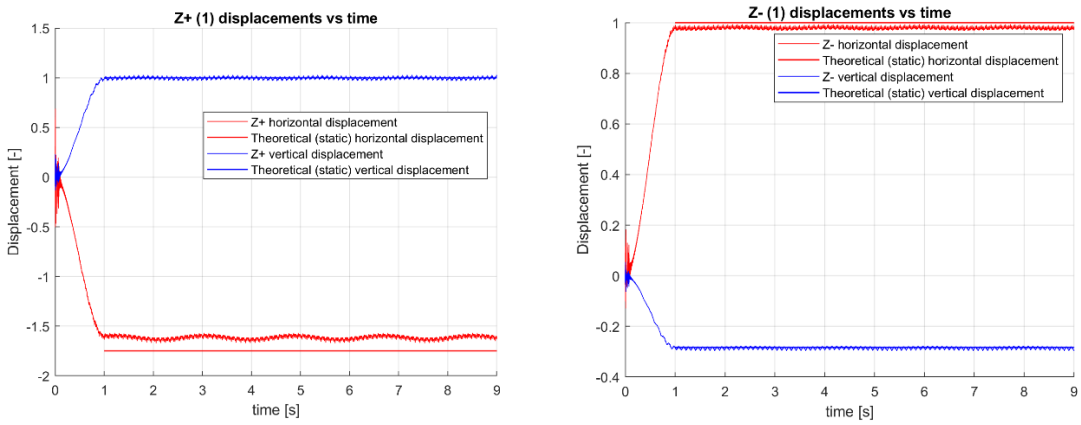


*Figure 114: Bearings displacement over simulation time*

The oscillations observed previously can also be seen in the plots of Figure 114.

# 5. CONCLUSIONS

The initial objective of this thesis was to explore the potential benefits of employing a commercial software package for the multibody analysis of gear transmission systems.

The process of understanding the various functionalities and workflows of the software first required validation of the results through simple rotor models, initially with rigid bodies and subsequently with flexible bodies. The development of the latter made it possible to understand how to introduce flexible bodies, generated by means of FEM (Finite Element Method), into the models. Among the different options available for generating the FE models to be imported, it was possible to exploit the one that accounts for rotor dynamic effects (using the SOL107 procedure of the NASTRAN solver).

Regarding the construction of the *power gearbox model*, it was possible to observe a progressive improvement in the meshing conditions as the model was made to more closely approximate its real counterpart.

The first version of the model considered an ideal case in which all components of the system were rigid, and it was observed that:

- The meshing process occurred in a poorly gradual manner, with sudden peaks in the contact force
- The pressure distribution along the tooth flank exhibited a significant shift of the force application point toward the tooth edge (edge contact)

The second version of the model differs from the first in that it accounts for the (sole) deformability of the teeth under load, and the results showed:

- A more gradual meshing process, but with large oscillations in the transmitted force
- A more uniform pressure distribution, although still highly concentrated at the edge

- An atypical meshing condition in which, throughout the simulation, the contact was always sustained by at least two tooth pairs for both stages

In the third version of the model, tooth profile micro-geometry modifications were introduced, leading to a marked improvement in the results:

- The meshing process was visibly more gradual, and the total force exchanged between the teeth further approached the theoretical value (static case)
- The profile modifications proved to be an essential tool for improving the contact conditions, resulting in better pressure distribution along the tooth flank (more centered around the tooth mid-width)
- A meshing condition was re-established in which the contact was sustained by one or two tooth pairs throughout the entire simulation

In the final version, by means of the multi gear shaft option available in the software, it was possible to take shafts deformations into account and to observe how the geometry of the components influences the system behavior, even under quasi-static conditions. It was indeed possible to notice components displacements (orbital motion of planet gears), particularly when considering bodies deformations, that can influence the dynamic of the system. This behavior appears to be caused by shaft deflections under specific loading conditions and was not observed in the first three versions, which were developed using rigid bodies.

The results of the final version showed:

- Improved meshing conditions, with reduced oscillations in the contact force
- A pressure distribution that remained practically unchanged with respect to the previous case

- The presence of low-frequency oscillations in the contact force and an orbital motion of the planet gears

At the conclusion of this thesis project, it was possible to observe that the use of commercial multibody software, such as MSC.Adams, can represent an effective tool for the modeling and analysis of gear transmission systems, being able to capture significant effects due, for example, to tooth profile micro-geometry modifications. Furthermore, the possibility of rapidly varying the simulation parameters greatly facilitates comparative analyses, allowing verification of whether changes in a given parameter have a significant impact on the system behavior.

This project lays the groundwork for further research in the field of gearbox dynamics and represents a starting point for the adoption of a multibody approach in this domain.

# Appendix

## 1. Reduction Techniques

In the context of static analyses of deformable bodies, the presence of a large number of nodes, and thus degrees of freedom, does not typically pose a problem. By contrast, in dynamic simulations where the equations of motion must be integrated step by step, the presence of large matrices would render the solver's computational time unacceptable. A solution to this problem is to reduce the degrees of freedom of the system which, although it may introduce a certain degree of approximation, substantially lowers computational cost while maintaining satisfactory accuracy.

This introductory subsection is included due to the central role that reduction techniques play when studying the dynamics of a system with many degrees of freedom, and especially because of the challenges associated with integrating such reduction techniques while incorporating deformable bodies within multibody software.

### 1.1. Nodal reduction technique

The simplest reduction method is the nodal method, commonly referred to as *static reduction*, by which one means a process for reducing the stiffness matrix [1]. This reduction is performed by setting the accelerations and velocities of the generalized coordinates to zero (as in the analysis of a static case) and by partitioning the degrees of freedom in *slave degrees of freedom* ($\boldsymbol{q}_2$) and *master degrees of freedom* ($\boldsymbol{q}_1$), subsequently, the generalized coordinates associated with the former are expressed in terms of the latter:

$$\begin{bmatrix} \boldsymbol{K}_{11} & \boldsymbol{K}_{12} \\ \boldsymbol{K}_{21} & \boldsymbol{K}_{22} \end{bmatrix} \begin{Bmatrix} \boldsymbol{q}_1 \\ \boldsymbol{q}_2 \end{Bmatrix} = \begin{Bmatrix} \boldsymbol{f}_1 \\ \boldsymbol{f}_2 \end{Bmatrix}$$

Second set of equations can be written as:

$$\boldsymbol{q}_2 = -\boldsymbol{K}_{22}^{-1}\boldsymbol{K}_{21}\boldsymbol{q}_1 + \boldsymbol{K}_{22}^{-1}\boldsymbol{f}_2$$

In such way the final set of equations is:

$$\boldsymbol{K}_{cond}\boldsymbol{q}_1 = \boldsymbol{f}_{cond} \quad \rightarrow \quad \begin{cases} \boldsymbol{K}_{cond} = \boldsymbol{K}_{11} - \boldsymbol{K}_{12}\boldsymbol{K}_{22}^{-1}\boldsymbol{K}_{12}^{T} \\ \boldsymbol{f}_{cond} = \boldsymbol{f}_1 - \boldsymbol{K}_{12}\boldsymbol{K}_{22}^{-1}\boldsymbol{f}_2 \end{cases}$$

In this way, within the scope of static analyses, no approximation is introduced; indeed, it is a recommended procedure when some nodes of the structure have zero or near-zero mass, thereby reducing the risk of the problem becoming ill-conditioned.

A reduction method similar to the one discussed above is the *Guyan reduction*, which consists in exploiting the same expression obtained for the slave DOFs but this time neglecting the generalized force vector $\mathbf{f_2}$. The resulting expression for $\mathbf{q_2}$ is then substituted into the computation of the system's kinetic energy, thereby obtaining a condensed mass matrix $\mathbf{M_{cond}}$. In a similar manner, $\mathbf{C_{cond}}$ and $\mathbf{G_{cond}}$, respectively the condensed damping and gyroscopic matrices, are derived.

Typically, provided that the choice of slave nodes is appropriate, the aforementioned reduction technique yields good results; however, it is not suitable when high-frequency phenomena are to be investigated.

## 1.2. Component Mode Synthesis (CMS)

One of the most widely used methods for studying the dynamics of structures with many degrees of freedom is *Component Mode Synthesis* (CMS), also called *dynamic reduction* because it can be applied directly to the dynamic stiffness matrix [1]. In general, it is based on partitioning the structure into *boundary degrees of freedom* and *internal degrees of freedom* where, in the context of partitioning a system into substructures, the former are those degrees of freedom shared with other substructures of the system, while the latter are the remaining degrees of freedom of the considered substructure [1]. The core concept underlying this methodology is the definition of the slave degrees of

freedom as the sum of a reduced set of normal modes and a particular set of static modes [9].

There are several possible choices for the modal bases to be used; here we present the one employed in the well-known *Craig–Bampton* method.

The generalized coordinates $\mathbf{q_2}$ are obtained as the sum of a reduced set of *constraint modes* and a set of *fixed-boundary normal modes* [9]. The former are computed by applying, one at a time, a unit displacement to each boundary degree of freedom while keeping all other boundary degrees of freedom fixed. The latter are the modes obtained from an eigen-solution with all boundary degrees of freedom constrained to zero displacement.

Denoting the constraint modes by $\mathbf{q}_2'$ and the fixed-boundary normal modes by $\mathbf{q}_2''$, one can write:

$$\boldsymbol{q}_2 = \boldsymbol{q}_2' + \boldsymbol{q}_2''$$

Where:

$$\boldsymbol{q}_2' = -\boldsymbol{K}_{22}^{-1}\boldsymbol{K}_{21}\boldsymbol{q}_1 = \boldsymbol{\Psi}_c\boldsymbol{q}_1$$

Where the constraint modes are expressed in a manner analogous to that used for the slave DOFs in a Guyan reduction, while for the fixed-boundary normal modes it is necessary to solve the following eigenvalue problem:

$$\begin{bmatrix}\boldsymbol{M}_{11} & \boldsymbol{M}_{12}\\ \boldsymbol{M}_{21} & \boldsymbol{M}_{22}\end{bmatrix}\begin{Bmatrix}\ddot{\boldsymbol{q}}_1\\ \ddot{\boldsymbol{q}}_2\end{Bmatrix} + \begin{bmatrix}\boldsymbol{K}_{11} & \boldsymbol{K}_{12}\\ \boldsymbol{K}_{21} & \boldsymbol{K}_{22}\end{bmatrix}\begin{Bmatrix}\boldsymbol{q}_1\\ \boldsymbol{q}_2\end{Bmatrix} = \begin{Bmatrix}\mathbf{0}\\ \mathbf{0}\end{Bmatrix} \quad \rightarrow \quad \boldsymbol{M}_{22}\ddot{\boldsymbol{q}}_2 + \boldsymbol{K}_{22}\boldsymbol{q}_2 = \mathbf{0}$$

Where, since we're interested in the fixed-boundary normal modes discussed above, we're considering boundary coordinates to be equal to zero. By solving the eigen problem it is possible to obtain the following coordinates transformation:

$$\boldsymbol{q}_2'' = \boldsymbol{\Psi}_f\boldsymbol{\eta}_2$$

Where $\boldsymbol{\Psi}_f$ is the modal matrix and $\boldsymbol{\eta}_2$ are the modal coordinates. It is of relevant importance to notice that one can arbitrarily choose the number of desired modes. The higher the number of nodes the higher the correspondence with the actual behavior of the substructure but to not lose the usefulness of the reduction method the number of fixed-boundary normal modes, *k,* should be lower than the number of internal degrees of freedom, *n.*

By considering the whole vector of generalized coordinates:

$$\boldsymbol{q} = \begin{Bmatrix} \boldsymbol{q}_1 \\ \boldsymbol{q}_2 \end{Bmatrix} = \begin{Bmatrix} \boldsymbol{q}_1 \\ \boldsymbol{\Psi}_c \boldsymbol{q}_1 + \boldsymbol{\Psi}_f \boldsymbol{\eta}_2 \end{Bmatrix} = \begin{bmatrix} \boldsymbol{I} & \boldsymbol{0} \\ \boldsymbol{\Psi}_c & \boldsymbol{\Psi}_f \end{bmatrix} \begin{Bmatrix} \boldsymbol{q}_1 \\ \boldsymbol{\eta}_2 \end{Bmatrix} = \boldsymbol{\Psi} \begin{Bmatrix} \boldsymbol{q}_1 \\ \boldsymbol{\eta}_2 \end{Bmatrix}$$

Where $\boldsymbol{\Psi}$ represents the CB-Transformation matrix. To reduce the remaining terms of the EOMs it is possible to proceed as follows:

$$\boldsymbol{M}^* = \boldsymbol{\Psi}^T \mathbf{M} \boldsymbol{\Psi}; \quad \mathbf{K}^* = \boldsymbol{\Psi}^T \mathbf{K} \boldsymbol{\Psi}; \quad \mathbf{C}^* = \boldsymbol{\Psi}^T \mathbf{C} \boldsymbol{\Psi}; \quad \mathbf{G}^* = \boldsymbol{\Psi}^T \mathbf{G} \boldsymbol{\Psi}; \quad \mathbf{f}^* = \boldsymbol{\Psi}^T \mathbf{f}$$

The CB-Transformation matrix allows to pass from the original matrices having size $m \times n$, where m is the number of boundary DOFs, to the reduced matrices having size $m \times k$.

This above-described transformation is of great interest because it's one of the most used in the Floating Frame of Reference (FFR) formulation which is by far the most common way to deal with the introduction of flexible bodies within the framework of multibody software.

## 2. Multibody software theory

The introduction of deformable bodies in multibody software algorithms is a complex matter for which different formulations have been developed, the most used in commercial software are: Absolute Nodal Coordinate Formulation (ANCF), Consistent Rotation-Based Formulation (CRBF) and the Floating Frame of Reference Formulation (FFRF) [10]. In many software applications the FFRF appears to be the most used formulation because it provides a relatively simple mathematical approach being able to manage large body

displacements whereas considering small deformation for any flexible body in the model, these latter described by means of a body coordinate system. On the contrary, the ANCF and CRBF have no need for the introduction of body coordinate system and can describe both large deformation and displacements. However, the two formulations have the drawback of having a highly non-linear function of the generalized coordinates representing a vector of generalized elastic forces, whereas the advantage of considering small deformations in the FFRF leads to have a linear vector of generalized elastic forces [10].

## 2.1. Floating Frame of Reference Formulation

To properly describe the kinematic of a flexible body the FFRF formulation exploit, besides the already anticipated body coordinate system, an Intermediate Element Coordinate system (IEC) for each element $j$ inside the body $i$. This IEC system is fixed on the origin of the body coordinate system, but its orientation is parallel to that of element $j$ coordinate system [9], [11].

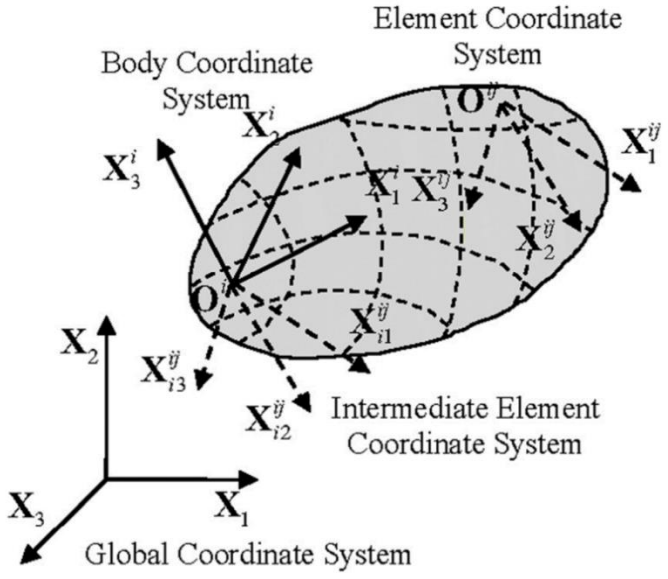


*Figure 115: Schematic of reference frames used in the FFR formulation [9]*

In **Errore. L'origine riferimento non è stata trovata.** it is possible to see a representation of the Global Coordinate System, the Body Coordinate System, the Intermediate Coordinate System and the Element Coordinate System.

The position of a generic point $p$ in element $j$ of body $i$ is described by the following expression:

$$\boldsymbol{r}_p^{ij} = \boldsymbol{R}^i + \boldsymbol{A}^i \boldsymbol{C}^{ij} \boldsymbol{S}_p^{ij} \overline{\boldsymbol{C}}^{ij} \boldsymbol{q}_n^{ij}$$

Where $\boldsymbol{R}^i$ is the position of the origin of the body coordinate system in the global system, $\boldsymbol{A}^i$ is a rotation matrix for passing from body coordinates to global ones, $\boldsymbol{C}^{ij}$ is the transformation matrix for passing from the element coordinate system to the body coordinate system, $\boldsymbol{S}_p^{ij}$ is the shape function, $\overline{\boldsymbol{C}}^{ij}$ is a constant transformation matrix used to pass from the nodal coordinates in the IEC system to the generalized coordinates $\boldsymbol{q}_n^{ij}$ in the body coordinate system.

This latter vector can be written as $\boldsymbol{q}_n^{ij} = \boldsymbol{q}_0^{ij} + \overline{\boldsymbol{q}}_f^{ij}$, where the first term is the vector of un-deformed nodal coordinates whereas the second term is the vector of nodal deformations. By partitioning the nodal coordinates in this manner, it is possible to introduce *reference conditions* separately on the nodal deformations vector, in this way it is possible to eliminate the rigid body modes from the shape function. This procedure allows us to obtain a unique displacement field for the flexible body. To pass to the total nodal coordinates of body *i,* from the nodal coordinates of the only element *j,* a Boolean matrix $\boldsymbol{B}_1^{ij}$ is used such that $\boldsymbol{q}_n^{ij} = \boldsymbol{B}_1^{ij} \boldsymbol{q}_n^i$. By defining the *matrix of the reference conditions* $\boldsymbol{B}_2^i$ it is possible to write $\overline{\boldsymbol{q}}_f^i = \boldsymbol{B}_2^i \boldsymbol{q}_f^i$, leading to the final form of the above equation [9], [11]:

$$\boldsymbol{r}_p^{ij} = \boldsymbol{R}^i + \boldsymbol{A}^i \boldsymbol{C}^{ij} \boldsymbol{S}_p^{ij} \overline{\boldsymbol{C}}^{ij} \boldsymbol{B}_1^{ij} (\boldsymbol{q}_0^i + \boldsymbol{B}_2^i \boldsymbol{q}_f^i)$$

Considering the aforementioned partition of the nodal coordinates the set equation of motions of the system becomes:

$$\begin{bmatrix} \boldsymbol{M}_{rr}^{i} & \boldsymbol{M}_{rf}^{i} \\ \boldsymbol{M}_{fr}^{i} & \boldsymbol{M}_{ff}^{i} \end{bmatrix} \begin{Bmatrix} \ddot{\boldsymbol{q}}_{r}^{i} \\ \ddot{\boldsymbol{q}}_{f}^{i} \end{Bmatrix} + \begin{bmatrix} \mathbf{0} & \mathbf{0} \\ \mathbf{0} & \boldsymbol{K}_{ff}^{i} \end{bmatrix} \begin{Bmatrix} \boldsymbol{q}_{r}^{i} \\ \boldsymbol{q}_{f}^{i} \end{Bmatrix} = \begin{Bmatrix} \boldsymbol{Q}_{r}^{i} \\ \boldsymbol{Q}_{f}^{i} \end{Bmatrix}$$

At this point it is possible to perform matrix condensation with previously discussed CMS to reduce model size.

The software MSC.Adams used throughout this project exploits FFRF formulation.

# References


[1] G. Genta, Dynamics of Rotating Systems, Torino: Springer, 2004.

[2] C. Xie e X. Shu, «A new mesh stiffness model for modified spur gears with coupling tooth and body flexibility effects,» *Applied Mathematical Modelling,* pp. 1194-2010, 2020.

[3] H. Vinayak e R. Singh, «MULTI-BODY DYNAMICS AND MODAL ANALYSIS OF COMPLIANT GEAR BODIES,» *Journal of Sound and Vibration,* pp. 171-214, 1997.

[4] G. Saletti, G. Battiato e S. Zucca, «A Coupled Harmonic Balance-Based Approach for the Non-Linear Dynamics of Spur-Gear Pairs,» *Vibration,* pp. 1-13, 2025.

[5] F. Bejar, «Geometry and mounting optimization of lightweight gearbox components,» Lyon, 2024.

[6] W. Yu e C. K. Mechefske, «Analytical modeling of spur gear corner contact effects,» *Mechanism and Machine Theory,* pp. 146-164, 2015.

[7] Hexagon, *Adams 2023.4: Adams Machinery User's Guide,* 2023.

[8] V. Y. Öztürk, E. Cigeroglu e H. N. Özgüven, «Ideal tooth profile modifications for improving nonlinear dynamic response of planetary gear trains,» *Journal of Sound and Vibration,* pp. 1-20, 2021.

[9] Hexagon, *Adams 2024.1: Adams Flex User's Guide,* 2024.

[10] A. Cammarata e C. M. Pappalardo, «On the use of component mode synthesis methods for the model reduction of flexible multibody systems within the floating frame of reference formulation,» *Mechanical Systems and Signal Processing,* pp. 1-29, 2020.

[11] J. J. O'Shea, P. Jayakumar, D. Mechergui, A. Shabana e L. Wang, «REFERENCE CONDITIONS AND SUB-STRUCTURING TECHNIQUES IN

FLEXIBLE MULTIBODY SYSTEM DYNAMICS,» *Journal of Computational and Nonlinear Dynamics,* pp. 1-56, 2018.

[12] M. Software, *MSC Nastran 2019: Quick Reference Guide,* 2019.

[13] M. Software, *MSC Nastran 2019: Rotordynamics User's Guide,* 2019.

[14] Hexagon, *Adams 2022.4: Adams Solver User's Guide,* 2022.

[15] Hexagon, *Adams Rotor Dynamics Using MNF from MSC Nastran SOL 107,* 2024.

[16] Hexagon, *Adams 2023.4, Getting Started: Adams Machinery,* 2023.

[17] A. Nandi e S. Neogy, «Modelling of rotors with three-dimensional solid finite elements,» *The Journal of Strain Analysis for Engineering Design,* pp. 359-371, 2001.